UNIVERSITÀ DEGLI STUDI DI UDINE
DIPARTIMENTO POLITECNICO DI INGEGNERIA E ARCHITETTURA
PHD IN INDUSTRIAL AND INFORMATION ENGINEERING

PIEZOELECTRIC TRANSDUCERS FOR BROADBAND VIBRATION CONTROL

BY
DANIEL CASAGRANDE

SUPERVISOR: Prof. Paolo Gardonio
CO-SUPERVISOR: Prof. Stefano Saggini

ACADEMIC YEAR 2015-2016

ABSTRACT

This thesis presents theoretical and experimental studies concerning active and semi-active systems for the vibration control of the flexural response of a thin plate using piezoelectric transducers. Concerning the active control systems, velocity feedback loops are implemented using a piezoelectric patch with a particular shape as actuator. This piezoelectric patch is composed of 6 triangular leafs disposed in such a way as to form an hexagonal patch. Single and decentralised multiple channel configurations were studied, using the Nyquist criteria to analyse the stability of the control loop and the kinetic energy of the flexural response of the panel to asses the control performance.

Then, a fully coupled model of a semi-active vibration control system is presented, which uses a piezoelectric transducer connected to an electric shunt circuit composed of an inductance and a resistance. A reduced model that neglects the structural damping and considers only the first natural mode of the plate was used to derive the optimum values for the inductance and resistance of the shunt circuit. These values were then compared to the ones found numerically using a genetic algorithm and considering an increasing amount of natural modes of the plate. A parametric study is also presented in which the effects of the piezoelectric patch dimension on the vibration control performance is analysed.

The last part of the thesis presents a time-varying shunted piezoelectric absorber that produces a broadband control effect of the flexural response of the plate. Single and multiple configurations were studied, and two control laws were proposed for the shunt: switching mode, in which the inductance and resistance values cyclically change between a set of three pairs of values in order to control iteratively the flexural response of the panel near three of its natural frequencies; and sweeping mode, in which the shunt values are varied continuously from a lower to an upper bound that match the lower and upper values of the frequency range of interest. Series and parallel operation modes are proposed for the multiple configuration using five time-varying shunted piezoelectric vibration absorbers. In the series mode the targeted frequency range is divided in five sub-ranges in which only one piezoelectric vibration absorber works and in the parallel mode all five absorbers work in the full targeted frequency range but with a phase shift between each other.

ACKNOWLEDGEMENTS

First of all, I would like to thank my supervisor Prof. Paolo Gardonio for his valuable guidance and continuous support during my work here at the University of Udine. He has always been willing to share his expertise and I have learned a lot from him. I would also like to thank my co-supervisor Prof. Stefano Saggini for his help during the experimental measurements.

A special acknowledgement goes to Elvio Castellarin and to the staff from the DPIA for their help and patience.

The work produced during my stay in Udine was founded by the European Commission through the MSC ITN EMVeM programme and it is gratefully acknowledged.

On a personal level I would like to thank my family for their advice and encouragement and my friends and colleagues with whom I shared the best moments during this experience in Udine. It has been a great honor for me to work together with you all, thank you very much for your friendship, advices, useful ideas, and support during long days at work.

CONTENTS

LIST OF FIGURES

LIST OF TABLES

NOMENCLATURE

LIST OF ACRONYMS

AC	Alternating current
ADC	Analogue-to-digital converters
AVC	Active vibration control
BSD	Blind switch damping
CLPT	Classical laminated plate theory
CPU	Central processing unit
DAC	Digital-to-analogue converters
DC	Direct current
DFT	Discrete Fourier Transform
FRF	Frequency response function
GA	Genetic algorithm
IEPE	Integrated electronic piezoelectric
LC	Inductive-capacitive
MFC	Macro fiber composite
MIMO	Multiple-input multiple-output
PVDF	Polyvinylidene fluoride
PZT	Lead zirconate titanate
RL	Resistive-inductive
RLC	Resistive-inductive-capacitive
SISO	Single-input single-output
SSD	Synchronized switch damping
SSDI	Synchronized switch damping on inductor
SSDV	Synchronized switch damping on voltage source
TVA	Tuned vibration absorber

LIST OF SYMBOLS

Parameter	Description	Unit
l_x	Length of the panel	[m]
l_y	Width of the panel	[m]
h_p	Thickness of the panel	[m]
A_p	Area of the panel	[m^2]
Y_p	Young's modulus of the panel	[N/m^2]
ν_p	Poissons's ratio of the panel	—
m_p	Mass of the panel per unit area	[kg/m^2]
ρ_p	Density of the panel	[kg/m^3]
ξ_p	Modal damping ratio of the panel	—
d_x	Length of the transducer	[m]
d_y	Width of the transducer	[m]
h_{pe}	Thickness of the transducer	[m]
A_{pe}	Area of the transducer	[m^2]
Y_{pe}	Young's modulus of the transducer	[N/m^2]
ν_{pe}	Poissons's ratio of the transducer	—
$\mathbf{D}, D_{ij}$	Electric displacement vector and coefficients	[C/m^2]
$\mathbf{E}, E_{ij}$	Electric field vector and coefficients	[V/m]
$\mathbf{T}, T_{ij}$	Stress vector and coefficients	[N/m^2]
$\mathbf{S}, S_{ij}$	Strain vector and coefficients	—
ε_0	Free space electric permittivity	[F/m]
ε_r	Relative electric permittivity	—
ε	Electric permittivity	[F/m]
β	Electric impermittivity	[m/F]
C_{pe}	Transducer inherent capacitance	[F]
$\mathbf{s}, s_{ij}$	Compliance matrix and coefficients	[m^2/N]
d_{ij}	Piezoelectric strain constants	[m/V] [C/N]
g_{ij}	Piezoelectric voltage constants	[Vm/N] [m^2/C]
e_{ij}	Piezoelectric stress constants	[N/Vm] [C/m^2]

Parameter	Description	Unit
k	Piezoelectric electromechanical coupling factor	—
t	Time	[sec]
ω	Frequency	[Hz]
j	Imaginary unit defined as $j = \sqrt{-1}$	—

1

INTRODUCTION

Vibrations in mechanical systems are a response, usually an undesired one, to excitation forces due to the operation process itself or due to external or environmental causes. Mechanical vibrations are found almost everywhere and depending on the considered system and the type, frequency and amplitude of the vibrations, these can be neglected in the best case and generate noise, accuracy and other types of issues, or even damage and destroy the system or injuring people in the worst case. Considering their effects on humans, in the best case they are harmless or cause minor discomfort but they can also be accounted for headaches, nausea and a wide variety of health issues, including death in the worst case [3]. In the engineering field, vibration control of structures is of great interest in very different applications: from the manufacturing sector, to the maritime, space, aerospace, railway and automotive industries, to consumer goods industries as vibrations can be the source of lower productivity, material fatigue issues, or, amongst many others, user discomfort that translates in a loss of the market share, e.g. a washing machine or a car that are too noisy or vibrate too much [3–5]. In addition, many countries have set legal regulations that industries must meet regarding workers exposure to noise and vibration, e.g. within the European Union the regulations for noise and vibration are the Noise at Work Directive 2003/10/EC and the Human Vibration Directive 2002/44/EC setting as limit values 87 dB(A) for average daily noise exposure level, 2.5 m/s^2 for single action hand-arm vibration, 0.5 m/s^2 for single action whole-body vibration.

The diversity of size of the structures were vibration control is needed is also reflected in the diversity of the frequency ranges of the significant vibrations: $1 - 20$ Hz for some systems, $20 - 250$ Hz for others, tonal or broad band, etc [5]. The targeted frequency range is one of the parameters to take into account in order to choose the best vibration control strategy. Another one is the nature of the vibration: flexural, torsional or longitudinal.

A variety of techniques have been developed over the years to produce the desired vibration control effect on such different applications; these techniques are usually categorized depending on the use of external power sources in two main categories: passive or active; with many authors also referring to a third category usually called semi-passive or semi-active.

1.1 PASSIVE VIBRATION CONTROL

Passive treatments involves changes in the stiffness, mass and damping of the vibrating system and in this way making it less responsive to the sources of vibrations. These changes are usually design modifications or the addition of masses, dampers or springs; elements that passively react in opposition to the accelerations, velocities or deflections imposed upon them [5]. This means that they do not require external power. In his book [5], Mead has classified the passive vibration control approaches into four main categories:

BY STRUCTURAL DESIGN: optimizing the design of a mechanical system can reduce its vibration levels, e.g. by shifting the system resonance frequencies away from the excitation frequencies;

BY LOCALIZED ADDITIONS: a lumped mass or a vibration absorber (a combination of mass, spring and damper elements) is added at a specific place of the structure where it can neutralize the exciting force over a narrow frequency band;

BY ADDED DAMPING: with the addition of highly damped polymeric materials located in specific places of a lightly damped structure where they can dissipate as much energy as possible; and

BY RESILIENT ISOLATION: useful when the vibration is transmitted through few connection points, then these connections are made of soft or resilient rubber springs that can isolate the system from the source of vibration.

Passive solutions such as localized additions or added damping work well at high frequencies, however at lower frequencies they usually require a lot of space and introduce significant weight to the structure while delivering a limited control performance. Another factors to consider are the ageing of the damping material and changes in the system working conditions that would decrease the performance of these passive vibration control systems.

1.2 ACTIVE VIBRATION CONTROL

In active vibration control (AVC) electromechanical, electrohydraulic or electropneumatic actuators are used to produce a vibration that counteracts the original one produced by the exciting forces. These systems use sensors to measure the vibration of the structure, an electronic system to process the signals and to deliver the control signal to an amplifier that drives the actuators. AVC systems can be used in conjunction with passive treatments, which also act as a back-up to prevent serious damages in case the AVC unit fails for some reason and the feedback loop becomes unstable. Some of the drawbacks of active systems are the need of an external supply, instability and spillover (enhancing the vibration level at some frequencies) issues. Nevertheless, they are able to, in a wide range of operating conditions, achieve remarkable performances, specially at low frequencies.

Active vibration control systems can be classified into two main categories: feed-forward and feedback control. Feed-forward control is used when the disturbance is deterministic or tonal or when there is a signal reference strongly correlated with the disturbance [6]. A secondary disturbance is generated in order to destructively interfere with the primary one. This type of control relies in some prior knowledge of the primary disturbance, however the system can tune or adapt to different working conditions by using a reference signal and an adaptive filter. The reference signal (e.g. a tachometer signal for combustion engines) is measured and passed to the adaptive filter and then to an amplifier that drives an actuator. The performance of a feed-forward control system relies on the delicate interaction between the effects of the primary and secondary disturbances. Thus, the amplitude and phase of the controller must be carefully adjusted [6]; for this reason it is very important to use efficient algorithms to tune the controller in real time [7]. It is important to note here that, for adaptive feed-forward control systems, the reference signal measured by the sensor is not affected by the secondary disturbance.

On the other hand, feedback control systems are implemented when the original excitation of the structure cannot be directly observed, so no reference signal or prior information is available for the controller; e.g. when the structure is subjected to a broadband random excitation from many sources. Feedback control systems are widely used for controlling the vibration of lightly damped structures that are characterised by well separated resonance peaks at low frequency and for which the disturbance at each resonance peak is relatively narrowband [7]. An ideal velocity feedback is equivalent to a sky-hook damper;

so, considering that the response of a structure near low resonance frequencies is mainly controlled by damping, then velocity feedback loops can be used to actively increase the effective damping of the system [6].

Another type of classifying active control systems is referred to the amount of inputs and outputs of the system. The most usual classification is single-input single-output systems (SISO) and multiple-inputs multiple-outputs (MIMO) systems. SISO systems use only a pair of sensor and actuator while MIMO systems use an array of them and according to the control strategy they can be categorised as centralised or decentralised.

In centralised MIMO control systems all the sensors provide their signal to a centralised controller that process them and send the control signals to every actuator. The number of sensors and actuators is not always the same and they do not need to be collocated [6, 8, 9]. These type of control is used at low frequencies were the response of the structure is due to a small number of natural modes of the structure. Some disadvantages of centralised control are the wiring (in large structures it translates in higher cost and weight), complex control algorithms and the fact that the failure of one control channel makes the whole system fail.

Decentralised MIMO control systems are characterised by an array of collocated sensor-actuator pairs. Each pair has a dedicated controller and acts as a SISO control system, i.e. the signal measured by one sensor is processed and then fed to its correspondent actuator. The main advantage of this system is the simplicity of the control loops, which are simple gains for ideal velocity sensors and force actuators, and the fact that if one single unit fails the system continue to work. The main disadvantage of this type of control systems is the existence of crosstalk effects, which means that the stability of each loop is influenced by the vibration generated by neighbouring actuators. i.e. the interaction between single control loops, that may introduce instabilities into the control system [10].

Active control using piezoelectric patches has been explored in many recent studies [11–15] proposing SISO and MIMO decentralised control systems. Efficient, compact and lightweight smart structures can be achieved with this type of transducers, considering that the sensor and actuator can be embedded to the original structure.

Another interesting possibility using piezoelectric transducers is the self-sensing technique, developed by Dosch [16] and Anderson [17]. In this case the same piezoelectric patch is used as sensor and actuator. The key idea is, instead of using a sensor, to estimate the voltage induced in the piezoelectric patch, which is proportional to the mechanical strain in the hosting structure. This would provide a suitable signal for a feedback compensator [18].

1.3 SEMI-PASSIVE VIBRATION CONTROL

Semi-passive vibration control systems are passive systems that can change or update its parameters to adapt to changes in the working or environmental conditions, e.g. tensioning effects or temperature changes that change the properties of the hosting structure.

Shunted piezoelectric vibration absorbers are usually considered in this category, as the shunt parameters are varied or tuned to obtain the desired control effect and also because the tension-current characteristic of certain elements such as inductances is reproduced using virtual inductors because the needed values lie outside the commercial ranges or because the size and weight of such inductor would be too large.

Forward [19] was the first to experimentally introduce in 1979 the idea of using shunted piezoelectric transducers to control mechanical vibrations. He considered a piezoelectric patch bonded on a thin structure and connected to an electrical shunt circuit composed of an inductance. Uchino [20], around a decade later, investigated the effects produced by a shunt composed of a pure resistance. Then, some years later Hagood and von Flotow [21] presented a study showing the effects of using resistive and resistive-inductive (RL) shunts. They showed that using only a resistor the piezoelectric transducer produces a viscoelastic damping effect while when using the RL shunt it produces a resonating vibration absorption effect. They also derived, using as starting point the work of Den Hartog [22] with mechanical vibration absorbers, the expressions for the resistance and inductance to optimise the vibration absorption effect at the resonance frequency of a specific natural mode of the structure. References [18, 23] offer detailed reviews on vibration control using shunted piezoelectric transducers as well as the comprehensive book by Moheimani and Fleming [24].

Forward was also one of the first to consider a negative capacitance in the shunt to compensate the inherent capacitive effect of the piezoelectric transducer and improve the vibration absorption effect [25]. Since then many authors have been investigating this idea, see references [24, 26–37], who acknowledge the fact that to implement a negative capacitance active systems must be used with the corresponding power and stability issues.

Other techniques using semi-passive shunted piezoelectric transducers are the switching techniques. Most of these were developed during the late 90s and the first decade of the current century; the most popular one is the pulse switching or synchronized switch damping (SSD) [38], from which almost all the others, such as blind switch damping (BSD) [39], synchronized switch damping on voltage source (SSDV) [40] and synchronized switch damping on inductor (SSDI) [40], are derived. These are non-linear techniques and the basic principle is to open and short-circuit the transducer (or connect it to a particular shunt circuit) intermittently and synchronously with the structure motion. BSD works in a similar way but with a fixed switching period instead of synchronously with the structure motion [39].

Another idea that has attracted a lot of attention in the previous years is the use of periodic arrays of piezoelectric patches to form smart metamaterials with specific vibro-acoustical properties. Metamaterials are engineered materials arranged in repeating patterns, smaller than the wavelength of interest, whose properties come from their particular structure and not from the materials properties. In addition, using periodic arrays of shunted piezoelectric patches, it is possible to combine the vibration absorption effects of the shunted piezoelectric transducer and of the periodic structure, such as in references [41–43].

1.4 OBJECTIVE OF THE THESIS

The main objective of this thesis is to study and develop active and semi-passive vibration absorbers using piezoelectric transducers for the broadband control of the flexural response of a thin plate.

1.5 CONTRIBUTIONS OF THE THESIS

The main contributions of this thesis are:

- development and testing of an hexagonal transducer with an increased loop stability for active vibration control using velocity feedback loops (chapter 3);
- development of a fully coupled model for shunted piezoelectric transducers bonded on thin plates that implement time-varying control loads (chapter 4 and 5);
- analysis of the transducer mechanical and electromechanical coupling effect on the shunt tuning and of the validity of analytical expressions for

the optimum values of the shunt inductance and resistance obtained with a simplified model that considers only one natural mode of the structure and neglects its structural damping (chapter 4);

- general guidelines regarding the transducer dimensions and control performance for shunted piezoelectric absorbers (chapter 4);
- development of switching and sweeping vibration absorbers, which use piezoelectric transducers connected to time-varying RL shunts for the broadband control of the flexural response of a thin plate (chapter 5).

1.6 STRUCTURE OF THE THESIS

Chapter two serves as an introduction to piezoelectric materials, presenting some historical background, the piezoelectric direct and inverse effects and it focus on the fabrication, poling and working principle of piezoceramic transducers. The constitutive equations and the coefficients that characterize piezoelectric elements are presented here.

Chapter three presents a study on velocity feedback loops for active vibration control of a thin panel in which piezoelectric transducers, with a particular hexagonal shape, are used as actuators. SISO and MIMO configurations were studied, the stability of the feedback loops is analysed using the Nyquist criteria and the performance is assessed through the kinetic energy of the flexural response of the panel. Simulations and experimental results are presented.

Chapter four introduces a fully couple model to analyse the shunt tuning and a parametric study on the dimension of the piezoelectric transducer used in a shunted vibration absorber device. Optimum values for the shunt inductance and resistance to maximise the vibration absorption effect are found analytically for a simplified system that considers only the first natural mode of the panel and neglects the structural damping. These values are then compared to the ones found numerically using the fully coupled model considering an increasing amount of natural modes of the structure. The last section of the chapter presents a parametric study in which the thickness and surface area of the piezoelectric transducers are varied within certain ranges to analyse their effect on the performance of the shunted vibration absorber, using always the optimum values for the shunt obtained for each transducer dimension using a genetic algorithm.

Chapter five presents time-varying shunted piezoelectric absorbers to control the flexural response of a plate over a broad frequency band. Two operation modes are proposed for the control of the time-varying shunt: switching and sweeping modes. The switching mode, that should not be confused with the SSD techniques discussed above, changes iteratively between three pairs of inductance and resistance values in order to control three different resonance peaks of the plate. The algorithm remains in the current pair of values for a time greater than the time constant of the RLC parallel circuit and then changes to the next pair of values, cyclically. On the other hand, instead of discrete changes as in the switching mode, in the sweeping operation mode a sine function is used to continuously vary the shunt inductance and resistance between a lower and upper value, corresponding with the lower and upper values of the frequency range of interest. Both single and multiple patch systems are presented and compared to the results obtained using fixed tuned shunted piezoelectric transducers. For the multiple patch configuration two control laws are proposed: series and parallel; in the first one the targeted frequency range is divided into sub-ranges and each absorber works in one of these sub-ranges, and in the parallel mode all the absorbers work on the whole frequency range but with a phase shift between them.

Chapter six presents a summary of the presented studies and suggests ideas for future work.

2

PIEZOELECTRIC TRANSDUCERS

This chapter presents a brief historical background concerning piezoelectricity in general and piezoceramic materials in particular. The working principle, fabrication and poling process are then introduced together with the material constitutive equations and the coefficients or parameters used to characterise a piezoelectric ceramic.

Contents

2.1 INTRODUCTION

Certain materials, often called smart materials by some authors, exhibit particular responses to physical stimuli of different nature[2]. Table 2.1 show some of these stimuli and the effects they produce, where the diagonal terms are the intrinsic properties that characterise the behaviour of the material. Piezoelectricity, highlighted in red in table 2.1, is a property of certain materials which generate internal electrical charges in response to a mechanical force. Pierre and Jacques Curie called this property the piezoelectric effect in 1880. The most common materials that exhibit this behaviour are crystals such as quartz and tourmaline. Later on, the Curie brothers experimentally confirmed what the physicist Gabriel Lippmann predicted in 1881: piezoelectricity is reversible process. This means that applying an electrical field to a piezoelectric material will produce internal mechanical strains.

Table 2.1.: Stimulus-response relations indicating various effects in materials from reference [2].

Output Input	Strain	Electric change	Magnetic flux	Temp.	Light
Stress	***Elasticity***	Piezo-electricity	Magneto-restriction		Photo-elasticity
Electric field	Piezo-electricity	***Permittivity***			Electro-optic effect
Magnetic field	Magneto-restriction	Magneto-electric	***Permeability***		Magneto optic effect
Heat	Thermal expansion	Pyro-electricity		***Specific heat***	
Light	Photo-striction	Photovoltaic effect			***Refractive index***

Following these discoveries piezoelectric materials were studied for around 30 years until the first application arrived during World War I: Paul Langevin and his colleagues built an ultrasonic submarine detector [44]. Extensive research and new applications appeared before and during World War II, many which are considered the classical applications of piezoelectric materials: resonators, accelerometers, microphones and other types of transducers. After the war, the USA, Japan and the Soviet Union discovered piezoceramic materials while trying to improve the properties of capacitor materials. These new synthetic materials exhibited dielectric constants up to 100 times the one of natural crystals; and the newly discovered piezoceramics showed similar improvements in the piezoelectric capacity.

Nowadays many piezoceramic materials are industrially produced with very interesting electromechanical properties for a wide range of applications: from sensors to measure heat, force, traffic, etc. to linear, shear and rotor actuators, energy harvesting, vibration and noise control, sound systems and many others. One of the most popular of these materials is the PZT, a relatively stiff, brittle and high density piezoceramic that was developed around 1952 in the Institute of Technology of Tokyo. A composite material worth mentioning is the MFC, developed by NASA around 1999, which in principle has higher performance and durability compared to traditional monolithic ceramic devices.

2.2 STRUCTURE OF PIEZOELECTRIC CERAMICS

Perovskite is a mineral compound with formula $CaTiO_3$ named after the Russian mineralogist Perovski. Perovskite is also used to name a group of crystals which have the same structure. Piezoceramic materials are composed of these perovskite crystals. Each crystal, as shown in figure 2.1, is composed of a cubic lattice with large metal ions on the corners, a small metal ion in the central position and oxygens in the centre of the faces [45].

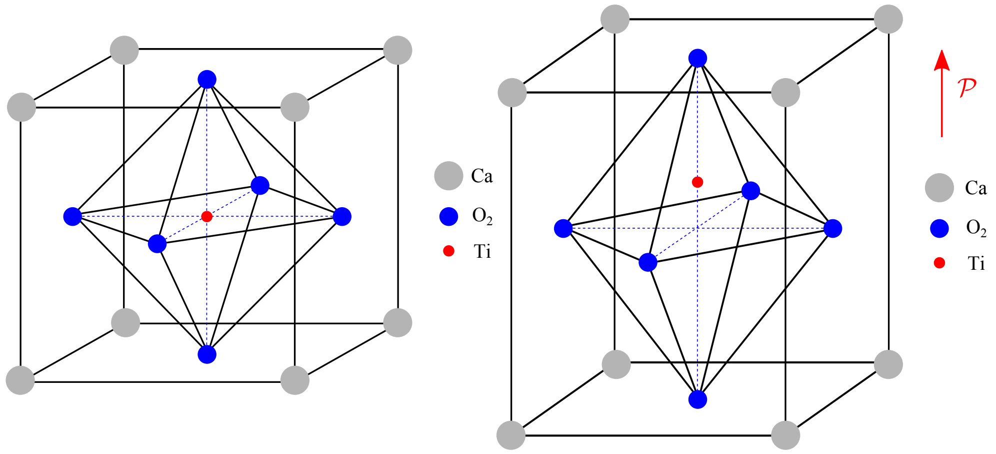

(a) $T>T_{Curie}$ (b) $T<T_{Curie}$

Figure 2.1.: (a) Unit cell with symmetrical, cubic Perovskite structure, and (b) tetragonally distorted unit cell [1].

Piezoceramic materials are produced by sintering a mixture of fine powders of metal oxides. The metal oxide powders are mixed in specific proportions, and then heated to obtain a uniform mixture. Binders are added to the mixture and specific shapes are formed with it, such as plates or discs. Then the sintering takes place: this shaped elements are heated at a specific temperature for an appropriate amount of time, enabling the formation of a dense crystalline structure, which after cooling can be cutted into particular shapes. The last step is adding the electrode layer to the proper surfaces of the ceramic. Figure 2.2 shows the typical structure of a piezoelectric patch, where the additional structural layer can be neglected.

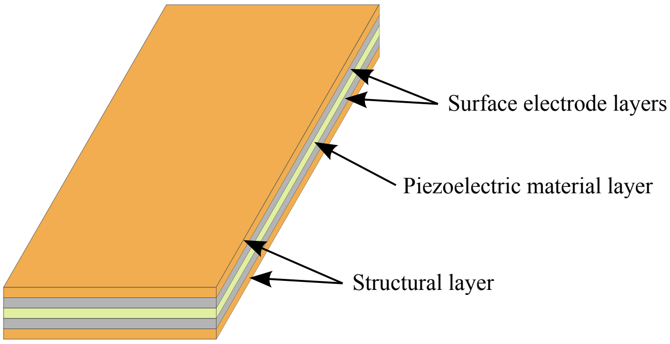

Figure 2.2.: General structure of a piezoceramic patch.

Plot (a) of figure 2.1 shows the lattice structure of a perovskite crystal at temperatures above the Curie temperature, in this case the crystal is symmetric and there is no dipole moment and no other piezoelectric properties. But once the material starts to cool down, below the Curie temperature, the lattice becomes deformed and asymmetric (or tetragonal symmetric[1]) which results in the formation of dipoles, as shown in plot (b) where the red P indicates the polarization direction. This type of ceramic is usually called ferroelectric ceramic, and presents spontaneous polarization. These dipoles, when aligned in the same orientation, create regions with a particular polarization called ferroelectric domain. However, no macroscopic piezoelectric behaviour is noticed as the distribution of this domains is random, as shown in plot (a) of figure 2.3.

Then, the ceramic element is exposed to a strong DC electric field (of up to several kV/mm) to align the ferroelectric domains. This process is called *poling*, and it is usually performed after heating the ceramic just below its Curie temperature. This process is analogous to the magnetizing of a permanent magnet

---

[1] Tetragonal symmetry refers to symmetric crystals that are stretched along one of its lattice vectors, e.g. a cube of dimensions $a \times a \times a$ is stretched into a prism of dimensions $a \times a \times h$.

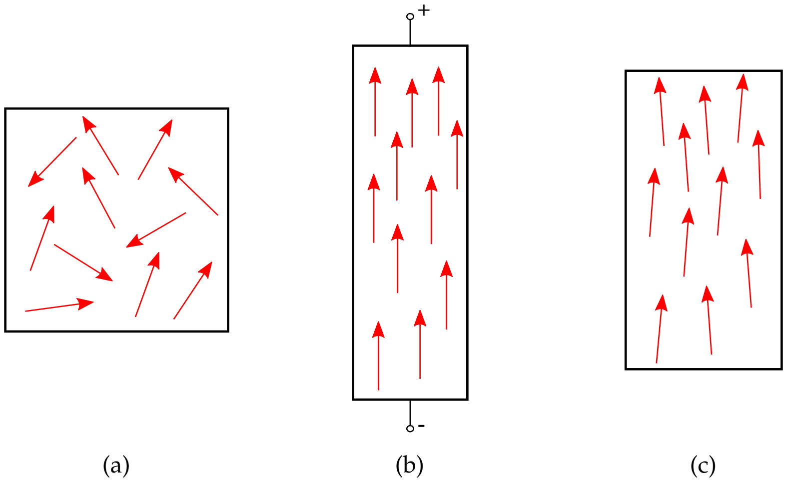

Figure 2.3.: Polar domains (a) before the poling process, (b) during poling, and (c) after poling.

[45]. During the poling process the domains are aligned, as shown in plot (b) of figure 2.3, and those that were oriented as the electric field grow and the others shrink. Plot (c) in the other hand shows the ceramic element polarization after the poling process, i.e. once the electric field is removed and the material is cooled down at normal temperature. It can be seen that the domains remain reoriented and are now aligned. They are not perfectly aligned due to internal mechanical stresses; however it is sufficient to produce a permanent polarization P_r and an expansion S_r of the ceramic element. Anyway, the length increase is very small, within the micrometer range [44].

The remnant polarization P_r can be degraded if the mechanical, thermal or electrical limits of the material are exceeded. Figure 2.4 shows typical hysteresis curves for the deformation and polarization versus the applied electric field. Plot (a) shows that as the electric field increases, so does the element deformation. Decreasing the electric field also produces a decrease of the deformation; but when the electric field iz zero it can be seen the remnant deformation S_r. Then, applying an increasing negative electric field shrinks the element up to a minimum and then it starts to lengthen again as the amplitude of the negative field increases. This effect is caused by the re-polarization of the domains, once they change orientation due to the negative electric field the element stops shrinking and starts to lengthen again. It may be also interesting to study the hysteresis curve for an unipolar electric field, i.e. E does not changes sign. In this case, once the electric field amplitude decreases, arrives to zero and the

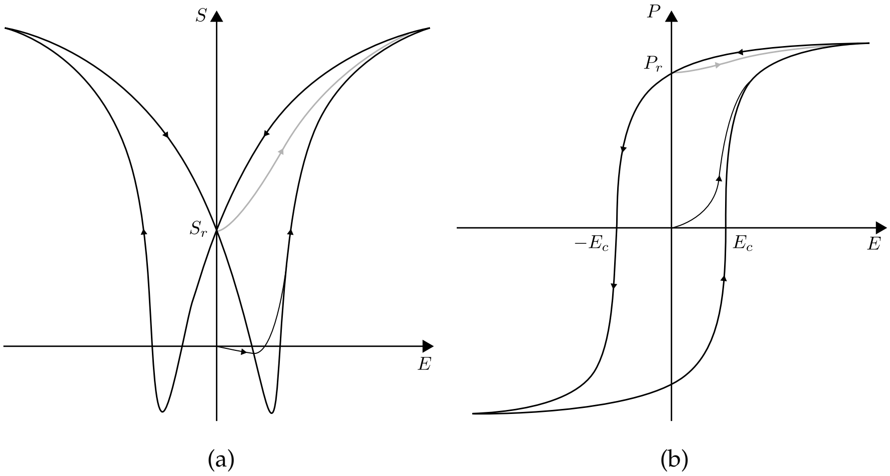

Figure 2.4.: Typical hysteresis loop of (a) deformation and (b) polarization versus applied field [1].

remnant deformation S_r is achieved, the electric field amplitude starts to rise again describing the curve presented with the solid gray line.

Plot (b) of figure 2.4 shows the hysteresis curve of polarization versus electric field, which shows a classical hysteresis curve. Here, it can be seen that a negative electric field will depolarize the material if it exceeds the coercivity strength E_c, and if the amplitude of the negative field continues to increase the material will be polarized in the opposite direction considering with respect to the original one. As in plot (a), the solid gray line in plot (b) shows the curve for an unipolar electric field.

Figures 2.5 and 2.6 show the behaviour of a poled piezoceramic element when subjected to mechanical and electrical stimuli respectively. Plot (a) in both figures shows a poled piezoceramic cylindrical element at rest. Plot (b) of figure 2.5 presents the same element subjected to mechanical compression along the polarization direction, this generates a voltage of the same polarity as the poling voltage. As shown in plot (c), if the element is subjected to a mechanical tension along the polarization direction, or compression perpendicular to that direction, a voltage is generated with opposite polarity to the poling voltage. In this configuration the element is being used as a sensor, converting mechanical energy into electrical energy.

Plot (b) of figure 2.6 shows the piezoceramic element subjected to an external voltage with the same polarity and in the same direction as the poling voltage, this produces internal mechanical tensions resulting in a deformation of the element: it becomes longer and its diameter is reduced. In plot (c), the element

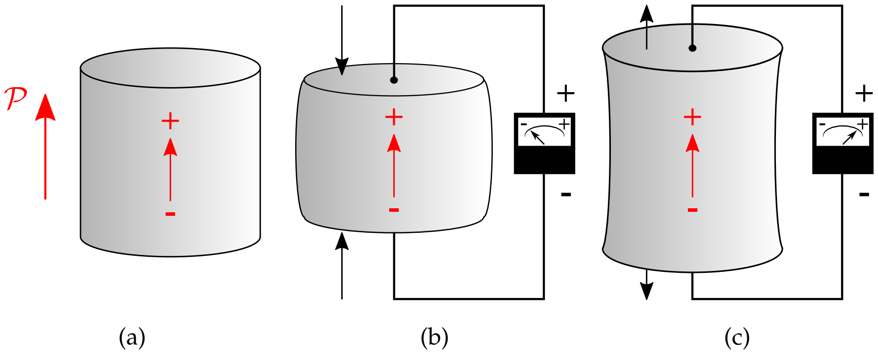

Figure 2.5.: (a) Polarized piezoelectric element (b) subjected to compression forces and (c) to traction forces.

is subjected to a an external voltage with the same direction but opposite polarity as the poling voltage, this also produces internal mechanical stresses that deform the element but in this case it shortens and its diameter increases. Operating in this way, it is said the element is used as an actuator: converting the electrical energy delivered by the power supply into mechanical energy.

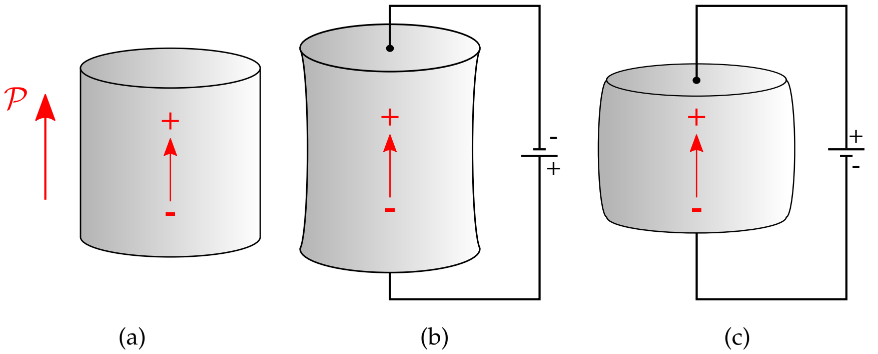

Figure 2.6.: (a) Polarized piezoelectric element connected to a voltage source with (b) the same and (c) opposite polarity as the poling voltage.

In both cases, using the piezoceramic as sensor or actuator, the relation between applied stress/voltage and the resulting voltage/strain is linearly proportional up to a specific stress/voltage determined by the material properties [44]. If operated under high electrical fields or mechanical stresses, considerable non linearities will be introduced. It is assumed here that the piezoelectric materials are linear, working under low voltages and low mechanical stress.

2.3 CONSTITUTIVE EQUATIONS OF A PIEZOELECTRIC TRANSDUCER

The stress/strain relations of a piezoelectric material are obtained assuming that the total strain of the transducer is the sum of the strain induced by the mechanical stress and the strain caused by the voltage applied to the transducer. Figure 2.7 shows a piezoelectric transducer with the polarization direction and the principal reference system used in the following formulation.

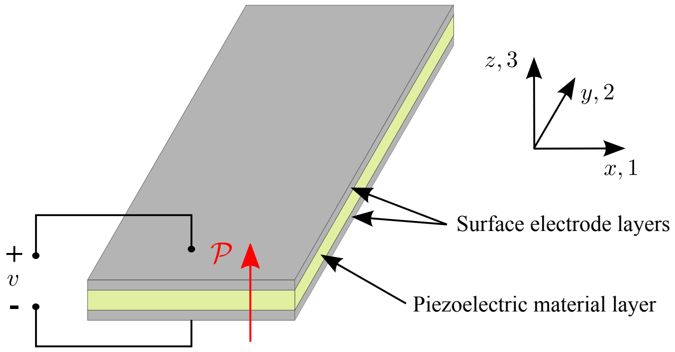

Figure 2.7.: Piezoelectric transducer diagram.

A contracted notation, known as Voigt-Kelvin notation [46] is used, which is presented in table 2.2 where $1, 2, 3$ are respectively the axes x, y, z and the shear components around axes x, y, z are given by $4, 5, 6$. Figure 2.7 shows that the polarization of the transducer has the same direction as axis 3.

Table 2.2.: Contracted notation.

Axis	Notation
x	1
y	2
z	3
Shear around x	4
Shear around y	5
Shear around z	6

Then, the normal stress and shear stress components are given respectively by equations (2.1a) and (2.1b).

$$T_1 = T_{11} \quad T_2 = T_{22} \quad T_3 = T_{33} \tag{2.1a}$$

$$T_4 = T_{23} \quad T_5 = T_{31} \quad T_6 = T_{12} \tag{2.1b}$$

$$\begin{aligned} S_1 &= S_{11} \\ S_2 &= S_{22} \\ S_3 &= S_{33} \end{aligned} \quad \text{(2.2a)} \qquad \begin{aligned} S_4 &= 2S_{23} \\ S_5 &= 2S_{31} \\ S_6 &= 2S_{12} \end{aligned} \quad \text{(2.2b)}$$

The pure extension and shear strains are given by (2.2a) and (2.2b) respectively. The stresses T_{ij} and strains S_{ij} have the typical denotation used in theory of elasticity [47].

Then, the constitutive equations for the piezoelectric transducer presented in figure 2.7 are given by [2]

$$D_m = \varepsilon^{\mathrm{T}}_{ik} E_k + d_{mi} T_i \tag{2.3}$$

$$S_i = d_{im} E_m + s^{\mathrm{E}}_{ij} T_j \tag{2.4}$$

where the sub-indexes $i, j = 1, \ldots, 6$ and $m, k = 1, 2, 3$ refer to different directions as indicated in table 2.2 and figure 2.7. Also, D is the electric displacement, E is the electric field, T is the stress, S is the strain, ε^{T} is the permittivity under constants stress, d_{mi} is the piezoelectric strain constant and s^{E} is the compliance under constant electric field.

If there is sensing involved in the application, then equations (2.3) and (2.4) are re-written into the following form [44]

$$S_i = s^{\mathrm{D}}_{ij} T_j + g_{mi} D_m \tag{2.5}$$

$$E_i = g_{mi} T_i + \beta^{\mathrm{T}}_{ik} D_k \tag{2.6}$$

where s^{D} is the compliance under constant electric displacement, g_{mi} is the piezoelectric voltage constant and β^{T} is the impermittivity under constant stress.

Then, writing equations (2.3) and (2.4) in matrix form the following expressions are obtained

$$\begin{bmatrix} D_1 \\ D_2 \\ D_3 \end{bmatrix} = \begin{bmatrix} \varepsilon^{\mathrm{T}}_{11} & \varepsilon^{\mathrm{T}}_{12} & \varepsilon^{\mathrm{T}}_{13} \\ \varepsilon^{\mathrm{T}}_{21} & \varepsilon^{\mathrm{T}}_{22} & \varepsilon^{\mathrm{T}}_{33} \\ \varepsilon^{\mathrm{T}}_{31} & \varepsilon^{\mathrm{T}}_{32} & \varepsilon^{\mathrm{T}}_{33} \end{bmatrix} \begin{bmatrix} E_1 \\ E_2 \\ E_3 \end{bmatrix} + \begin{bmatrix} d_{11} & d_{12} & d_{13} & d_{14} & d_{15} & d_{16} \\ d_{21} & d_{22} & d_{33} & d_{24} & d_{25} & d_{26} \\ d_{31} & d_{32} & d_{33} & d_{34} & d_{35} & d_{36} \end{bmatrix} \begin{bmatrix} T_1 \\ T_2 \\ T_3 \\ T_4 \\ T_5 \\ T_6 \end{bmatrix} \tag{2.7}$$

$$
\begin{bmatrix} S_1 \\ S_2 \\ S_3 \\ S_4 \\ S_5 \\ S_6 \end{bmatrix}
=
\begin{bmatrix}
s^{E}_{11} & s^{E}_{12} & s^{E}_{13} & s^{E}_{14} & s^{E}_{15} & s^{E}_{16} \\
s^{E}_{21} & s^{E}_{22} & s^{E}_{33} & s^{E}_{24} & s^{E}_{25} & s^{E}_{26} \\
s^{E}_{31} & s^{E}_{32} & s^{E}_{33} & s^{E}_{34} & s^{E}_{35} & s^{E}_{36} \\
s^{E}_{41} & s^{E}_{42} & s^{E}_{43} & s^{E}_{44} & s^{E}_{45} & s^{E}_{46} \\
s^{E}_{51} & s^{E}_{52} & s^{E}_{53} & s^{E}_{54} & s^{E}_{55} & s^{E}_{56} \\
s^{E}_{61} & s^{E}_{62} & s^{E}_{63} & s^{E}_{64} & s^{E}_{65} & s^{E}_{66}
\end{bmatrix}
\begin{bmatrix} T_1 \\ T_2 \\ T_3 \\ T_4 \\ T_5 \\ T_6 \end{bmatrix}
+
\begin{bmatrix}
d_{11} & d_{21} & d_{31} \\
d_{12} & d_{22} & d_{32} \\
d_{13} & d_{23} & d_{33} \\
d_{14} & d_{24} & d_{34} \\
d_{15} & d_{25} & d_{35} \\
d_{16} & d_{26} & d_{36}
\end{bmatrix}
\begin{bmatrix} E_1 \\ E_2 \\ E_3 \end{bmatrix}
\tag{2.8}
$$

Considering a transversely isotropic material, which is true for piezoceramic materials, and assuming that it is poled along axis 3, some of the matrix coefficients in equations (2.7) and (2.8) will be zero. The mechanical coefficients different than zero are:

$$s^{E}_{11} = s^{E}_{22} \tag{2.9}$$

$$s^{E}_{13} = s^{E}_{31} = s^{E}_{23} = s^{E}_{32} \tag{2.10}$$

$$s^{E}_{12} = s^{E}_{21} \tag{2.11}$$

$$s^{E}_{44} = s^{E}_{55} \tag{2.12}$$

$$s^{E}_{66} = 2(s^{E}_{11} - s^{E}_{12}) \tag{2.13}$$

$$\tag{2.14}$$

While the non-zero electric coefficients are

$$d_{31} = d_{32} \tag{2.15}$$

$$d_{15} = d_{24} \tag{2.16}$$

$$d_{33} \tag{2.17}$$

$$\varepsilon^{T}_{11} = \varepsilon^{T}_{22} \tag{2.18}$$

$$\varepsilon^{T}_{33} \tag{2.19}$$

Re-writing (2.7) and (2.8) the following simplified expressions are obtained

$$\begin{bmatrix} D_1 \\ D_2 \\ D_3 \end{bmatrix} = \begin{bmatrix} \varepsilon_{11}^{\mathrm{T}} & 0 & 0 \\ 0 & \varepsilon_{11}^{\mathrm{T}} & 0 \\ 0 & 0 & \varepsilon_{33}^{\mathrm{T}} \end{bmatrix} \begin{bmatrix} E_1 \\ E_2 \\ E_3 \end{bmatrix} + \begin{bmatrix} 0 & 0 & 0 & 0 & d_{15} & 0 \\ 0 & 0 & 0 & d_{15} & 0 & 0 \\ d_{31} & d_{31} & d_{33} & 0 & 0 & 0 \end{bmatrix} \begin{bmatrix} T_1 \\ T_2 \\ T_3 \\ T_4 \\ T_5 \\ T_6 \end{bmatrix} \tag{2.20}$$

$$\begin{bmatrix} S_1 \\ S_2 \\ S_3 \\ S_4 \\ S_5 \\ S_6 \end{bmatrix} = \begin{bmatrix} s_{11}^{\mathrm{E}} & s_{12}^{\mathrm{E}} & s_{13}^{\mathrm{E}} & 0 & 0 & 0 \\ s_{12}^{\mathrm{E}} & s_{11}^{\mathrm{E}} & s_{13}^{\mathrm{E}} & 0 & 0 & 0 \\ s_{13}^{\mathrm{E}} & s_{13}^{\mathrm{E}} & s_{33}^{\mathrm{E}} & 0 & 0 & 0 \\ 0 & 0 & 0 & s_{44}^{\mathrm{E}} & 0 & 0 \\ 0 & 0 & 0 & 0 & s_{44}^{\mathrm{E}} & 0 \\ 0 & 0 & 0 & 0 & 0 & s_{66}^{\mathrm{E}} \end{bmatrix} \begin{bmatrix} T_1 \\ T_2 \\ T_3 \\ T_4 \\ T_5 \\ T_6 \end{bmatrix} + \begin{bmatrix} 0 & 0 & d_{31} \\ 0 & 0 & d_{31} \\ 0 & 0 & d_{33} \\ 0 & d_{15} & 0 \\ d_{15} & 0 & 0 \\ 0 & 0 & 0 \end{bmatrix} \begin{bmatrix} E_1 \\ E_2 \\ E_3 \end{bmatrix} \tag{2.21}$$

It must be noted that equations (2.20) and (2.21) are valid for piezoelectric ceramic materials such as PZT. Instead, for piezoelectric polymers such as PVDF a different set of simplified equations must be used as this material is not isotropic on the surface plane.

For simplicity the following notation will be used in the next chapters: plain characters will be used to indicate scalar quantities while bold characters represent matrices and vector; e.g. equations (2.7) and (2.8) can be written in the following form:

$$\begin{bmatrix} \mathbf{D} \\ \mathbf{S} \end{bmatrix} = \begin{bmatrix} \boldsymbol{\varepsilon}^{\mathrm{T}} & \mathbf{d} \\ \mathbf{d}^{T} & \mathbf{s}^{\mathrm{E}} \end{bmatrix} \begin{bmatrix} \mathbf{E} \\ \mathbf{T} \end{bmatrix} \tag{2.22}$$

where the super-index ^{T} indicates the transpose.

2.4 PIEZOELECTRIC MATERIAL COEFFICIENTS

This section explains some of the most important parameters that characterize a piezoelectric material and that will be of use in the next chapters. Some of the piezoelectric coefficients are defined using a set of two sub-index *ij* and sometimes a super-index is also needed to indicate a mechanical or electrical boundary. The first sub-index i is indicates the direction of action of an electric parameter (e.g the electric field, the voltage or the charge density) while the second sub-index j is related to the direction of action of a mechanical parameter such as the strain or stress. The mechanical and electrical constraints indicated by a super-index are shown in table.

Table 2.3.: Super-indexes indicating mechanical and electrical constraints.

Super-index	Description
^{T} = constant stress	Transducer mechanically free
^{E} = constant electric field	Transducer in short circuit
^{D} = constant electric displacement	Transducer in open circuit
^{S} = constant strain	Transducer mechanically clamped

2.4.1 *Piezoelectric strain constants*

The piezoelectric strain/charge constant is represented by d_{ij}, where the sub-index ij means that the electric field is applied or the charge is collected in the i direction for a displacement or a force produced in the j direction. There are then two interpretations of this constant:

1. it is the ratio between the produced strain and the applied electrical field when external stresses are constant:

$$d_{ij} = \frac{S_j}{E_i} \quad [m/V] \tag{2.23}$$

2. it represents the ratio between the charge density flowing through short circuited electrodes perpendicular to the j direction and the stress applied in the i direction:

$$d_{ij} = \frac{Q_i^{E}}{T_j} \quad [C/N] \tag{2.24}$$

   where Q^{E} is the charge density flowing through the electrodes in short circuit.

Something important to note is that large d_{ij} constants indicate large mechanical displacements, which are usually desired for actuators.

2.4.2 *Piezoelectric voltage constants*

This constant relates the electric field produced in the i direction for a mechanical stress applied in the j direction or the strain produced in the j direction for a charge density applied in the i direction. Then, also here there are two interpretations:

1. it is the ratio between the produced electric field with the electrodes in open circuit and the applied mechanical stress:

$$g_{ij} = \frac{E_i^{\mathrm{E}}}{T_j} \quad [Vm/N] \tag{2.25}$$

2. it also represents the ratio between the produced strain in the j direction and the charge density applied in the i direction under constant stress:

$$g_{ij} = \frac{S_j}{Q_i} \quad \left[m^2/C\right] \tag{2.26}$$

   where Q is the charge density applied to the electrodes.

In this case, large g_{ij} coefficients relates to higher output voltages, which is usually desired for sensors.

2.4.3 *Piezoelectric stress constants*

This constants are the inverse of the piezoelectric voltage constants, which means they also relate the mechanical stress produced in the i direction for an electric field applied in the j direction or the charge density produced in the j direction for a strain applied in the i direction. Then, this two interpretations are formulated as:

1. the ratio between the produced mechanical stress and the applied electric field under constant strain:

$$e_{ij} = \frac{E_i^{\mathrm{T}}}{E_j} \quad [Vm/N] \tag{2.27}$$

2. the ratio between the produced strain in the j direction and the charge density applied in the i direction with the electrodes in short circuit:

$$e_{ij} = \frac{S_j}{Q_i} \quad \left[m^2/C\right] \tag{2.28}$$

2.4.4 *Elastic compliance*

The elastic compliance coefficients s_{ij} give the ratio of the strain in the i direction produced by the stress applied in the j direction assuming that the stress along the other directions remains the same. For example, s_{21} indicates the direct strain in direction 2 produced by a stress along direction 1 and s_{66} represents the shear strain around direction 6 due to a shear stress applied around the same axis.

As a mechanical stress produce an electrical response that can increase the resultant strain, the elastic compliance matrix can be defined as under constant electric field $\mathbf{s}^{\mathrm{E}}$ or constant electric displacement $\mathbf{s}^{\mathrm{D}}$. It would be expected that a short-circuited piezoelectric patch has a smaller Young's modulus of elasticity than when it is in open circuit, as $\mathbf{s}^{\mathrm{E}}$ would be smaller than $\mathbf{s}^{\mathrm{D}}$ [44].

2.4.5 *Permittivity*

The permittivity coefficient ε_{ij} indicates the charge density in the i direction produced by an electric field applied along the j direction. This coefficient can be expressed under constant stress $\varepsilon^{\mathrm{T}}_{pe}$ or constant strain $\varepsilon^{\mathrm{S}}_{pe}$. Sometimes the manufacturers provide a relative permittivity ε_r of the material, in this case the absolute value is given by

$$\varepsilon = \varepsilon_r \varepsilon_0 \tag{2.29}$$

where ε_0 is the permittivity of the free space defined as

$$\varepsilon_0 \approx 8.8542 \times 10^{-12} \mathrm{F/m} \tag{2.30}$$

2.4.6 *Capacitance*

Piezoceramic patches such as the one depicted in figure 2.7 have an inherent capacitance C_{pe}. However, unlike the permittivity, which is a property of the material itself, C_{pe} depends not only of the material but also of the patch dimensions. The capacitance can be obtained analytically using the following expression [2]

$$C_{pe} = \frac{\varepsilon^{\mathrm{T}} A_{pe}}{h_{pe}} \tag{2.31}$$

where A_{pe} and h_{pe} are the surface area and thickness of the piezoelectric patch.

2.4.7 *Electromechanical coupling factor*

The piezoelectric electromechanical coupling coefficient k_{ij} indicates the efficiency with which a piezoelectric material converts mechanical energy into electrical and vice versa. It can be calculated analytically [2, 21, 44, 45] and it can be measured experimentally in different ways involving measurements of specific parameters with the transducer in open and short circuit [21, 44]. For example, for a mechanically free piezoelectric ceramic that is strained along direction 1 due to a voltage applied along direction 3 the ratio between the stored mechanical energy and the applied electrical energy is represented by k_{31}^2.

2.5 CHAPTER CONCLUDING REMARKS

This chapter presented some historical facts regarding piezoelectric materials, in particular piezoceramics. A general overview of the structure and fabrication process of a piezoceramic was given, including the poling process. The direct and inverse piezoelectric effect were explained showing how a piezoceramic element could be used as an actuator or as a sensor.

Then, the piezoelectric material constitutive equations were introduced in their general form. A simplified, reduced form was also presented for a PZT material, one of the most common types of piezoceramic materials.

The last section of this chapter addressed the coefficients that characterise a piezoelectric material, focusing on the parameters used in the following chapters.

3

VELOCITY FEEDBACK LOOP USING PIEZOELECTRIC TRANSDUCERS

This chapter presents an active vibration control study in which decentralized velocity feedback loops are implemented on a thin rectangular aluminium panel using piezoelectric transducers with a specific shape. The stability and control performance of the system is analysed through simulations and experimentally implementing either one or five control loops.

The feedback loop is composed of a piezoelectric patch actuator with an accelerometer sensor at its centre. The actuator itself is made of six triangular anisotropic piezoelectric patches assembled into an hexagonal patch. This particular type of shaped piezoelectric patch produces bending moments along its edges and a net transverse force at its centre, balanced by opposite point forces at the six vertices of the hexagon.

Contents

3.1 INTRODUCTION

Prototype smart panels with multiple velocity feedback control loops were developed during the last two decades using inertial point force actuators [48, 49] and piezoelectric actuators bonded on the panel [13, 50] with collocated accelerometer sensors. Thin structures are characterised, at low frequencies, by low flexural modal overlap, which means that their flexural response is due to the resonances of low order modes; which are effectively controlled by control systems implementing velocity feedback loops [51]. Also, Elliot et al. [52] showed that an array of local velocity feedback loops is unconditionally [53–55] stable with a proper choice of actuators and sensors. The feedback loops produce a sky-hook damping that can reduce the overall flexural response of the panel [56]. Furthermore, the use of piezoelectric actuators to implement the velocity feedback loop seemed quite promising due to the possibility of producing compact sandwich structures [2, 6, 9, 57]. Nevertheless, as the velocity feedback loop was affected by stability issues [14, 58] its practical implementation was not straightforward. This problem could be traced to two physical phenomena:

- the piezoelectric patch produces a bending excitation field that is not collocated with the accelerometer sensor [59], and
- the strength of the bending excitation field produced by the piezoelectric patch tends to increase with frequency [60, 61].

These two concurrent phenomena produce delayed control signals components with high amplitude at higher frequencies, which leads to instability.

This study deals with the vibration control effects produced by a single velocity feedback loop located at the centre of a simply supported panel, and by five velocity feedback loops positioned at the centre and diagonals of the panel. Arrays of velocity feedback loops have been proven to produce large control effects [62], but a single unit can also produce good reductions if it is located in a key position like the centroid of a thin structure, and in this way coupling with all volumetric modes [63, 64]. In addition, velocity feedback loops using piezoelectric patch actuators have stability drawbacks because of the non collocated actuation effects generated at the edges of the patches. Nevertheless, several studies have shown that the shape of the piezoelectric patch has a strong effect on its active damping capability when implementing a velocity feedback loop [65]. Particular shapes can improve the stability of the loop, which leads to a better control performance [66].

The proposed hexagonal actuator is composed of six triangular macro fiber composite (MFC) [67] leafs with their principal axis aligned along the lateral edge of the hexagon and the radial direction. A single input-single output (SISO) control system is considered first, in which the MFC patch [68] is located at the centre of the panel and the error velocity sensor at the centre of the hexagon. The open and close loop response of the control system has been modelled and analysed. Also, a prototype was built to confirm the theoretical predictions. The closed loop response of the prototype was assessed off-line using the measured FRFs. This means that after these FRFs were acquired and stored, they were used in Matlab to produce the closed loop response.

Then, a decentralized multiple inputs-multiple outputs (MIMO) control system using five MFC hexagonal actuators is studied, following an approach similar to the one presented in [48] for five proof mass electrodynamic actuators and in [50] for 16 piezoelectric actuators. Also for the MIMO control system a model was developed to assess its open and closed loop responses and a prototype was built to confirm the results. Also here the prototype closed loop response was analysed off-line in Matlab using measured data.

3.2 VELOCITY FEEDBACK WITH MFC HEXAGONAL PATCH

The relevant geometrical and physical properties of the simply supported panel are summarized in table 3.1, and in table 3.2 for the MFC patch.

Table 3.1.: Dimensions and physical properties of the panel.

Parameter	Value	Units
Thickness	$h_p = 0.8$	mm
Width	$l_y = 0.314$	m
Length	$l_x = 0.414$	m
Aluminium Density	$\rho_p = 2700$	m^3
Young's Modulus	$E_p = 70 \times 10^9$	N/m^2
Poisson's ratio	$\nu_p = 0.33$	

The MFC is made of rectangular ceramic rods stacked between layers of electrodes, adhesive and polyimide film. The electrodes are attached to the film using an interdigitated pattern that transfers the applied voltage to and from the ribbon shaped rods. This type of actuators are more robust and flexible compared to standard monolithic piezoelectric patches. A general arrangement of an MFC transducer [69] is shown in figure 3.1, where the top and bottom layers

Table 3.2.: Dimensions and physical properties of the actuator.

Parameter	Value	Units
Thickness	$h_{pe} = 0.4$	mm
Leafs height	$a = 0.0173$	m
Leafs base	$b = 0.02$	m
Hexagon diagonal	$d = 0.04$	m
Density	$\rho_{pe} = 7600$	m^3
Young's Modulus	$E_{pe} = 90 \times 10^9$	N/m^2
Poisson's ratio	$\nu_{pe} = 0.35$	
Strain/charge constants	$d_{31} \approx 0$	m/V
	$d_{32} = 166 \times 10^{-12}$	m/V
	$d_{36} \approx 0$	m/V

of polyimide with the interdigitated electrode pattern can be seen; and between these layer the structural epoxy matrix containing the rectangular piezoelectric fibers.

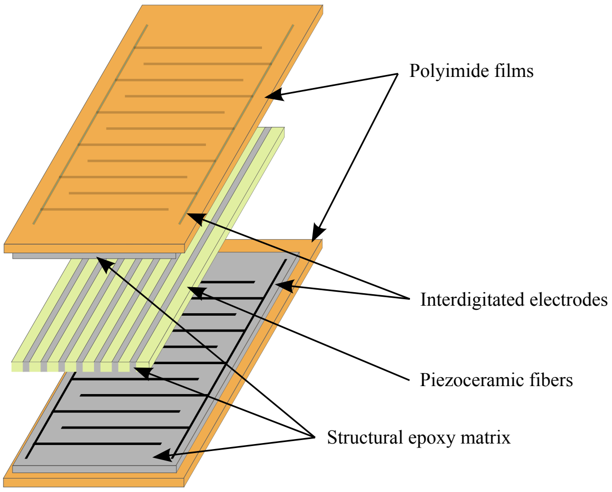

Figure 3.1.: General arrangement of an MFC patch.

3.2.1 *Excitation field*

Figure 3.2 shows the transverse force $p(x, y)$, flexural moments M_{nn}, shear moments M_{tn} and shear force t_{nz} distributions produced by a thin orthotropic patch bonded on a panel. For clarity only a portion of the smart panel is shown, where also the surface Ω and contour Γ can be seen. Figure 3.3 on the other hand, shows a cross section of the panel and piezoelectric transducer, where the variable h_s is the distance between the mid-planes of the panel and of the patch and is defined as

$$h_s = \frac{h_p + h_{pe}}{2} \tag{3.1}$$

where h_p is the thickness of the panel and h_{pe} is the thickness of the patch.

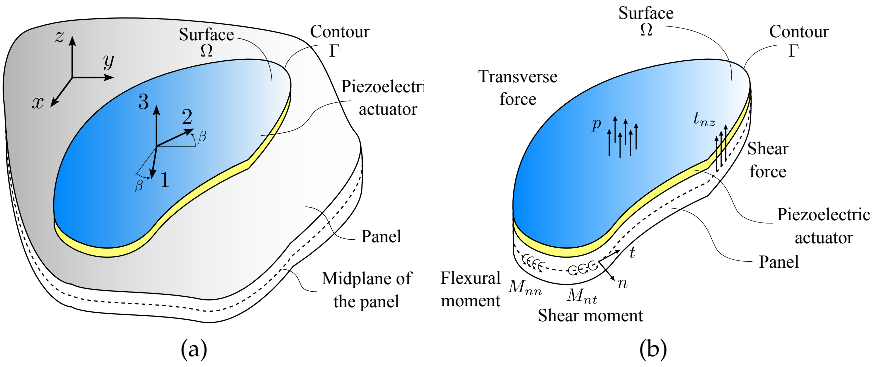

(a) (b)

Figure 3.2.: (a) Thin plate with a bonded piezoelectric transducer and (b) detailed section with the forces and moments produced by the patch.

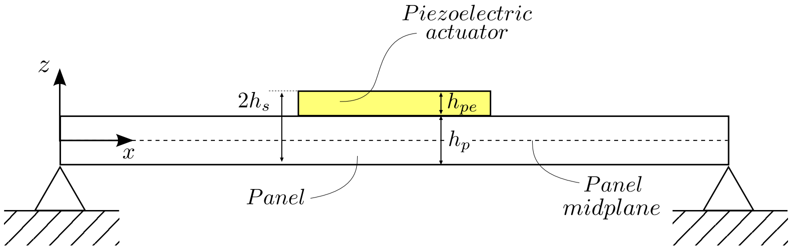

Figure 3.3.: Cross section of the panel and piezoelectric actuator.

Then, the equations of motion for the flexural response of a thin flat panel with a bonded piezoelectric transducer can be written as [70, 71]:

$$\begin{aligned} &\frac{Y_p h_p^3}{12(1-\nu_p^2)}\left(\frac{\partial^4 w}{\partial x^4} + 2\frac{\partial^4 w}{\partial x^2 \partial y^2} + \frac{\partial^4 w}{\partial y^4}\right) + \rho_p h_p \frac{\partial^2 w}{\partial t^2} + \\ &\frac{h_p}{2}\delta_{ep}\left(e_{31}\frac{\partial^2 S}{\partial x^2} + 2e_{36}\frac{\partial^2 w}{\partial x \partial y} + e_{32}\frac{\partial^2 S}{\partial y^2}\right) v_c = 0 \end{aligned} \tag{3.2}$$

where Y_p, ν_p and ρ_p are respectively the Young's modulus, the Poisson's ratio and the density of the panel, v_c is the voltage applied to the transducer, w is the transverse displacement of the panel, δ_{ep} is a function whose value is equal to 1 or -1 depending on whether the electric field and the poling direction have the same or opposite directions, $S(x,y)$ is the spatial sensitivity function which provides the spatial coupling between the structure and the piezoelectric transducer and is given by

$$S(x,y) = F(x,y)P_0(x,y) \tag{3.3}$$

where $F(x,y)$ is the effective surface electrode function and $P_0(x,y)$ is the poling strength function assumed the same in directions 1, 2 and 6. Finally, the stress constants e_{ij}, defined in section 2.4.3 are given by:

$$\begin{bmatrix} e_{31} \\ e_{32} \\ e_{36} \end{bmatrix} = \begin{bmatrix} m^2 & n^2 & -2mn \\ n^2 & m^2 & 2mn \\ mn & -mn & m^2-n^2 \end{bmatrix} \frac{Y_{pe}}{1-\nu_{pe}^2} \begin{bmatrix} 1 & \nu_{pe} & 0 \\ \nu_{pe} & 1 & 0 \\ 0 & 0 & \frac{1-\nu_{pe}}{2} \end{bmatrix} \begin{bmatrix} d_{31} \\ d_{32} \\ d_{36} \end{bmatrix} \tag{3.4}$$

where $m = \cos(\beta)$, $n = \sin(\beta)$ and β is the angle between the axes x and y of the main reference system and the axes 1 and 2 of the piezoelectric material, as shown in plot (a) of figure 3.2. Also, Y_{pe} and ν_{pe} are respectively the Young's modulus and the Poisson's ratio of the transducer material and d_{ij} are the piezoelectric strain constants defined in section 2.4.1, which are provided in table 3.2.

The equivalent distributed flexural actuation effects produced by the three piezoelectric patches are obtained using the formulation proposed by Deraemaeker et al. [72], they derived the following expressions for the loads produced by a piezoelectric patch bonded on a plate:

$$-p(x,y) = \frac{\partial^2}{\partial x^2}(h_s e_{31} v_c) + \frac{\partial^2}{\partial y^2}(h_s e_{32} v_c) + 2\frac{\partial^2}{\partial x \partial y}(h_s e_{36} v_c) \tag{3.5}$$

$$-M_{nn} = (e_{31}n_x^2 + e_{32}n_y^2 + 2e_{36}n_x n_y)h_s v_c \tag{3.6}$$

$$\begin{aligned} -\left[-\frac{\partial M_{nt}}{\partial s} + t_{nz}\right] = & \left\{(e_{32}-e_{31})\left[n_x n_y\right]_i + 2e_{36}\left[n_x^2\right]_i\right\}h_s v_c + \\ & \frac{\partial}{\partial s}\left\{\left[(e_{32}-e_{31})n_x n_y + 2e_{36}n_x^2\right]h_s v_c\right\} + \frac{\partial}{\partial x}(h_s e_{31} v_c)n_x + \\ & \frac{\partial}{\partial y}(h_s e_{32} v_c)n_y + 2\frac{\partial}{\partial x}(h_s e_{36} v_c)n_y \end{aligned} \tag{3.7}$$

where $\left[n_x^2\right]$ and $\left[n_x n_y\right]$ are the discontinuity jumps of n_x^2 and $n_x n_y$ where n_x and n_y are the x and y components of the unit vector $\mathbf{n}$ normal to the contour Γ. Also, $\partial(\dots)/\partial s$ is the derivative with respect to the curvilinear coordinate s along the contour Γ. As shown in figure 3.2, the term $p(x,y)$ represents a surface pressure excitation, only present if the patch stress/charge properties or the applied voltage have a non uniform distribution across the surface of the electrodes. The second term M_{nn} gives the flexural moments distributed along the contour Γ with vector orientation parallel to the tangent of Γ. The third term represents the shear forces occurring along the discontinuity points of Γ.

The MFC hexagonal patch is composed of six triangular leafs with the principal axis oriented along the lateral edge of the hexagon and the radial direction, as shown in figure 3.4. The response of the hexagonal patch is obtained by adding the effects of all six triangular leaf.

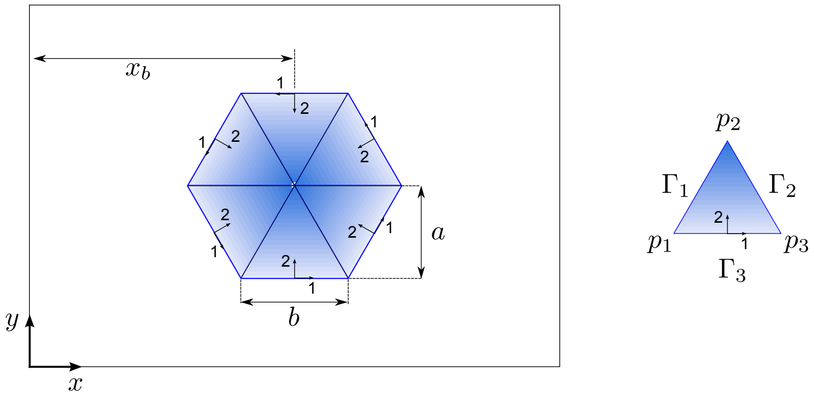

Figure 3.4.: Rectangular panel with an hexagonal MFC patch.

For simplicity an isosceles triangular leaf with the base aligned with the x axis is considered, with principal axes 1 and 2 parallel to the axes x and y of the plate. Then, the contour function Γ that delimits the surface of the triangular leaf is described by

$$\begin{aligned} &\Gamma_{1,2} \qquad x(y) = x_b \mp \frac{b}{2} \pm my && \mathit{for} \quad y \in \left[0\,,\, a\right] \\ &\Gamma_{1,3} \qquad y(x) = 0 && \mathit{for} \quad x \in \left[x_b - \frac{b}{2}\,,\, x_b + \frac{b}{2}\right] \end{aligned} \tag{3.8}$$

where a and b are the triangular leaf height and base dimensions, presented in table 3.2 and shown in figure 3.4 where also x_b is shown. These three segments are connected at the following discontinuity points:

$$p_1(x,y) = (x_b - \frac{b}{2}, 0) \tag{3.9}$$

$$p_2(x,y) = (0, a) \tag{3.10}$$

$$p_3(x,y) = (x_b + \frac{b}{2}, 0) \tag{3.11}$$

The normal functions along the three segments and the discontinuity jumps at the three corners are presented in tables 3.3 and 3.4 respectively. Then, replacing these values in equations (3.5), (3.6) and (3.7) the point shear forces at the vertices of each triangular patch and the bending moments along its three lateral edges, shown in plot (a) of figure 3.5, are obtained as [66, 72]:

Table 3.3.: Contour functions for the triangular leaf.

Contour	n_x	n_y	$n_x n_y$	n_x^2	n_y^2
Γ_1	$\frac{b}{\sqrt{b^2+4a^2}}$	$\frac{-2a}{\sqrt{b^2+4a^2}}$	$\frac{-2ab}{b^2+4a^2}$	$\frac{b^2}{b^2+4a^2}$	$\frac{4a^2}{b^2+4a^2}$
Γ_2	$\frac{b}{\sqrt{b^2+4a^2}}$	$\frac{2a}{\sqrt{b^2+4a^2}}$	$\frac{2ab}{b^2+4a^2}$	$\frac{b^2}{b^2+4a^2}$	$\frac{4a^2}{b^2+4a^2}$
Γ_3	-1	0	0	1	0

Table 3.4.: Jump functions for the triangular leaf.

Vertex	$[n_x n_y]$	$[n_x^2]$
p_1	$\frac{2ab}{b^2+4a^2}$	$1 - \frac{b^2}{b^2+4a^2}$
p_2	$\frac{-4ab}{b^2+4a^2}$	0
p_3	$\frac{2ab}{b^2+4a^2}$	$\frac{b^2}{b^2+4a^2} - 1$

$$F_1 = (e_{32} - e_{31}) \frac{2ba}{b^2 + 4a^2} h_s v_c \tag{3.12}$$

$$F_2 = -(e_{32} - e_{31}) \frac{4ba}{b^2 + 4a^2} h_s v_c \tag{3.13}$$

$$M_1 = -\frac{b^2 e_{31} + 4a^2 e_{32}}{b^2 + 4a^2} h_s v_c \tag{3.14}$$

$$M_2 = -e_{31} h_s v_c \tag{3.15}$$

It can be seen that $F_2 = -2F_1$ and that the total transverse point force applied to the panel is equal to zero.

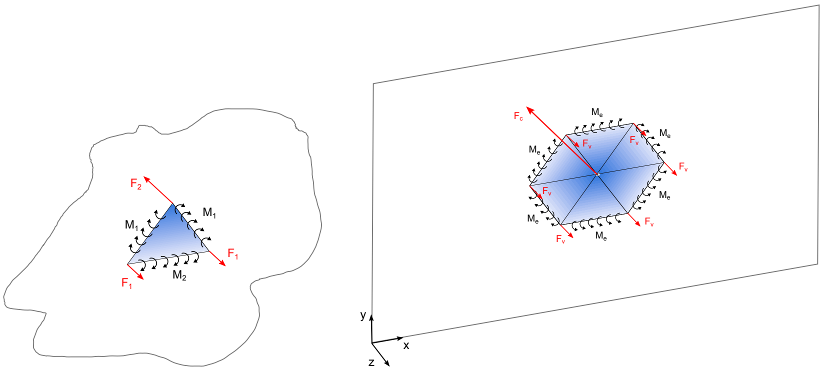

(a) (b)

Figure 3.5.: Point shear forces and bending moments produced by: (a) each triangular leaf and (b) the hexagonal actuator.

Then, the flexural excitation field produced by the hexagonal patch, presented in plot (b) of figure 3.5, is derived by adding the effects of the six triangular leafs, resulting in:

- a shear point force F_c at the centre of the hexagon defined in equation (3.16),
- shear point forces at each of the six vertices of the hexagon described by the equation (3.17), and
- bending moments along the edges of the hexagon defined in equation (3.18).

$$F_c = 6F_2 \tag{3.16}$$

$$F_v = 2F_1 \tag{3.17}$$

$$M_e = M_2 \tag{3.18}$$

It is important to note that this model neglects the bending moments generated along the lateral edges of each triangular leaf; as, ideally, these are cancelled with the ones produced by the contiguous leafs.

As mentioned in the introduction, piezoelectric patch actuators usually have stability drawbacks because of the non collocated actuation effects produced at the edges of the patches. Nevertheless, with this proposed shape, the net transverse point force produced at the centre of the patch would reinforce the collocation characteristic of the actuator-sensor coupling. This would have two important control effects:

1. it would improve the stability properties of the feedback loop, since the spectra of the open loop FRFs have higher magnitude at lower frequencies and lower phase lag at higher frequencies, and
2. it would enhance the active damping effect produced when the feedback loop is closed.

3.2.2 *System set-up*

The block diagram of the control system is shown in figure 3.6, where the mechanical and electrical variables have harmonic time dependence of the form $\text{Re}\{\exp(j\omega t)\}$ where $j = \sqrt{-1}$ and ω is the circular frequency. Also, $F_p(\omega)$ is the primary excitation, $G_{cp}(\omega)$, defined in equation (3.19), is the FRF between the velocity at control position $\dot{w}_c(\omega)$ and the primary force $F_p(\omega)$; $G_{cc(\omega)}$ is the open loop FRF defined in equation (3.20), and G_c is a constant gain.

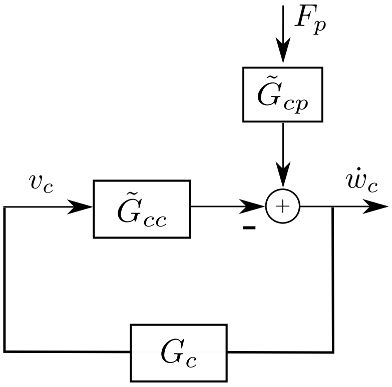

Figure 3.6.: Block diagram of the feedback control system.

$$G_{cp}(\omega) = \frac{\dot{w}_c(\omega)}{F_p(\omega)} \tag{3.19}$$

$$G_{cc}(\omega) = \frac{\dot{w}_c(\omega)}{v_c(\omega)} \tag{3.20}$$

These mobility functions were obtained both by simulation and experimental measurements. For the simulations, $G_{cc}(\omega)$ is defined as follows:

$$G_{cc}(\omega) = G_{cF_c}(\omega) + G_{cF_v}(\omega) + G_{cM_e}(\omega) \tag{3.21}$$

where $G_{cF_c}(\omega)$ and $G_{cF_v}(\omega)$ are the mobility functions between the velocity at control position and the forces $F_c(\omega)$ and $F_v(\omega)$ at the centre and vertices of the patch given by equations (3.16) and (3.17) respectively, and $G_{cM_e}(\omega)$ are the mobility functions between the velocity at control position and the moments M_e along the edge of the hexagon, defined in equation (3.18). These mobility functions were derived using a modal summation approach, and their equations can be found in appendix A.1.

The experimental measurements were conducted with a dSPACE Auto Box DS1103 with a sampling rate set to 48 kHz. The main features of this controller board are

- a CPU with a 1 GHz clock, 32 MB of memory for the application and 96 MB for data storage;
- 4 sample and hold ADC converters connected to 16 multiplexed inputs with a voltage range of ±10 V.
- 8 DAC converters with an output range of ±10 V and ±5 mA.

Figure 3.7 shows the AutoBox in plot (a) and the connector panel in plot (b) with the ADC input channels highlighted by a solid blue rectangle and the DAC output channels by a dashed red rectangle.

Kemo CardMaster 255G filters are used at the sensor input and output of the DAC implementing a low-pass filter with a cut-off frequency set to 25.4 kHz. These filters have internal jumpers to configure AC/DC single ended, differential or IEPE input. Those connected to the sensors have to be set to IEPE. Plot (c) of figure 3.7 shows the front panel of the filter, with the two knobs to select the cut-off frequency, two switches to set the filter gain and the input and output connectors.

The accelerometer sensor is a PCB Piezotronics 352C65 with a natural frequency above 35 kHz, a sensitivity of 10.2 mV/(m/s^2) and a weight of 2 grams. Below its cut-off frequency, the accelerometer produces an output proportional to the base acceleration, which is then integrated in order to obtain the velocity at the centre of the hexagonal patch. As the control loop is closed off-line in Matlab using measured data, the integration of the acceleration signal measured by the sensor is also done in Matlab.

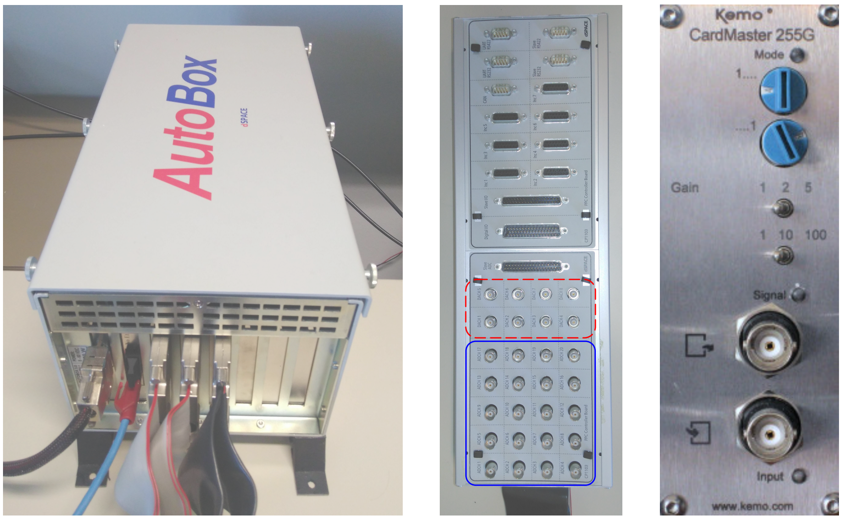

(a) (b) (c)

Figure 3.7.: dSPACE AutoBox with board RT1103 (a) and (b) control panel. (c) Kemo CardMaster 255G front panel.

The primary force $F_p(\omega)$ is produced by a Modal Shop 2007E shaker, whose point of action is located at $x_p = 85$ mm, $y_p = 110$ mm. And to measure it a force sensor PCB Piezotronics 208C01 is used, with a sensitivity of 112.4 mV/N and an upper frequency limit of 36 kHz.

Also, an analogue amplifier with a fixed gain of 1 : 20 was used to drive the patch.

3.2.3 *Open Loop FRF*

The SISO control system is implemented using the hexagonal patch actuator and accelerometer sensor located at the centre of the hexagon. In the simulation an ideal sensor is assumed, with a high fundamental frequency and no mass. Also, the mass and stiffness effect of the patch is not taken into account.

The set-up for the experimental measurement of the open loop FRF is presented in Figure 3.8; where $\dot{w}_c$ is given by the voltage v_{sensor}. As this system is to be applied using analogue devices, the FRF of the Kemo filter 1 was obtained experimentally and then subtracted from the measured data. It is also important to mention that the voltage v_c applied to the patch is measured between the input filter 2 and the fixed gain amplifier and that the integration of the filter 1 output signal v_{output} is done within the dSPACE platform.

Considering the chosen sampling rate and the fact that the Kemo filters cut-off frequency produces a constant roll off of the open loop FRF, it is sufficient

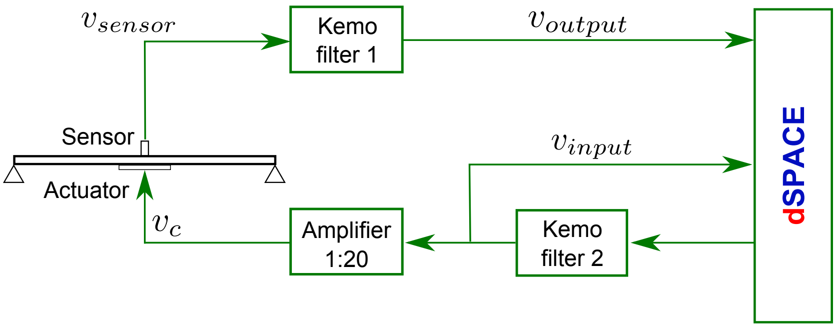

Figure 3.8.: Open loop measurement set-up.

to study the system response up to 20 kHz. As at lower frequencies extra energy is needed to produce an output with a good noise to signal ratio several measurements were taken. Then, 9 measurements were conducted where the patch was excited using a linear cosine sweep from 30 Hz up to 3.8 kHz; and then a final measurement using a broadband white noise signal to obtain the FRF from 3.8 kHz to 20 kHz.

3.2.4 *Control stability analysis*

The stability of the feedback loop is analysed considering the Bode and Nyquist plot of the open loop FRF G_{cc}.

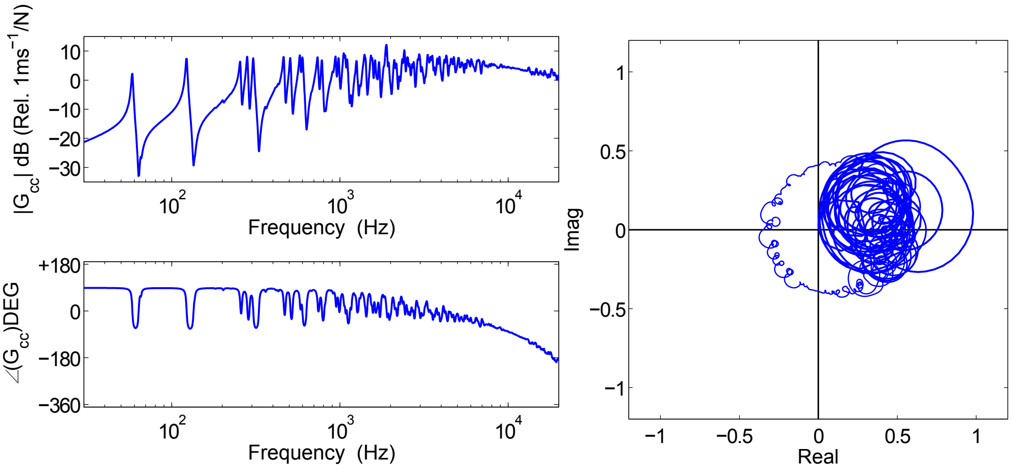

(a) (b)

Figure 3.9.: Simulated open loop FRF (a) Bode and (b) Nyquist plots.

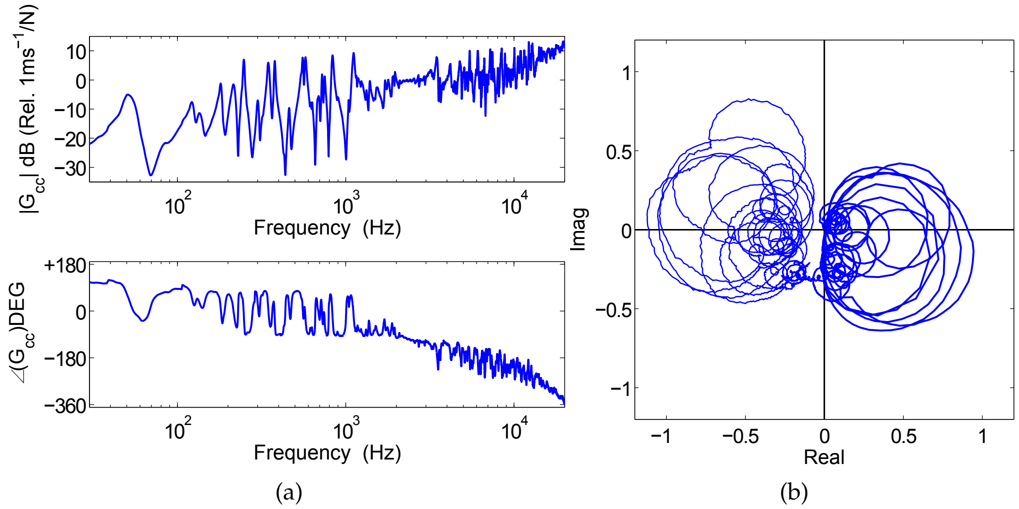

Figure 3.10.: Measured open loop FRF (a) Bode and (b) Nyquist plots.

The simulation results are presented in figure 3.9; plot (b) presents the Bode plot, which shows a response whose amplitude is characterised by a series of well defined resonance peaks and anti-resonance narrow troughs at low frequency, with a magnitude and overlap factor that increase with frequency. The response phase shows a constant lag that starts at about 2 kHz and crosses $-90°$ at around 10 kHz. It can be seen that at this frequency the magnitude plot becomes flat. Then, the first crossover at $-180°$ is at around 17 kHz.

Plot (b) of figure 3.9 presents the Nyquist plot of the simulated system, which shows an entanglement of big circles in the real positive quadrants; above 1 kHz the amplitude of circles is reduced and they slowly start to drift to the real negative quadrant, eventually crossing the real negative axis around 0.32 and returning to the real positive quadrants. The system is stable for a limited range of loop gains.

On the other hand, figure 3.10 shows the Bode and Nyquist plots of the measured open loop FRF. Plot (a) presents the Bode plot, which shows a response characterized by a few damped resonance peaks below 150 Hz; between 200 Hz and 2 kHz it is characterized by a lot of resonance peaks with increasing amplitude, an interesting feature takes place between 2 and 3 kHz: the amplitude does not show any resonance peak nor anti-resonance troughs, this would conveniently allow the implementation of a low-pass filter. Above 3 kHz there is a first resonance peak that could limit the efficiency of the filter, and after that a series of resonance peaks and anti-resonance troughs as the amplitude continues to rise with frequency. From the very beginning of the curve the phase plot shows a delay, which may be introduced by the measuring instruments and that reduces the stability of the loop. The first crossovers at -90° and -180° are around 250 and 3500 Hz.

The Nyquist plot presented in plot (b) of figure 3.10 shows a group of entangled circles in the real positive quadrants, which shift to the real negative quadrants as the frequency and the phase lag increase. The same interesting feature can be seen in the Nyquist plot when the locus crosses the negative imaginary axis, where the entangled circles greatly reduce their diameter as they continue to shift to the negative real quadrants. After this, the circles grow bigger and as they further shift to the upper negative real quadrant they encircle the -1 point in the real negative axis.

The Nyquist plot not only provides a good insight into the system stability, but also into how much vibration reduction the control system is able to achieve. In reference [14] a maximum reduction index R_n for the vibration at the error sensor has been defined in terms of the following simple formula

$$R_n \cong 20log_{10}|1+\delta_n| \tag{3.22}$$

where δ_n is the control ratio defined as

$$\delta_n = -\frac{\mathrm{Re}\{G_{cc}(\omega_n)\}}{\mathrm{Re}\{G_{cc}(\omega_0)\}} \tag{3.23}$$

Equation 3.22 suggests that the amplitude reduction is proportional to the ratio between the real value where the nth resonance circle, which corresponds to the targeted nth resonance node, in the right semi-plane crosses the real axis and the value in the left semi-plane where the locus crosses the real axis.

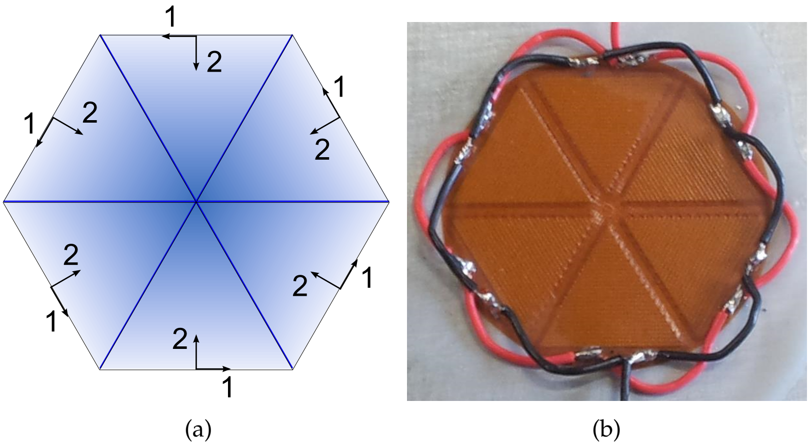

(a) (b)

Figure 3.11.: (a) Ideal and real (b) hexagonal patch.

The differences between the response of the simulated and experimental systems shown in figures 3.9 and 3.10 could be explained in terms of constructive constraints. The hexagonal patch used in the simulation and experimental measurements can be seen respectively in plots (a) and (b) of figure 3.11. A 2 mm gap can be seen in plot (b) between each consecutive leaf of the real hexagonal patch. Recalling figure 3.1, this gap is where the interdigitated electrodes of this MFC patch are placed. As the point force produced at the tip of each leaf is not at the centre of the hexagon and the moments along the edges of each leaf are not properly cancelled this would lead to a slightly different behaviour than the predicted one. Some other factors that were not considered in the model could also modify the response of the patch, such as the effect of the adhesive layer between the panel and the piezoelectric patch, the stiffness of the patch and the mass effect of the patch and the sensor.

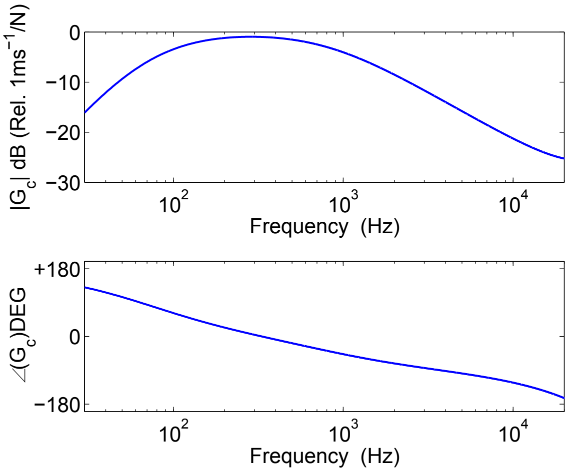

Figure 3.12.: Bode plot of the implemented compensator FRF.

Then, instead of a pure gain g_c, to increase stability, a compensator $G_c(\omega)$ is designed to reduce the incursion of the locus in the negative real quadrants of figure 3.10, reducing in this way the circles in the left hand side quadrants and increasing the reduction index R_n. The compensator, whose FRF is presented in figure 3.12, is composed of a combination of a second order high pass and a first order low pass filter with cut-off frequencies set to 70 and 800 Hz respectively.

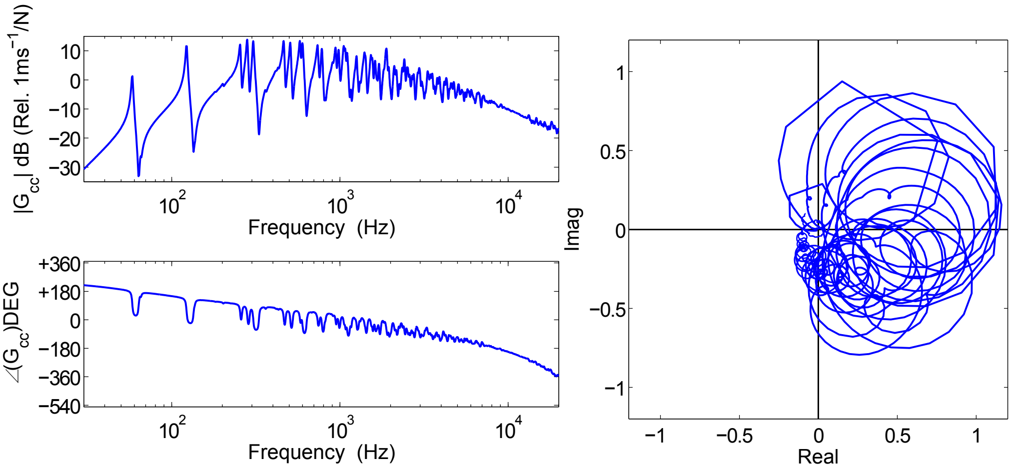

(a) (b)

Figure 3.13.: Simulated (a) Bode and (b) Nyquist plots of the compensated open loop FRF.

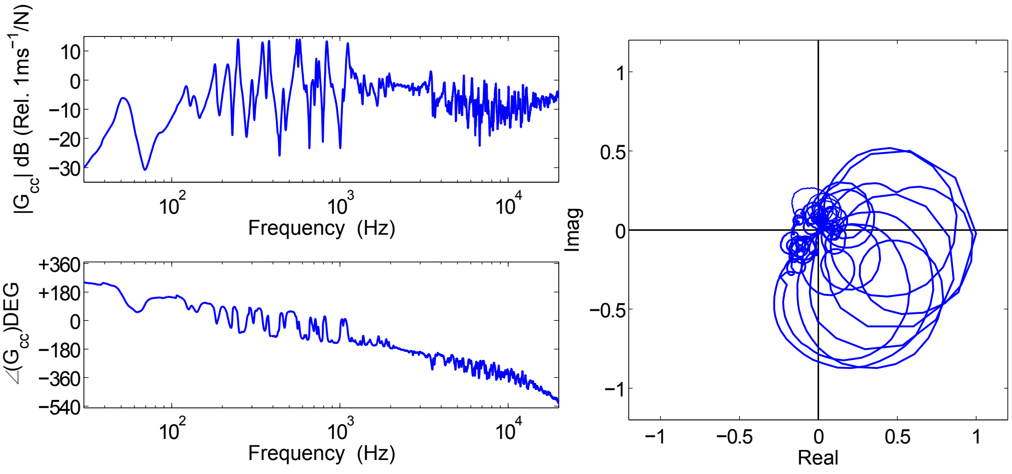

(a) (b)

Figure 3.14.: Measured (a) Bode and (b) Nyquist plots of the compensated open loop FRF.

The compensator was implemented in both the simulated and the experimental set-up, for the latter it was done in Matlab using the previously measured data. Both the simulated and experimental Nyquist plots, presented in plot (b) of figures 3.13 and 3.14, show good improvement after the implementation of the compensator $G_c(\omega)$. Using equation 3.22 yields a maximum reduction of about 20 dB corresponding to the resonance peaks located around 600 Hz for the simulated system, and about 17 dB for the resonance peak at 580 Hz for the experimental set-up.

3.2.5 *Closed loop performance*

The closed loop response of the system can be derived from the block diagram presented in figure 3.6, leading to the following expression

$$\dot{w}_c(\omega) = \frac{G_{cp}(\omega)}{1 + G_{cc}(\omega)G_c(\omega)} F_p(\omega) \tag{3.24}$$

For the simulation, $G_{cp}(\omega)$ is derived using a modal summation approach, the expressions used to calculate it can be found in appendix A.1 together with the ones for the open loop FRF.

Then, in order to simulate off-line the response of the velocity feedback loop based on measured data, the $G_{cp}(\omega)$ FRF was also measured, which is defined in equation 3.19 as the mobility function between the velocity at control position and the primary force.

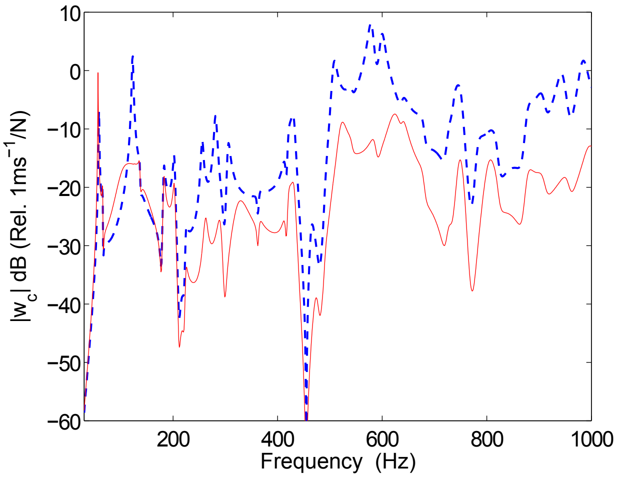

Figure 3.15.: Narrow band spectra of the control velocity per unit force of the shaker with no control (thick dashed blue line) and with active control (thin solid red line) for the simulated SISO system.

Also, the broad band white noise input $F_p(\omega)$ has been coloured using a passband filter to obtain more realistic results. The passband is composed of a second-order high pass filter with a cut-off frequency of 100 Hz and a first order low pass filter with a cut-off frequency of 3.5 kHz.

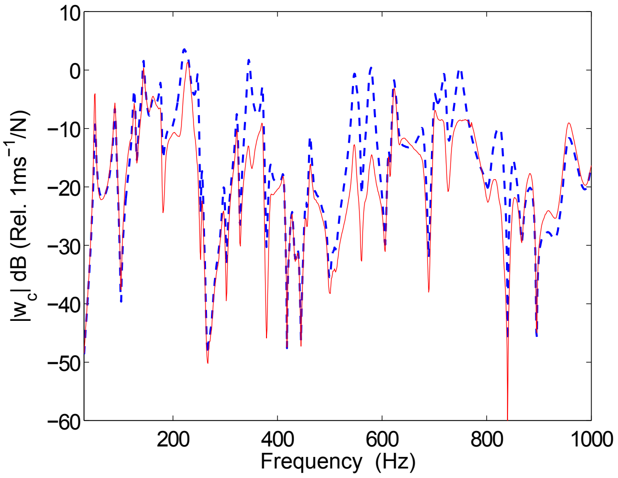

Figure 3.16.: Narrow band spectra of the control velocity per unit force of the shaker with no control (thick dashed blue line) and with active control (thin solid red line) for the experimental SISO system.

The feedback loop is then closed setting the compensator $G_{cc}(\omega)$ with a gain equal to 80% the gain margin for both the simulation and the off-line experiment. This gain value showed a good compromise between the reduction that can be obtained for the response magnitude and the spillover effect.

The plots of the simulated closed loop FRF are presented in figure 3.15, where the thick dashed blue line represents the uncontrolled system and the thin solid red line the system with the active control unit. Some spillover is noticed in the first resonance peak, nevertheless the simulation results show a good reduction in almost all the targeted frequency band; achieving a maximum reduction of 20 dB for the resonance peak at 580 Hz.

On the other hand, the off-line experimental closed loop response is presented in figure 3.16 where the same colour and types of lines is used to identify the controlled and uncontrolled system. As expected, at low frequency below 100 Hz the controller has almost no effect on the response. However, as frequency increases up to 1 kHz most of the resonance peaks are reduced between 3 and 17 dB, with an average reduction of 3 dB in this frequency range. Some spillover can be seen in the first resonance peak at 50 Hz, and very little at 880, 920 and 960 Hz.

3.3 MIMO FEEDBACK SYSTEM

In this section a system with five decentralised active control units is analysed. The experimental system is presented in figure 3.17, in which five velocity feedback loops are implemented using five hexagonal actuators with accelerometers at their centres, as defined in table 3.5.

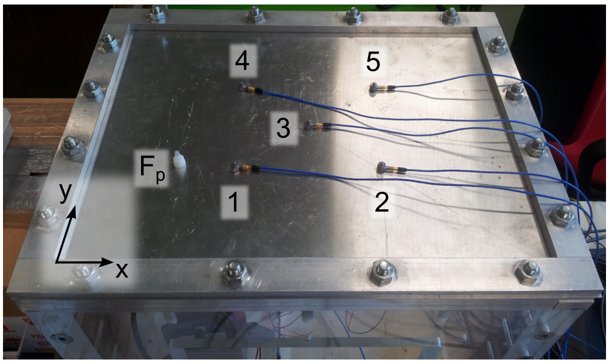

(a) Top view from outside of the perspex box.

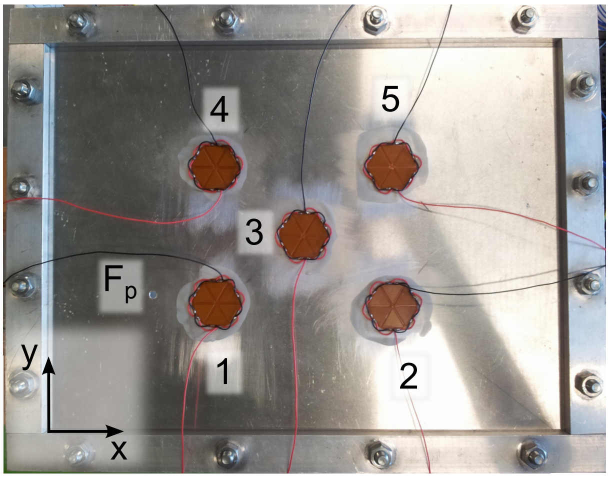

(b) Bottom view from inside of the perspex box.

Figure 3.17.: Perspex box showing (a) the panel with the five accelerometers and the excitation force action point and (b) the five hexagonal patches.

Table 3.5.: Coordinates of the centre of each hexagonal actuator.

Actuator	1	2	3	4	5
y [mm]	102	101	157	213	214
x [mm]	137	280	208	137	280

Plot (a) of figure 3.17 shows a top view from outside the perspex box where the five accelerometers can be seen, and also the primary force application point together with the coordinate reference system. Plot (b) on the other hand, shows a bottom view from the inside of the perspex box where the five piezoelectric actuators can be seen.

For this MIMO configuration, the vector with the closed loop responses of the five control velocities is given by [73]

$$\dot{\mathbf{w}}_c(\omega) = [\mathbf{I} + \mathbf{G}_{cc}(\omega)\mathbf{G}_c(\omega)]^{-1}\mathbf{G}_{cp}(\omega)F_p(\omega) \tag{3.25}$$

where $\dot{\mathbf{w}}_c(\omega)$ is a 5×1 vector containing the complex velocity signals from the error sensors, $\mathbf{I}$ is a 5×5 identity matrix, $\mathbf{G}_{cc}(\omega)$ is a 5×5 fully populated matrix with the transfer functions between the control voltage v_c driving each actuator and the velocity at each control position (refer to appendix A.2 for detailed equations), $\mathbf{G}_c(\omega)$ is a diagonal matrix with the compensator and control gain of each loop, $\mathbf{G}_{cp}(\omega)$ is a 5×1 vector with the five transfer functions between each velocity at control positions and the primary force $F_p(\omega)$.

3.3.1 *Control stability analysis*

The stability of the system is assessed using the generalized Nyquist criterion [7], which establishes that the system is stable if the locus of $\det[\mathbf{I} + \mathbf{G}_{cc}(\omega)\mathbf{G}_c(\omega)] = 0$ does not encircle the instability point $(0, j0)$ as the frequency varies from 30 Hz to 20 kHz. As the determinant of a matrix is the product of its eigenvalues, the stability analysis of the system can be assessed through the polar plots of the five eigenvalues of $\mathbf{I} + \mathbf{G}_{cc}(\omega)\mathbf{G}_c(\omega)$. In this case the five loci should not encircle the instability point $(-1, j0)$.

The loci of the simulated system, left-hand side plots presented in figure 3.18, exhibit a quite convenient shape for stability with almost all the circles in the real positive quadrants and few incursions into the real negative ones. The highest eigenvalue defines the gain margin, and the maximum reduction that could be achieved is around 27 dB.

Considering the experimental results, the right-hand side plots in figure 3.18 show that the loci of the highest eigenvalue also has a very convenient shape for stability, quite similar to the simulated one but with smaller incursions into the real negative quadrants. Nevertheless, it can be seen that the second eigenvalue has a big circle in the left quadrants; defining a lower gain margin and a maximum reduction index of 15 dB. The stability of the experimental MIMO system is lower compared to the one of the SISO due to interactions between the loops, represented by the transfer functions $\mathbf{G}_{cc}(i, j)$ when $i \neq j$. It is noted that the compensators $\mathbf{G}_c(\omega)$ are the same used for the SISO system, and the loop gain was set considering the most critical loci, i.e. the second one. Then, the same compensator and gain was applied to the five control loops.

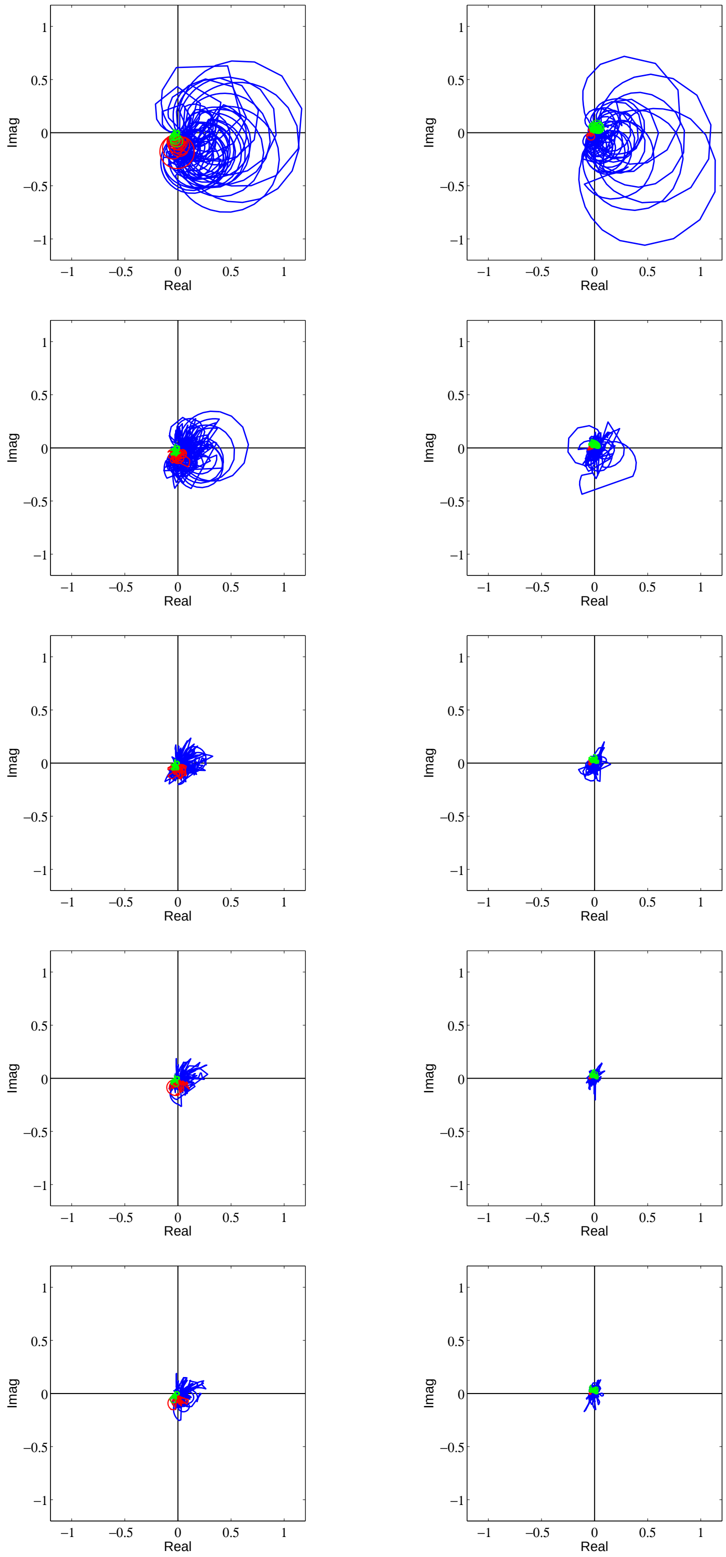

Figure 3.18.: Loci of the five eigenvalues of the simulated (left-hand side plots) and measured (right-hand side plots) $\mathbf{G}_{cc}(\omega)$ matrix between 30 Hz and 20 kHz.

3.3.2 *Closed loop performance*

The overall performance of the system is evaluated using equation when applying a loop gain equal to 80% the gain margin.

$$\dot{\mathbf{w}}_c^{avg}(\omega) = \sum |\dot{\mathbf{w}}_c(\omega)|^2 = \dot{\mathbf{w}}_c^H(\omega)\dot{\mathbf{w}}_c(\omega) \tag{3.26}$$

where the superscript ^{H} is used to indicate the Hermitian operator.

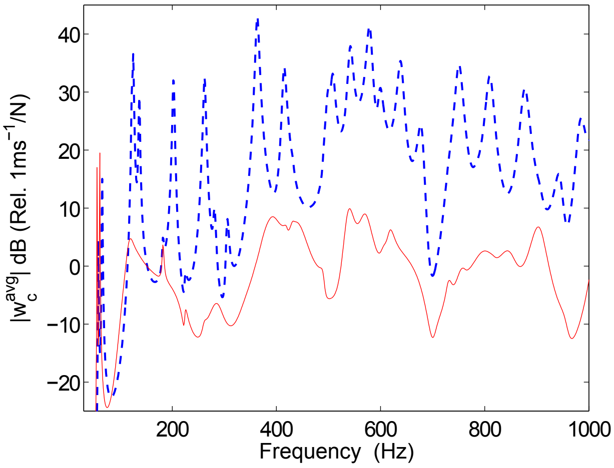

Figure 3.19.: Narrow band spectra of the control velocity per unit force of the shaker with no control (thick dashed blue line) and with active control (thin solid red line) for the simulated MIMO system.

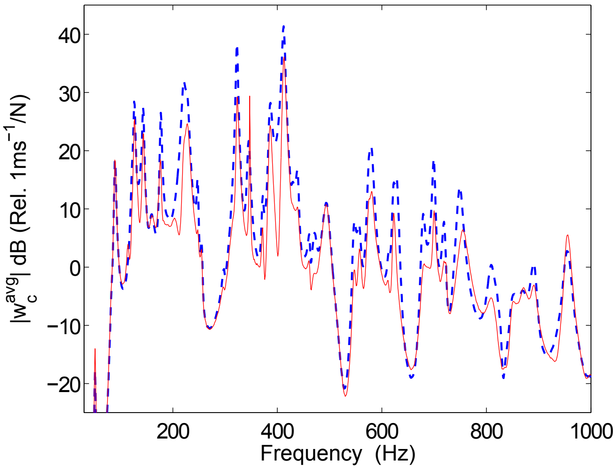

Figure 3.20.: Narrow band spectra of the control velocity per unit force of the shaker with no control (thick dashed blue line) and with active control (thin solid red line) for the experimental MIMO system.

The results of the simulated system presented in figure 3.19 are quite promising, showing high reductions in all the considered band, except for a little spillover at the first resonance peak.

Regarding the off-line control using measured FRFs, figure 3.20 shows that the amplitudes of most of the resonance peaks between 100 Hz and 1 kHz are reduced between 3 and 9 dB. The controller has no effect below 100 Hz and produces very little spillover at the resonance peak at 950 Hz.

3.4 CHAPTER CONCLUDING REMARKS

This chapter presented simulation and experimental results of the active control effects of SISO and MIMO velocity feedback loops on a thin panel using hexagonal MFC actuators.

The theoretical work predicted for the SISO set-up good reductions in most of the considered frequency band with a maximum reduction of around 20 dB. While for the MIMO configuration, impressive reductions were predicted in all the frequency of interest, except below 100 Hz.

On the other hand, the off-line experimental results showed good agreement with the simulated SISO system; with good reductions in most of the resonance peaks. The differences between simulation and experimental results are higher when implementing off-line the five decentralised actuators; however, the system is capable of reducing the response magnitude at several resonance peaks. This performance difference is explained by the existence of a big circle in the real left quadrant of the second loci, which drastically lowers the gain margin and the maximum reduction index of the experimental system.

One reason for the discrepancies between simulation and experimental results could be the gap between consecutive triangular leafs of the hexagon. Due to this gap the moments produced at the edges of the leafs are not properly cancelled and the point forces at the tip of each leaf are not acting at the centre of the hexagon.

Considering these promising results, an improvement in the overall performance is expected when reducing the gap between consecutive triangular leafs of the hexagon.

4

SHUNTED PIEZOELECTRIC TRANSDUCERS FOR VIBRATION CONTROL

This chapter studies the flexural vibration control effects produced on a two-dimensional thin structure by a shunted piezoelectric vibration absorber. In particular, it shows how the high modal overlap factor and the electromechanical inherent properties of piezoelectric patches can influence the tuning of the electrical shunt and therefore the performance of the vibration control system produced at the target frequencies.

A parametric study is also presented in which general guidelines for the dimensioning of the piezoelectric patch vibration absorber are provided in order to maximise the vibration control performance.

Contents

4.1 INTRODUCTION

The study presented here considers a plate equipped with a pair of collocated piezoelectric transducers connected to a shunt, which is tuned in such a way as to absorb vibration energy near a resonance frequency of the hosting structure. In their work published in 1991, Hagood and von Flotow [21] presented two methods to find the optimum values for an RL shunt: one based on the pole placement control theory and the other based on the fixed-point formulation developed by Den Hartog [22] for mechanical TVAs. Approximated and exact expressions to calculate the optimal inductance and resistance of the RL shunt can also be found in recent works [74–76]. However, they refer to simplified systems that consider only one flexural natural mode of the hosting structure; and, in general, the flexural response spectrum of distributed structures subject to broad band disturbances is characterised by multiple resonance peaks produced by the overlap of the second order responses of the structure natural modes [70].

The distribution of the resonance peaks on the frequency axis depends on the type of structure (beam, plate, shell, etc.) and on the type of wave (flexural, extensional, etc.) and it is defined by the modal density factor $n(\omega)$ [70, 77, 78], which gives the average number of natural frequencies per unit frequency where ω is the circular frequency in rad/s. Furthermore, the number of modal responses that contribute to the overall response of the structure at a given frequency is proportional to frequency, to the modal damping ratio and to the modal density factor. This effect is usually quantified with the so called modal overlap factor $M(\omega) = 2\omega\xi n(\omega)$ [70, 77, 78]. In thin two-dimensional structures, flexural vibrations are characterised by modal overlap factors that rise rapidly with frequency. Then, the flexural response at each frequency of shells and plates is influenced by multiple modes.

The system proposed in this work is composed of a pair of collocated thin rectangular piezoelectric transducers bonded on opposite sides of the panel, forming in this way a symmetric laminate around the mid-plane of the panel. The transducers are connected in a counter-phase parallel architecture. The shunt is composed by a parallel RL circuit which together with the inherent capacitance of the transducers produce a resonating electrical circuit that couples with the flexural vibration of the panel, acting as a vibration absorber [21, 22, 79]. An ideal negative capacitance, which compensates the inherent one of the transducers [24–37, 80], is then also considered in the parallel circuit. An analytical fully coupled model, which includes the passive mechanical and electro-mechanical effects of the piezoelectric transducers, is used to derive the flexural response of the plate with the pair of piezoelectric patches.

This study highlights how the shunt tuning is affected by the multi-modal response of distributed two-dimensional structures and by the inherent electrical and passive mechanical effects of the piezoelectric transducers. A parametric study is also presented, which provides general guidelines on how the area and thickness of the transducers affect the tuning and performance of the piezoelectric vibration absorber system.

4.2 MODELLING OF SHUNTED PIEZOELECTRIC TRANSDUCERS BONDED ON A THIN PLATE

The system considered in this study is presented in figure 4.1, it is composed of a simply supported rectangular thin panel with a pair of collocated, rectangular, thin, piezoelectric transducers bonded slightly offset from the centre of the aluminium plate. The piezoelectric patches have the same aspect ratio as the plate and lateral edges oriented parallel to the edges of the plate. Both patches have the same dimensions and are made of the same material, which means they have the same elastic and piezoelectric properties. The patches are assumed perfectly bonded on the plate, one on the bottom surface and the other on the top surface. In this way, they form a symmetric laminate around the plate mid-surface. Then, as shown in figure 4.1 the principal reference system is located on the bottom left corner of the panel with x and y axes laid on the plate mid-surface parallel to the edges of plate. A double notation (x, y, z) and $(1, 2, 3)$ is used for the principal axes to simplify the mathematical formulation. The piezoelectric transducers are polarised in transverse direction, indicated by

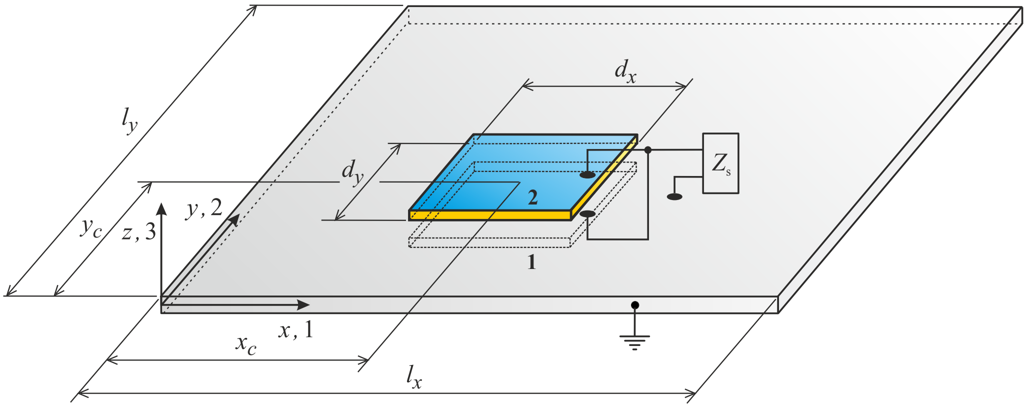

Figure 4.1.: Plate with a pair of piezoelectric transducers.

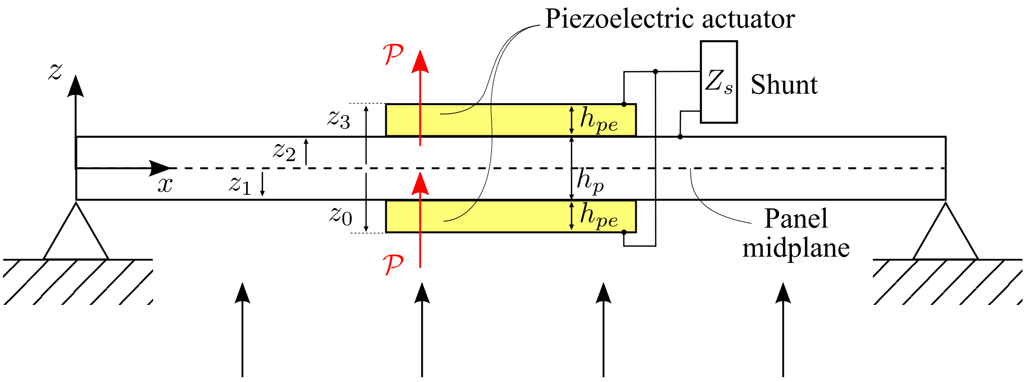

Figure 4.2.: Cross section of the plate with the pair of shunted piezoelectric transducers.

the red arrow in figure 4.2. As they are bonded on opposite surfaces of the plate, they undergo opposite form of normal strains in x and y directions when the plate bends, i.e. extensional against compressional strains. Then, the pair of transducers are connected in a counter-phase parallel architecture as to offer the same electromechanical loads to flexural vibrations despite the above mentioned fact that they are bonded on opposite surfaces of the panel. This arrangement of two patches is then connected to an electrical shunt circuit, devised to reduce the flexural vibration contribution due to one flexural mode of the plate. The shunt, as shown in figure 4.3 is composed of an inductor and a resistor in parallel, which together with the inherent capacitance of the piezoelectric transducers form an RLC parallel circuit. It is possible to maximise the absorption of the electrical energy generated by the extensional and compressional normal strains of the two piezoelectric patches due to the flexural vibration of the plate by properly tuning the inductance and resistance of the shunt [21, 22, 79].

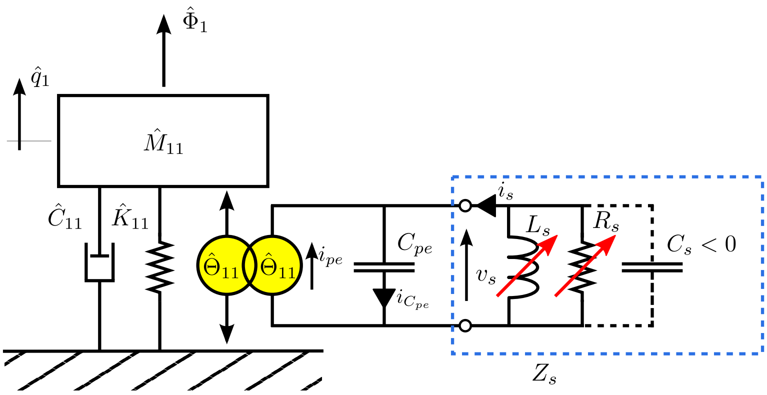

Figure 4.3.: Lumped parameters model of the system considering only its first natural mode.

Piezoelectric transducers are, generally speaking, characterised by a relatively large inherent capacitance, which limit the effectiveness of the shunt. Then, the possibility of adding a negative capacitance to the shunt to compensate that of the patches [25]. To implement this negative capacitance effect active electrical circuits using operational amplifiers could be used; however, this introduces a number of issues [24–37, 80] that should be taken into account, e.g. the system stability. For simplicity and as depicted in figure 4.3 an idealised capacitor characterised by negative capacitance is considered in the shunt.

A uniform distribution of uncorrelated, stochastic, transverse forces resembling a rain on the roof excitation [12] is used to excite the plate. The steady state response of the plate is expressed in terms of the power spectral density (PSD) of the total flexural kinetic energy [12].

Table 4.1.: Dimensions and physical properties of the plate.

Parameter	Value	Units
Thickness	$h_p = 1$	mm
Length	$l_x = 414$	mm
Width	$l_y = 314$	mm
Density	$\rho_p = 2700$	kg/m^3
Young's Modulus	$Y_p = 70 \times 10^9$	N/m^2
Poisson's ratio	$\nu_p = 0.33$	—
Modal damping ratio	$\xi_p = 0.02$	—

The principal reference system depicted in figure 4.1 is used to define the constitutive relations for both the panel and the piezoelectric patches. The plate is made of aluminium isotropic material and the transducers of a piezoceramic material polarized in transverse z-direction and isotropic in the x–y plane. Both materials are assumed homogeneous and linearly elastic. The geometry and mechanical properties of the panel are presented in table 4.1 while the geometry and electromechanical properties of the patches are provided in table 4.2.

The plate and the two piezoelectric transducers form a symmetric laminate around the mid-surface of the plate. In this case the in-plane extensional and shear vibrations [77] are uncoupled from the out-of-plane flexural vibrations of the panel [81]. Then, considering that the study is focused on the flexural vibrations of the plate produced by out-of-plane loads in a low audio frequency range up to 1 kHz, the model for the out-of-plane response of the plate with the pair of shunted piezoelectric transducers is simply derived.

Table 4.2.: Dimensions and physical properties of the piezoelectric patches.

Parameter	Value	Units
Thickness	$h_{pe} = 0.5$	mm
Width	$d_x = 82.8$	mm
Length	$d_y = 62.8$	mm
Centre position	$x_c = \frac{13}{28} l_x$	mm
	$y_c = \frac{15}{28} l_y$	mm
Density	$\rho_{pe} = 7600$	kg/m^3
Young's Modulus	$Y_{pe} = 50 \times 10^9$	N/m^2
Poisson's ratio	$\nu_{pe} = 0.35$	—
Permittivity	$\varepsilon_{33}^T = 29.2 \times 10^{-9}$	F/m
Inherent capacitance	$C_{pe} = 267.9 \times 10^{-9}$	F
Strain/charge constants	$d_{31} = -150 \times 10^{-12}$	m/V
	$d_{32} = -150 \times 10^{-12}$	m/V
	$d_{36} \approx 0$	m/V

The study considers that the piezoelectric patches are perfectly bonded to the panel, i.e. the layers of epoxy adhesive are very thin and stiff compared to the plate and patches; in this case the bending strains are assumed continuous at the interface between the panel and the patches [82–85]. Also, the considered thicknesses of the plate and piezoelectric patches are at least 10 times smaller than the surface dimensions of the plate and of the patches.

Therefore, the out-of-plane flexural vibrations of the plate with the shunted transducers are derived with the classical laminated plate theory (CLPT) [81]. The CLPT assumes linearly varying laws across the whole panel and piezoelectric transducers laminate with null values at the plate mid-surface for the normal strains in x and y directions. Then, according to Hooke's stress-strain law for linearly elastic materials, also the normal stresses in x and y directions should vary linearly across the laminate; however, as the material properties of the plate and of the piezoelectric transducers are not the same, the normal stresses in x and y directions are characterised by discontinuity and change in slope at the interfaces between the plate and the piezoelectric patches [86, 87]. In fact, these discontinuities are emphasised by the additional normal stresses in x and y directions produced by the electrical activation of the piezoelectric patches, which are in opposite direction than those produced by the restoring strain of the piezoelectric material [85, 87]. However, the equilibrium condition at the free edges of the transducers enforces the in-plane normal stress components in x and y directions to be zero, which is in conflict with the linearly varying hypothesis mentioned above [81]. Nevertheless, Liang and Rogers [82] showed that the in-plane normal stress field in the transducers is actually unaffected by the free edges except approximately four patch thicknesses from the edges. Then, as the considered rectangular piezoelectric transducers have a large aspect ratio (i.e. lateral dimensions vs thickness), the linear stress distribution can be assumed [85], which generates a case a pure bending in the laminate. Furthermore, Crawley and de Luis [83] showed that for perfectly bonded patches the laminate generates bending moments than can be localised along the boundaries of the piezoelectric transducers.

On the other hand, if the piezoelectric patches material properties were not isotropic in the plane and the material principal axes were not parallel to the edges of the patches, twisting moments would also be generated along the edges of the patches together with the bending moments mentioned before. These twisting moments would produce transverse point forces acting at each corner of the patches, but whose overall effect is necessarily zero, as expected for strain actuators [71, 88–91].

4.2.1 *Stress/strain relations of the plate and patches*

The out-of-plane flexural vibration of the plate with the shunted piezoelectric patches is derived considering the CLPT, which for the system at hand, assumes [57, 81]:

1. the thicknesses of the plate and piezoelectric patches are small compared to the surface dimensions of the plate and piezoelectric patches (ratio thickness vs lateral dimensions < 0.1);
2. the displacements of the plate mid-surface are much smaller than unity such that their squares and products are negligible;
3. the out-of-plane normal stress is small compared to the in-plane normal stresses;
4. transverse normals perpendicular to the laminate mid-surface remain straight after deformation, they do not undergo elongation and remain perpendicular to the mid-surface after deformation.

The fourth hypothesis, known as Kirchhoff hypothesis, leads to the following linear relationships for the in-plane $U(x,y,z,t)$ and $V(x,y,z,t)$ and the out-of-plane $W(x,y,z,t)$ displacements in the plate and piezoelectric patches [81]:

$$U(x,y,z,t) = u(x,y,t) - zw_{,x}(x,y,t) \tag{4.1}$$

$$V(x,y,z,t) = v(x,y,t) - zw_{,y}(x,y,t) \tag{4.2}$$

$$W(x,y,z,t) = w(x,y,t) \tag{4.3}$$

where $u(x,y,t)$ and $v(x,y,t)$ are the in-plane displacements, $w(x,y,t)$ is the out-of-plane displacement of the panel mid-surface and $w_{,x}$ and $w_{,y}$ are the rotations of the normal to the mid-surface about the y and x axe respectively where the subscript "$_,$" is used to indicate the spatial derivative. The Kirchoff hypothesis also leads to a plane strain state [46, 47, 57, 81], which means that S_3, S_4 and S_5 are zero. The condition of zero shear strains S_4 and S_5 for isotropic or orthotropic materials implies that also the shear stresses T_4 and T_5 are zero. Then, considering the third hypothesis, which assumes that T_3 is zero, there is also a plane stress state, which is normally used to define the material stress/strain relations for thin laminates [46, 47, 57, 81]. Then, the constitutive expressions for the plate and piezoelectric patches are expressed as:

$$\mathbf{T} = \begin{bmatrix} T_1 \\ T_2 \\ T_6 \end{bmatrix} \quad (4.4a) \qquad \mathbf{S} = \begin{bmatrix} S_1 \\ S_2 \\ S_6 \end{bmatrix} \quad (4.4b)$$

The second hypothesis leads to linear strain-displacement relations [46, 47, 57, 81], such that:

$$S_1 = U_{,x} \tag{4.5}$$

$$S_2 = V_{,y} \tag{4.6}$$

$$S_6 = U_{,y} + V_{,x} \tag{4.7}$$

Substituting the displacements given in equations (4.1)-(4.3) into these expressions yields the following strains relations with respect to the displacements and curvatures of the plate mid-surface:

$$S_1 = u_{,x}(x,y) - zw_{,xx}(x,y) \tag{4.8}$$

$$S_2 = v_{,y}(x,y) - zw_{,yy}(x,y) \tag{4.9}$$

$$S_6 = u_{,y}(x,y) + v_{,x}(x,y) - 2zw_{,xy}(x,y) \tag{4.10}$$

Finally, considering only the transverse displacement of the plate mid-surface (i.e. neglecting $u_{,x}(x,y)$, $v_{,y}(x,y)$, $u_{,y}(x,y)$ and $v_{,x}(x,y)$) the plate and piezoelectric transducers strain vector can be expressed as:

$$\mathbf{S} = z\mathbf{K} \tag{4.11}$$

where **K** the vector with the curvatures due to bending deformation of the plate defined as

$$\mathbf{K} = \begin{bmatrix} -w_{,xx} \\ -w_{,yy} \\ -2w_{,xy} \end{bmatrix} \tag{4.12}$$

where for simplicity the dependency on the x and y variables has been omitted.

The electric field and electric displacement vectors are presented in equations (4.13a) and (4.13b). The electric field, generated by the electric potential difference at the two electrodes is aligned with the polarization vector along direction 3; and the same happens with the polarization vector.

$$\mathbf{E} = \begin{bmatrix} E_1 \\ E_2 \\ E_3 \end{bmatrix} = \begin{bmatrix} 0 \\ 0 \\ E_3 \end{bmatrix} \tag{4.13a}$$

$$\mathbf{D} = \begin{bmatrix} D_1 \\ D_2 \\ D_3 \end{bmatrix} = \begin{bmatrix} 0 \\ 0 \\ D_3 \end{bmatrix} \tag{4.13b}$$

As both vectors have only one component, the following notation is used $E_{pe} = E_3$ and $D_{pe} = D_3$ instead of the vectorial one. Also, as the transducers have a constant thickness and their piezoelectric material is homogeneous, the electric field can be assumed constant as for small thicknesses fringe effects are negligible [92]. Then, the following electric field-electric potential relation is assumed:

$$E_{pe} = \frac{v_{pe}}{h_{pe}} \tag{4.14}$$

where v_{pe} is the voltage difference across the electrodes of the two piezoelectric transducers connected in parallel. On the other hand, also the electric displacement generated by the piezoelectric material produces a total electric charge on the electrodes of the patches, given by:

$$Q_{pe} = \int_{A_{pe,i}} D_{pe} A_{pe,i} \tag{4.15}$$

Then, the following matrix form [2, 92] can be used to express the constitutive equations for the plate material as:

$$\mathbf{T} = \mathbf{c}_p \mathbf{S} \tag{4.16}$$

and for the piezoelectric material as:

$$\begin{bmatrix} D_{pe} \\ \mathbf{T} \end{bmatrix} = \begin{bmatrix} \varepsilon_{pe}^{\mathbf{S}} & \mathbf{e}_{pe}^{T} \\ -\mathbf{e}_{pe} & \mathbf{c}_{pe}^{E} \end{bmatrix} \begin{bmatrix} E_{pe} \\ \mathbf{S} \end{bmatrix} \tag{4.17}$$

where $\varepsilon_{pe}^{\mathbf{S}} = \varepsilon_{33}^{\mathbf{S}}$ is the piezoelectric material permittivity in transverse direction under constant strain ($\mathbf{S} = 0$), the vector $\mathbf{e}_{pe}$ is given by the piezoelectric stress/charge constants

$$\mathbf{e}_{pe} = \begin{bmatrix} e_{31} \\ e_{32} \\ 0 \end{bmatrix} \tag{4.18}$$

and the matrices $\mathbf{c}_p$ and $\mathbf{c}_{pe}^{E}$ give the elastic constants for the plate and piezoelectric patches and are defined as

$$\mathbf{c}_p = \begin{bmatrix} \frac{Y_p}{1-\nu_p^2} & \frac{\nu_p Y_p}{1-\nu_p^2} & 0 \\ \frac{\nu_p Y_p}{1-\nu_p^2} & \frac{Y_p}{1-\nu_p^2} & 0 \\ 0 & 0 & \frac{Y_p}{2(1+\nu_p)} \end{bmatrix} \tag{4.19a}$$

$$\mathbf{c}_{pe}^{E} = \begin{bmatrix} \frac{Y_{pe}^{\mathbf{E}}}{1-\nu_{pe}^{\mathbf{E}2}} & \frac{\nu_{pe}^{\mathbf{E}} Y_{pe}^{\mathbf{E}}}{1-\nu_{pe}^{\mathbf{E}2}} & 0 \\ \frac{\nu_{pe}^{\mathbf{E}} Y_{pe}^{\mathbf{E}}}{1-\nu_{pe}^{\mathbf{E}2}} & \frac{Y_{pe}^{\mathbf{E}}}{1-\nu_{pe}^{\mathbf{E}2}} & 0 \\ 0 & 0 & \frac{Y_{pe}^{\mathbf{E}}}{2(1+\nu_{pe}^{\mathbf{E}})} \end{bmatrix} \tag{4.19b}$$

where Y_p and ν_p are the Young's modulus (or elastic modulus) and Poisson ratio of the plate and $Y_{pe}^{\mathbf{E}}$ and $\nu_{pe}^{\mathbf{E}}$ correspond to the piezo, measured under constant field intensity ($\mathbf{E} = 0$).

The parameters e_{31}, e_{32} and $\varepsilon_{pe}^{\mathbf{S}}$ are not available in commercial datasheets, so they are usually derived using an alternative form of the constitutive equations of the piezoelectric material:

$$\begin{bmatrix} D_{pe} \\ \mathbf{S} \end{bmatrix} = \begin{bmatrix} \varepsilon_{pe}^{\mathbf{T}} & \mathbf{d}_{pe}^{T} \\ \mathbf{d}_{pe} & \mathbf{s}_{pe}^{E} \end{bmatrix} \begin{bmatrix} E_{pe} \\ \mathbf{T} \end{bmatrix} \tag{4.20}$$

where $\varepsilon_{pe}^{\mathbf{T}}$ is the piezoelectric material permittivity in transverse direction under constant stress ($\mathbf{T} = 0$), the vector $\mathbf{d}_{pe}$ is given by the piezoelectric strain/charge constants provided in table 4.2

$$\mathbf{d}_{pe} = \begin{bmatrix} d_{31} \\ d_{32} \\ 0 \end{bmatrix} \tag{4.21}$$

and the matrix $\mathbf{s}_{pe}^{E}$ gives the compliance constants for the piezoelectric patches:

$$\mathbf{s}_{pe}^{E} = \begin{bmatrix} \frac{1}{Y_{pe}^{\mathbf{E}}} & -\frac{\nu_{pe}^{\mathbf{E}}}{Y_{pe}^{\mathbf{E}}} & 0 \\ -\frac{\nu_{pe}^{\mathbf{E}}}{Y_{pe}^{\mathbf{E}}} & \frac{1}{Y_{pe}^{\mathbf{E}}} & 0 \\ 0 & 0 & \frac{2(1+\nu_{pe}^{\mathbf{E}})}{Y_{pe}^{\mathbf{E}}} \end{bmatrix} \tag{4.22}$$

The values for the piezoelectric material permittivity in transverse direction under constant strain $\varepsilon_{pe}^{\mathbf{S}}$ and for the vector $\mathbf{e}_{pe}$ are obtained by setting the stress $\mathbf{T}$ equal to zero in equations (4.17) and (4.20), which gives the following set of four equations:

$$D_{pe} = \varepsilon_{pe}^{\mathbf{S}} E_{pe} + \mathbf{e}_{pe}^{T} \mathbf{S} \tag{4.23}$$

$$0 = -\mathbf{e}_{pe} E_{pe} + \mathbf{c}_{pe}^{E} \mathbf{S} \tag{4.24}$$

$$D_{pe} = \varepsilon_{pe}^{\mathbf{T}} E_{pe} \tag{4.25}$$

$$\mathbf{S} = \mathbf{d}_{pe} E_{pe} \tag{4.26}$$

Substituting equation 4.26 in equation 4.24 gives

$$\mathbf{e}_{pe} = \mathbf{c}_{pe}^{E} \mathbf{d}_{pe} \tag{4.27}$$

Then, substituting equations 4.25, 4.26 and 4.27 in equation 4.23 yields

$$\varepsilon_{pe}^{\mathbf{S}} = \varepsilon_{pe}^{\mathbf{T}} (1 - k^2) \tag{4.28}$$

where k is called the electromechanical coupling coefficient [2, 44] of the piezoelectric transducer and is defined as follows

$$k^2 = \frac{\mathbf{e}_{pe}^{T} \mathbf{c}_{pe}^{E} \mathbf{d}_{pe}}{\varepsilon_{pe}^{\mathbf{T}}} \tag{4.29}$$

4.2.2 *Variational formulation using the generalised Hamilton's principle*

The equations of motion for the flexural vibration of the plate with the shunted piezoelectric transducers are derived using the generalised form of Hamilton's principle for electromechanical systems considering the variational indicator $V.I.$ for displacement and flux linkage variables [2, 92, 93]:

$$\int_{t_1}^{t_2} [\delta L + \delta W_{nc}]\, dt = 0 \tag{4.30}$$

where $\delta(\dots)$ is the variation operator, W_{nc} is the work done by non conservative forces and L is the Lagrangian given by [2]:

$$L = T^* - V + W_e^* \tag{4.31}$$

where T^*,V and W_e^* represent respectively the kinetic coenergy, the elastic potential energy and the electrical coenergy for the flexural vibrations of the plate with the patches [2, 93]. These three variables are given by [2, 92]:

$$T^* = \frac{1}{2}\int_{V_p} \rho_p \dot{w}^2 \,\mathrm{d}V_p + \sum_{i=1,2} \frac{1}{2}\int_{V_{pe,i}} \rho_{pe} \dot{w}^2 \,\mathrm{d}V_{pe,i} \tag{4.32}$$

$$V = \frac{1}{2}\int_{V_p} \mathbf{S}^T\mathbf{T} \,\mathrm{d}V_p + \sum_{i=1,2} \frac{1}{2}\int_{V_{pe,i}} \mathbf{S}^T\mathbf{T} \,\mathrm{d}V_{pe,i} \tag{4.33}$$

$$W_e^* = \sum_{i=1,2} \frac{1}{2}\int_{V_{pe,i}} E_{pe}D_{pe} \,\mathrm{d}V_{pe,i} \tag{4.34}$$

where the sub-index i is used to identify the two piezoelectric transducers. Substituting equations (4.16) and (4.16) in equation (4.33) gives:

$$V = \frac{1}{2}\int_{V_p} \mathbf{S}^T\mathbf{c}_p\mathbf{S} \,\mathrm{d}V_p + \sum_{i=1,2} \frac{1}{2}\int_{V_{pe,i}} \left(-\mathbf{S}^T\mathbf{e}_{pe}E_{pe} + \mathbf{S}^T\mathbf{c}_{pe}^E\mathbf{S}\right) \,\mathrm{d}V_{pe,i} \tag{4.35}$$

Then, substituting equation (4.16) in equation 4.34:

$$W_e^* = \sum_{i=1,2} \frac{1}{2}\int_{V_{pe,i}} \left(E_{pe}\varepsilon_{pe}^{\mathbf{S}}E_{pe} + E_{pe}\mathbf{e}_{pe}^T\mathbf{S}\right) \,\mathrm{d}V_{pe,i} \tag{4.36}$$

On the other hand, the work done by non-conservative actions is composed of three contributions: the work done by the external uncorrelated transverse forces exciting the panel; the work done by the damping forces exerted by the interaction between the panel flexural vibration and the fluid and the work done by the external currents applied to the piezoelectric patches; which are respectively represented in equations 4.37, 4.38 and 4.39.

$$W_{nc}^{f} = \int_{A_p} f w \, \mathrm{d}A_p \tag{4.37}$$

$$W_{nc}^{d} = -\int_{A_p} \mu \dot{w} w \, \mathrm{d}A_p \tag{4.38}$$

$$W_{nc}^{i} = -\sum_{i=1,2} \int_{A_{pe,i}} \sigma v_{pe} \, \mathrm{d}A_{pe,i} \tag{4.39}$$

where f is the uncorrelated transverse force excitation per unit surface, w the transverse displacement at position (x, y) of the plate, μ is the viscous damping factor per unit surface and σ are the surface charge densities set at the electrodes of the two piezoelectric patches. So, the total work done by non-conservative forces is defined by:

$$W_{nc} = W_{nc}^{f} + W_{nc}^{d} + W_{nc}^{i} = \int_{A_p} f w \, \mathrm{d}A_p - \int_{A_p} \mu \dot{w} w \, \mathrm{d}A_p - \sum_{i=1,2} \int_{A_{pe,i}} \sigma v_{pe} \, \mathrm{d}A_{pe,i} \tag{4.40}$$

4.2.3 *Variation indicator*

The variations of the Lagrangian and of the work of the non-conservative actions are derived as follows

$$\delta L = \frac{\partial L}{\partial \dot{w}} \delta \dot{w} + \frac{\partial L}{\partial \mathbf{S}} \delta \mathbf{S} + \frac{\partial L}{\partial E_{pe}} \delta E_{pe} \tag{4.41}$$

$$\delta W_{nc} = \frac{\partial W_{nc}}{\partial w} \delta w + \frac{\partial W_{nc}}{\partial v_{pe}} \delta v_{pe} \tag{4.42}$$

Recalling that the Lagrangian has three contributions, the variations are calculated for each one of them:

$$\delta T^{*} = \frac{\partial T^{*}}{\partial \dot{w}} \delta \dot{w} + \frac{\partial T^{*}}{\partial \mathbf{S}} \delta \mathbf{S} + \frac{\partial T^{*}}{\partial E_{pe}} \delta E_{pe} \tag{4.43}$$

$$\delta V = \frac{\partial V}{\partial \dot{w}} \delta \dot{w} + \frac{\partial V}{\partial \mathbf{S}} \delta \mathbf{S} + \frac{\partial V}{\partial E_{pe}} \delta E_{pe} \tag{4.44}$$

$$\delta W_{e}^{*} = \frac{\partial W_{e}^{*}}{\partial \dot{w}} \delta \dot{w} + \frac{\partial W_{e}^{*}}{\partial \mathbf{S}} \delta \mathbf{S} + \frac{\partial W_{e}^{*}}{\partial E_{pe}} \delta E_{pe} \tag{4.45}$$

Then, solving all these operations yields:

$$\frac{\partial T^*}{\partial \dot{w}}\delta\dot{w} = \int_{V_p} \rho_p \dot{w}\delta\dot{w}\,\mathrm{d}V_p + \sum_{i=1,2}\int_{V_{pe,i}} \rho_{pe}\dot{w}\delta\dot{w}\,\mathrm{d}V_{pe,i} \tag{4.46}$$

$$\frac{\partial T^*}{\partial \mathbf{S}}\delta\mathbf{S} = 0 \tag{4.47}$$

$$\frac{\partial T^*}{\partial E_{pe}}\delta E_{pe} = 0 \tag{4.48}$$

$$\frac{\partial V}{\partial \dot{w}}\delta\dot{w} = 0 \tag{4.49}$$

$$\frac{\partial V}{\partial \mathbf{S}}\delta\mathbf{S} = \int_{V_p} \delta\mathbf{S}^T\mathbf{c}_p\mathbf{S}\,\mathrm{d}V_p + \sum_{i=1,2}\frac{1}{2}\int_{V_{pe,i}} \left(-\delta\mathbf{S}^T\mathbf{e}_{pe}E_{pe} + 2\delta\mathbf{S}^T\mathbf{c}_{pe}^E\mathbf{S}\right)\,\mathrm{d}V_{pe,i} \tag{4.50}$$

$$\frac{\partial V}{\partial E_{pe}}\delta E_{pe} = -\sum_{i=1,2}\frac{1}{2}\int_{V_{pe,i}} \delta E_{pe}\mathbf{S}^T\mathbf{e}_{pe}\,\mathrm{d}V_{pe,i} \tag{4.51}$$

$$\frac{\partial W_e^*}{\partial \dot{w}}\delta\dot{w} = 0 \tag{4.52}$$

$$\frac{\partial W_e^*}{\partial \mathbf{S}}\delta\mathbf{S} = \sum_{i=1,2}\frac{1}{2}\int_{V_{pe,i}} E_{pe}\mathbf{e}_{pe}^T\delta\mathbf{S}\,\mathrm{d}V_{pe,i} \tag{4.53}$$

$$\frac{\partial W_e^*}{\partial E_{pe}}\delta E_{pe} = \sum_{i=1,2}\frac{1}{2}\int_{V_{pe,i}} \left(2\delta E_{pe}\varepsilon_{pe}^{\mathbf{S}}E_{pe} + \delta E_{pe}\mathbf{e}_{pe}^T\mathbf{S}\right)\,\mathrm{d}V_{pe,i} \tag{4.54}$$

While solving the derivatives for equation 4.42 yields

$$\frac{\partial W_{nc}}{\partial w}\delta w = \int_{A_p} f\delta w\,\mathrm{d}A_p - \int_{A_p} \mu\dot{w}\delta w\,\mathrm{d}A_p \tag{4.55}$$

$$\frac{\partial W_{nc}}{\partial v_{pe}}\delta v_{pe} = -\sum_{i=1,2}\int_{A_{pe,i}} \sigma\delta v_{pe}\,\mathrm{d}A_{pe,i} \tag{4.56}$$

Then, the variation of the Lagrangian is the sum of all terms from equation (4.46) to equation (4.56), which gives

$$\begin{aligned}\int_{t1}^{t2}\Bigg\{ &\int_{V_p} \rho_p \dot{w}\delta\dot{w}\,\mathrm{d}V_p + \sum_{i=1,2}\int_{V_{pe,i}} \rho_{pe}\dot{w}\delta\dot{w}\;\mathrm{d}V_{pe,i} - \int_{V_p} \delta\mathbf{S}^T\mathbf{c}_p\mathbf{S}\;\mathrm{d}V_p \\ &+ \sum_{i=1,2}\frac{1}{2}\int_{V_{pe,i}} \Big(\delta\mathbf{S}^T\mathbf{e}_{pe}E_{pe} - 2\delta\mathbf{S}^T\mathbf{c}_{pe}^E\mathbf{S} + \delta E_{pe}\mathbf{S}^T\mathbf{e}_{pe} + E_{pe}\mathbf{e}_{pe}^T\delta\mathbf{S} \\ &+2\delta E_{pe}\varepsilon_{pe}^{\mathbf{S}}E_{pe} + \delta E_{pe}\mathbf{e}_{pe}^T\mathbf{S}\Big)\;\mathrm{d}V_{pe,i} + \int_{A_p} f\delta w\;\mathrm{d}A_p \\ &- \int_{A_p}\mu\dot{w}\delta w\;\mathrm{d}A_p - \sum_{i=1,2}\int_{A_{pe,i}}\sigma\delta v_{pe}\;\mathrm{d}A_{pe,i}\Bigg\}\;\mathrm{d}t = 0\end{aligned} \tag{4.57}$$

Considering that $\mathbf{S}$ and $\mathbf{e}_{pe}$ are column vectors, equation (4.57) can be simplified into:

$$\begin{aligned}\int_{t1}^{t2}\Bigg\{ &\int_{V_p} \rho_p \dot{w}\delta\dot{w}\,\mathrm{d}V_p + \sum_{i=1,2}\int_{V_{pe,i}} \rho_{pe}\dot{w}\delta\dot{w}\;\mathrm{d}V_{pe,i} - \int_{V_p} \delta\mathbf{S}^T\mathbf{c}_p\mathbf{S}\;\mathrm{d}V_p \\ &+ \sum_{i=1,2}\int_{V_{pe,i}} \Big(\delta\mathbf{S}^T\mathbf{e}_{pe}E_{pe} - \delta\mathbf{S}^T\mathbf{c}_{pe}^E\mathbf{S} + \delta E_{pe}\varepsilon_{pe}^{\mathbf{S}}E_{pe} + \delta E_{pe}\mathbf{e}_{pe}^T\mathbf{S}\Big)\;\mathrm{d}V_{pe,i} \\ &+ \int_{A_p} f\delta w\;\mathrm{d}A_p - \int_{A_p}\mu\dot{w}\delta w\;\mathrm{d}A_p - \sum_{i=1,2}\int_{A_{pe,i}}\sigma\delta v_{pe}\;\mathrm{d}A_{pe,i}\Bigg\}\;\mathrm{d}t = 0\end{aligned} \tag{4.58}$$

Then, considering that the operators $\delta(\dots)$ and $\partial(\dots)/\partial t$ are commutative, the first two terms of equation (4.58) are integrated by parts [93]; and recalling that $\delta w = 0$ for $t = t_1$ and $t = t_2$ equation (4.58) can be expressed as:

$$\begin{aligned}\int_{t1}^{t2}\Bigg\{ &-\int_{V_p} \rho_p \ddot{w}\delta w\,\mathrm{d}V_p - \sum_{i=1,2}\int_{V_{pe,i}} \rho_{pe}\ddot{w}\delta w\;\mathrm{d}V_{pe,i} - \int_{V_p} \delta\mathbf{S}^T\mathbf{c}_p\mathbf{S}\;\mathrm{d}V_p \\ &+ \sum_{i=1,2}\int_{V_{pe,i}} \Big(\delta\mathbf{S}^T\mathbf{e}_{pe}E_{pe} - \delta\mathbf{S}^T\mathbf{c}_{pe}^E\mathbf{S} + \delta E_{pe}\varepsilon_{pe}^{\mathbf{S}}E_{pe} + \delta E_{pe}\mathbf{e}_{pe}^T\mathbf{S}\Big)\;\mathrm{d}V_{pe,i} \\ &+ \int_{A_p} f\delta w\;\mathrm{d}A_p - \int_{A_p}\mu\dot{w}\delta w\;\mathrm{d}A_p - \sum_{i=1,2}\int_{A_{pe,i}}\sigma\delta v_{pe}\;\mathrm{d}A_{pe,i}\Bigg\}\;\mathrm{d}t = 0\end{aligned} \tag{4.59}$$

Substituting the strain-displacement relation and the electric field-electric potential relation given in equations (4.11) and (4.14) respectively yields the following integral expression

$$\begin{aligned} &\int_{t1}^{t2} \Bigg\{ -\int_{V_p} \rho_p \ddot{w}\delta w \,\mathrm{d}V_p - \sum_{i=1,2} \int_{V_{pe,i}} \rho_{pe} \ddot{w}\delta w \,\mathrm{d}V_{pe,i} - \int_{V_p} z^2 \delta \mathbf{K}^T \mathbf{c}_p \mathbf{K} \,\mathrm{d}V_p \\ &+ \sum_{i=1,2} \int_{V_{pe,i}} \left(\frac{z}{h_{pe}} \delta \mathbf{K}^T \mathbf{e}_{pe} v_{pe} - z^2 \delta \mathbf{K}^T \mathbf{c}_{pe}^E \mathbf{K} + \frac{1}{h_{pe}^2} \delta v_{pe} \varepsilon_{pe}^{\mathbf{S}} v_{pe} + \frac{z}{h_{pe}} \delta v_{pe} \mathbf{e}_{pe}^T \mathbf{K} \right) \,\mathrm{d}V_{pe,i} \\ &+ \int_{A_p} f\delta w \,\mathrm{d}A_p - \int_{A_p} \mu \dot{w} \delta w \,\mathrm{d}A_p - \sum_{i=1,2} \int_{A_{pe,i}} \sigma \delta v_{pe} \,\mathrm{d}A_{pe,i} \Bigg\} \,\mathrm{d}t = 0 \end{aligned} \tag{4.60}$$

The next step is breaking the volume integrals into a product of area and thickness integrals, and solving these thickness integrals the following expression is obtained

$$\begin{aligned} &\int_{t1}^{t2} \Bigg\{ -\int_{A_p} m_p \ddot{w}\delta w \,\mathrm{d}A_p - 2\int_{A_{pe,i}} m_{pe} \ddot{w}\delta w \,\mathrm{d}A_{pe,i} - \int_{A_p} I_p \delta \mathbf{K}^T \mathbf{c}_p \mathbf{K} \,\mathrm{d}A_p \\ &+ 2\int_{A_{pe,i}} \left(z_{pe} \delta \mathbf{K}^T \mathbf{e}_{pe} v_{pe} - I_{pe} \delta \mathbf{K}^T \mathbf{c}_{pe}^E \mathbf{K} + \frac{1}{h_{pe}} \delta v_{pe} \varepsilon_{pe}^{\mathbf{S}} v_{pe} + z_{pe} \delta v_{pe} \mathbf{e}_{pe}^T \mathbf{K} \right) \,\mathrm{d}A_{pe,i} \\ &+ \int_{A_p} f\delta w \,\mathrm{d}A_p - \int_{A_p} \mu \dot{w} \delta w \,\mathrm{d}A_p - \sum_{i=1,2} \int_{A_{pe,i}} \sigma \delta v_{pe} \,\mathrm{d}A_{pe,i} \Bigg\} \,\mathrm{d}t = 0 \end{aligned} \tag{4.61}$$

where:

$$m_p = \rho_p h_p \tag{4.62}$$

$$m_{pe} = \rho_{pe} h_{pe} \tag{4.63}$$

$$z_{pe} = \int_{z_0}^{z_1} \frac{z}{h_{pe}} \,\mathrm{d}z = \int_{z_2}^{z_3} \frac{z}{h_{pe}} \,\mathrm{d}z = -\frac{h_p + h_{pe}}{2} \tag{4.64}$$

$$I_p = \int_{z_1}^{z_2} z^2 \,\mathrm{d}z = \frac{h_p^3}{12} \tag{4.65}$$

$$I_{pe} = \int_{z_0}^{z_1} z^2 \,\mathrm{d}z + \int_{z_1}^{z_3} z^2 \,\mathrm{d}z = \alpha \frac{h_{pe}^3}{12} \tag{4.66}$$

$$\alpha = 6\left(\frac{h_p}{h_{pe}}\right)^2 + 12\left(\frac{h_p}{h_{pe}}\right) + 8 \tag{4.67}$$

The thicknesses z_0, z_1, z_2 and z_3, shown in figure 4.2, are defined as

$$z_0 = -\left[\frac{h_p}{2} + h_{pe}\right] \tag{4.68}$$

$$z_1 = -\frac{h_p}{2} \tag{4.69}$$

$$z_2 = \frac{h_p}{2} \tag{4.70}$$

$$z_3 = \frac{h_p}{2} + h_{pe} \tag{4.71}$$

4.2.4 *Solution using Galerkin's method*

The transverse displacement of the plate with the piezoelectric transducers is separable in space and time variables for synchronous motions [94], which allows its representation in terms of a modal summation as follows

$$w(x,y,z) = [\phi_{n_1} \dots \phi_{n_R}] \begin{bmatrix} q_1(t) \\ \vdots \\ q_R(t) \end{bmatrix} = \boldsymbol{\varphi}(x,y)\mathbf{q}(t) \tag{4.72}$$

where $\phi_{n_R}(x,y)$ are the R natural modes of the plate with no piezoelectric patches and $q_R(t)$ are the R generalised coordinates for the transverse vibrations of the plate. The plate is assumed simply supported, therefore it is characterised by the following natural modes and natural frequencies:

$$\phi_{nr}(x,y) = 2\,\sin\left(\frac{r_1 \pi x}{l_x}\right)\sin\left(\frac{r_2 \pi y}{l_y}\right) \tag{4.73}$$

$$\omega_{nr} = \sqrt{\frac{Y_p h_p^2}{12\rho_p(1-\nu_p^2)}}\left[\left(\frac{r_1\pi}{l_x}\right)^2 + \left(\frac{r_2\pi}{l_y}\right)^2\right] \tag{4.74}$$

where r_1 and r_2 are the mode indexes.

Substituting the modal summation for the transverse displacement presented in equation (4.72) and allowing arbitrary variations of $\mathbf{q}(t)$ and $v_{pe}(t)$, which are equal to zero for $t = t_1$ and $t = t_2$, yields the following two matrix equations [92]

$$\left[\mathbf{M}_p + \mathbf{M}_{pe}\right]\ddot{\mathbf{q}}(t) + \mathbf{C}_p\dot{\mathbf{q}}(t) + \left[\mathbf{K}_p + \mathbf{K}_{pe}\right]\mathbf{q}(t) + \boldsymbol{\Theta}_{pe}v_{pe}(t) = \boldsymbol{\Phi}(t) \tag{4.75}$$

$$-\boldsymbol{\Theta}_{pe}^T \mathbf{q}(t) + C_{pe} v_{pe}(t) = q_{pe}(t) \tag{4.76}$$

where q_{pe} is the charge produced by the piezoelectric transducers, $\mathbf{M}_p$, $\mathbf{C}_p$, $\mathbf{K}_p$ are the modal mass, modal damping and modal stiffness matrix of the plate, $\mathbf{M}_{pe}$, $\mathbf{K}_{pe}$ and $\boldsymbol{\Theta}_{pe}$ are the modal mass, modal stiffness and modal electromechanical transduction coefficient of the piezoelectric patches, C_{pe} is the capacitance of both piezoelectric transducers and $\boldsymbol{\Phi}$ is the vector with the modal amplitudes of the generalised primary forces. These matrices and vectors are defined as:

$$\mathbf{M}_p = m_p \int_{A_p} \boldsymbol{\varphi}^T(x,y)\boldsymbol{\varphi}(x,y)\mathrm{d}A_p = m_p\mathbf{I} \tag{4.77}$$

$$\mathbf{C}_p = \int_{A_p} \mu\boldsymbol{\varphi}^T(x,y)\boldsymbol{\varphi}(x,y)\mathrm{d}A_p = 2m_p\xi_p\boldsymbol{\Omega} \tag{4.78}$$

$$\mathbf{K}_p = I_p \int_{A_p} \boldsymbol{\psi}^T(x,y)\mathbf{c}_p\boldsymbol{\psi}(x,y)\mathrm{d}A_p = m_p\boldsymbol{\Omega}^2 \tag{4.79}$$

$$\mathbf{M}_{pe} = 2m_{pe} \int_{A_{pe}} \boldsymbol{\varphi}^T(x,y)\boldsymbol{\varphi}(x,y)\mathrm{d}A_{pe} \tag{4.80}$$

$$\mathbf{K}_{pe} = 2I_{pe} \int_{A_{pe}} \boldsymbol{\psi}^T(x,y)\mathbf{c}_{pe}^E\boldsymbol{\psi}(x,y)\mathrm{d}A_{pe} \tag{4.81}$$

$$\boldsymbol{\Theta}_{pe} = 2z_{pe} \int_{A_{pe}} \boldsymbol{\psi}^T(x,y)\mathbf{e}_{pe}\mathrm{d}A_{pe} \tag{4.82}$$

$$\boldsymbol{\Phi} = \int_{A_p} \boldsymbol{\varphi}^T(x,y)f(x,y)\mathrm{d}A_p \tag{4.83}$$

$$C_{pe} = 2\frac{\varepsilon_{pe}^S A_{pe}}{h_{pe}} \tag{4.84}$$

where $\mathbf{I}$ is an identity $R \times R$ matrix, ξ_p is the modal damping ratio assumed to be equal for all modes, and

$$\boldsymbol{\psi}(x,y) = \begin{bmatrix} \boldsymbol{\varphi}_{,xx}(x,y) \\ \boldsymbol{\varphi}_{,yy}(x,y) \\ 2\boldsymbol{\varphi}_{,xy}(x,y) \end{bmatrix} \tag{4.85}$$

$$\boldsymbol{\Omega} = \begin{bmatrix} \omega_{n1} & & \\ & \ddots & \\ & & \omega_{nR} \end{bmatrix} \tag{4.86}$$

The plate mass and stiffness matrices are diagonal while the piezoelectric transducers mass and stiffness matrices are fully populated, which means that the inertial and stiffness effects of the patches couple the modal responses of the plate based on the natural modes of the plate without patches. For the complete calculation of these matrices see appendix B.

It is convenient to calculate the derivative of equation (4.76) to work with current instead of total charges, then the following expression is obtained

$$-\boldsymbol{\Theta}_{pe}^T \dot{\mathbf{q}}(t) + C_{pe}\dot{v}_{pe}(t) = i_s(t) \tag{4.87}$$

where i_{pe} is the current flowing trough the piezoelectric patches. Then, another equation is used to describe the shunt circuit, considering the most general case analysed here where an RLC parallel is used and according to the sign convention shown in figure 4.3 the governing equation is

$$i_{pe}(t) = -\left[\frac{1}{R_s}v_{pe}(t) + \frac{1}{L_s}\int v_{pe}(t)\mathrm{d}t + C_s\dot{v}_{pe}(t)\right] \tag{4.88}$$

4.2.5 *Frequency domain formulation*

The variables presented in the previous section can be expressed in terms of phasors in the form

$$f(t) = f(\omega)e^{j\omega t}$$

where harmonic motion is assumed and where ω is the circular frequency and $f(\omega)$ is the complex amplitude. Then, the three differential equations (4.75), (4.87) and (4.87) that describe the response of the panel with the pair of shunted piezoelectric transducers can be expressed as

$$\left[-\omega^2\mathbf{M} + j\omega\mathbf{C}_p + \mathbf{K}\right]\mathbf{q}(\omega) + \boldsymbol{\Theta}_{pe}v_{pe}(\omega) = \boldsymbol{\Phi}(\omega) \tag{4.89}$$

$$-j\omega\boldsymbol{\Theta}_{pe}^T\mathbf{q}(\omega) + j\omega C_{pe}v_{pe}(\omega) = i_s(\omega) \tag{4.90}$$

$$v_{pe}(\omega) = v_s(\omega) = -Z_s(\omega)i_s(\omega) \tag{4.91}$$

where $\mathbf{M}$ and $\mathbf{K}$ are the fully populated matrices containing respectively the sum of the modal mass matrices of the plate $\mathbf{M}_p$ and patches $\mathbf{M}_{pe}$ and of the modal stiffness matrices of the plate $\mathbf{K}_p$ and patches $\mathbf{K}_{pe}$, $\mathbf{\Phi}(\omega)$ is the vector containing the complex amplitudes of the generalised primary forces, $\mathbf{q}$ is the vector with the amplitudes of the generalised coordinates, $v_{pe}(\omega)$ and $i_{pe}(\omega)$ are the complex amplitudes of the voltage and current and $Z_s(\omega)$ is the impedance of the shunt circuit, defined for the parallel RLC shunt in equation (4.92) and for the parallel RL circuit in equation (4.93)

$$Z_s^{RLC}(\omega) = \frac{j\omega L_s R_s}{R_s + j\omega L_s - \omega^2 R_s L_s C_s} \tag{4.92}$$

$$Z_s^{RL}(\omega) = \frac{j\omega L_s R_s}{R_s + j\omega L_s} \tag{4.93}$$

Substituting the current in equation (4.90) using equation (4.91) and the resulting voltage into equation (4.89) yields

$$\left[-\omega^2\mathbf{M} + j\omega\left(\mathbf{C}_p + Z_{spe}\mathbf{\Pi}_{pe}\right) + \mathbf{K}\right]\mathbf{q}(\omega) = \mathbf{\Phi}(\omega) \tag{4.94}$$

where $\mathbf{\Pi}_{pe}$ and Z_{spe} are respectively the electromechanical coupling matrix defined in equation 4.95 and the impedance of the shunt in parallel with the impedance of patches defined in equation 4.96 for the RLC shunt and in equation 4.97 for the RL shunt.

$$\mathbf{\Pi}_{pe} = \mathbf{\Theta}_{pe}\mathbf{\Theta}_{pe}^T \tag{4.95}$$

$$Z_{spe}^{RLC}(\omega) = \frac{j\omega L_s R_s}{R_s + j\omega L_s - \omega^2 R_s L_s \left(C_s + C_{pe}\right)} \tag{4.96}$$

$$Z_{spe}^{RL}(\omega) = \frac{j\omega L_s R_s}{R_s + j\omega L_s - \omega^2 R_s L_s C_{pe}} \tag{4.97}$$

Equation (4.94) is defined by R second order differential equations mechanically coupled via the fully populated total mass and total stiffness matrices $\mathbf{M}$ and $\mathbf{K}$ but also electromechanically via the fully populated coupling matrix $\mathbf{\Pi}$. The mechanical coupling appears because the response of the plate has been expanded with reference to the natural modes of the plate without the piezoelectric transducers. Then, the next step is to derive a new set of generalised coordinates in which the total mass and stiffness matrices are diagonal. Considering the free response ($\mathbf{\Phi} = 0$) with the patches in short circuit ($v_{pe} = 0$) and neglecting the structural damping ($\mathbf{C}_p = 0$) equation (4.94) becomes

$$\left[-\omega^2\mathbf{M} + \mathbf{K}\right]\mathbf{q}(\omega) = 0 \tag{4.98}$$

By solving this eigenvalue-eigenvector problem the natural frequencies and natural modes of the plate with the piezoelectric transducers are obtained as

$$\hat{\omega}_{nr} = \sqrt{\lambda_r} \tag{4.99}$$

$$\hat{\phi}_{nr}(x, y) = \boldsymbol{\varphi}(x, y)\hat{\mathbf{q}}_r \tag{4.100}$$

where λ_r and $\hat{\mathbf{q}}_r$ are respectively the r-th eigenvalue and the r-th eigenvector. All eigenvectors can be collected in an eigenvector matrix defined as

$$\mathbf{V} = [\hat{\mathbf{q}}_1 \ldots \hat{\mathbf{q}}_R] \tag{4.101}$$

This matrix $\mathbf{V}$ is used to diagonalise the total mass and total stiffness matrices after setting

$$\mathbf{q}(\omega) = \mathbf{V}\hat{\mathbf{q}}(\omega) \tag{4.102}$$

where the vector $\hat{\mathbf{q}}(\omega)$ contains the new generalised coordinates. Substituting 4.102 into equation 4.94 and pre-multiplying by $\mathbf{V}^T$ gives the following new set of R differential equations in the new generalised coordinates

$$\left[-\omega^2\hat{\mathbf{M}} + j\omega\left(\hat{\mathbf{C}} + Z_{spe}\hat{\mathbf{\Pi}}\right) + \hat{\mathbf{K}}\right]\hat{\mathbf{q}}(\omega) = \hat{\mathbf{\Phi}}(\omega) \tag{4.103}$$

where the new modal matrices are defined as

$$\hat{\mathbf{M}} = \mathbf{V}^T\mathbf{M}\mathbf{V} \tag{4.104}$$

$$\hat{\mathbf{C}} = \mathbf{V}^T\mathbf{C}_p\mathbf{V} \tag{4.105}$$

$$\hat{\mathbf{K}} = \mathbf{V}^T\mathbf{K}\mathbf{V} \tag{4.106}$$

$$\hat{\mathbf{\Pi}} = \mathbf{V}^T\mathbf{\Pi}_{pe}\mathbf{V} \tag{4.107}$$

$$\hat{\mathbf{\Phi}} = \mathbf{V}^T\mathbf{\Phi}\mathbf{V} \tag{4.108}$$

It is important to note that the new modal matrices for the total mass and stiffness are now diagonal, while the modal damping and modal electromechanical coupling matrices are fully populated. In effect, the modal equations of motion using the new generalised coordinates $\hat{\mathbf{q}}$ are coupled via the electromechanical coupling effect and via the damping effect. However, as the latter can be neglected for small damping effects, also the new modal damping matrix $\hat{\mathbf{C}}$ is diagonal.

4.2.6 *Spectral analysis of the structure response*

As shown in [12], the flexural response of the plate is derived in terms of the kinetic energy PSD of the plate and piezoelectric patches, derived with the following expression [95, 96]

$$\begin{aligned} S_K(\omega) = &\frac{1}{2}\int_{A_p} \rho_p h_p \lim_{T\to\infty} E\left[\frac{1}{T}\dot{w}^*(x,y,\omega)\dot{w}(x,y,\omega)\right] dA_p \\ &+ \frac{1}{2}\int_{A_{pe}} 2\rho_{pe} h_p \lim_{T\to\infty} E\left[\frac{1}{T}\dot{w}^*(x,y,\omega)\dot{w}(x,y,\omega)\right] dA_{pe} \end{aligned} \tag{4.109}$$

where the superscript * is used to indicate the complex conjugate operator, $\dot{w}(x,y,\omega)$ is the finite Fourier transform of $\dot{w}(x,y,t)$ which according to equations (4.72) and (4.100) is defined by:

$$\dot{w}^*(x,y,\omega) = \boldsymbol{\varphi}(x,y)\dot{\mathbf{q}}(\omega) = \boldsymbol{\varphi}(x,y)\mathbf{V}^T\dot{\hat{\mathbf{q}}}(\omega) \tag{4.110}$$

where $\dot{\mathbf{q}}(\omega)$ and $\dot{\hat{\mathbf{q}}}(\omega)$ are respectively the finite Fourier transform of the vectors $\dot{\mathbf{q}}(t)$ and $\dot{\hat{\mathbf{q}}}(t)$ containing the generalised modal velocities of the panel. Substituting (4.110) in (4.109) gives [12]

$$S_K(\omega) = \frac{1}{2}Tr\left[\hat{\mathbf{M}}\mathbf{S}_{\hat{\mathbf{q}}\hat{\mathbf{q}}}(\omega)\right] \tag{4.111}$$

where $Tr[\dots]$ is the trace operator and $\mathbf{S}_{\hat{\mathbf{q}}\hat{\mathbf{q}}}(\omega)$ is the matrix that contains the self and cross PSD functions of the plate modal velocities produced by the random excitation and is defined as

$$\mathbf{S}_{\hat{\mathbf{q}}\hat{\mathbf{q}}}(\omega) = \lim_{T\to\infty} E\left[\frac{1}{T}\dot{\hat{\mathbf{q}}}(\omega)\dot{\hat{\mathbf{q}}}^H(\omega)\right] \tag{4.112}$$

where the vector $\dot{\hat{\mathbf{q}}}(\omega)$ can be derived from equation (4.102) and can be expressed using the following mobility matrix equation

$$\dot{\hat{\mathbf{q}}}(\omega) = \hat{\mathbf{Y}}(\omega)\hat{\boldsymbol{\Phi}}(\omega) \tag{4.113}$$

where $\hat{\mathbf{Y}}(\omega)$ is defined in equation (4.114) and $\hat{\boldsymbol{\Phi}}(\omega)$ is the finite Fourier transform of the vectors with the generalised modal forces $\hat{\boldsymbol{\Phi}}(t)$

$$\hat{\mathbf{Y}}(\omega) = j\omega\left[-\omega^2\hat{\mathbf{M}} + j\omega\left(\hat{\mathbf{C}} + Z_{spe}\hat{\boldsymbol{\Pi}}\right) + \hat{\mathbf{K}}\right]^{-1} \tag{4.114}$$

Then, for a linear time-invariant system, the matrix $\mathbf{S}_{\hat{\mathbf{q}}\hat{\mathbf{q}}}(\omega)$, which contains the modal velocities PSD of the plate and piezoelectric transducers, is derived using the following expression

$$\begin{aligned} \mathbf{S}_{\hat{\mathbf{q}}\hat{\mathbf{q}}}(\omega) &= \lim_{T\to\infty} E\left[\frac{1}{T}\hat{\mathbf{Y}}(\omega)\hat{\mathbf{\Phi}}(\omega)\hat{\mathbf{\Phi}}^T(\omega)\hat{\mathbf{Y}}^H(\omega)\right] \\ &= \hat{\mathbf{Y}}\mathbf{S}_{\hat{\mathbf{\Phi}}\hat{\mathbf{\Phi}}}(\omega)\hat{\mathbf{Y}}^H(\omega) \end{aligned} \tag{4.115}$$

where $\mathbf{S}_{\hat{\mathbf{\Phi}}\hat{\mathbf{\Phi}}}(\omega)$ is the matrix containing the PSD functions of the modal excitaciones, which for the uniform spatial distribution of uncorrelated rain-on-the-roof forces is defined as

$$\mathbf{S}_{\hat{\mathbf{\Phi}}\hat{\mathbf{\Phi}}}(\omega) = \lim_{T\to\infty} E\left[\hat{\mathbf{\Phi}}(\omega)\hat{\mathbf{\Phi}}^T(\omega)\right] \tag{4.116}$$

Using equations (4.83) and (4.108), equation 4.116 can be expressed as

$$\begin{aligned} \mathbf{S}_{\hat{\mathbf{\Phi}}\hat{\mathbf{\Phi}}} &= \lim_{T\to\infty} E\left[\frac{1}{T}\mathbf{V}^T\int_{A_p}\boldsymbol{\varphi}^T(x,y)f(x,y,\omega)\mathrm{d}A_p\int_{A'_p}\boldsymbol{\varphi}(x',y')f^*(x',y',\omega)\mathrm{d}A'_p\mathbf{V}\right]_{\mathbf{V}} \\ &= \mathbf{V}^T\int_{A_p}\int_{A'_p}\boldsymbol{\varphi}^T(x,y)S_{ff}(x,y,x',y',\omega)\boldsymbol{\varphi}(x',y')\mathrm{d}A_p\mathrm{d}A'_p \end{aligned} \tag{4.117}$$

where $S_{ff}(x,y,x',y',\omega)$ is the cross spectral density of the rain-on-the-roof excitation, defined as

$$S_{ff}(x,y,x',y',\omega) = \lim_{T\to\infty} E\left[\frac{1}{T}f(x,y,\omega)f^*(x',y',\omega)\right] \tag{4.118}$$

Finally, the following expression for the kinetic energy PSD is found substituting equation (4.115) into (4.111)

$$S_K(\omega) = \frac{1}{2}Tr\left[\hat{\mathbf{M}}\hat{\mathbf{Y}}\mathbf{S}_{\hat{\mathbf{\Phi}}\hat{\mathbf{\Phi}}}(\omega)\hat{\mathbf{Y}}^H(\omega)\right] \tag{4.119}$$

4.3 SHUNT TUNING

This section is focused on the effect of the modal overlap and of the electromechanical coupling effects on the response of the system when the shunt is tuned to control the first mode of the plate. This study analyses the spectrum of the flexural response of the plate in a narrow frequency band around the first resonance frequency considering an increasing number of modes in the model. The analysis starts with the response of the structure with the shunt in open and short circuit and with a purely resistive shunt. Optimal tuning values for the inductance and resistance are presented for a simplified model. Then, an RL shunt using the latter optimal values is analysed. Finally a RLC shunt is considered to show the effect of a negative capacitance on the system response.

4.3.1 *Effect of the shunt on the structure*

Figure 4.4 shows the 30-60 Hz spectrum of the total flexural kinetic energy PSD of the plate without the piezoelectric transducers (dashed thick black line), with the transducers in short circuit (dash-dotted thin green line), in open circuit (thin dotted magenta line) and using a purely resistive shunt (solid blue line). The optimal resistance for this shunt was found by trial and error. The four plots are obtained considering (a) only the first, (b) the first five, (c) the first fifty and (d) the first one hundred and fifty natural modes of the plate and piezoelectric transducers.

The first resonance peak of the plate can be seen at 39 Hz in the four plots as its value does not change with the number of modes considered in the model. Plot (a) shows that for the three responses involving the transducers (in open and short circuit and connected to a resistive shunt) there is a shift to higher frequencies to around 47 Hz. The short circuit inhibits the electromechanical capacitive effect of the transducers, resulting in a somewhat reduced stiffness effect. As it can be seen in the plot, the resonance peak for the short circuited transducers has the same amplitude as the open circuit one but is located at a slightly lower frequency. Furthermore, the resonance peak is located at an intermediate frequency when the resistive shunt is used and its amplitude is about 6 dB lower due to the electromechanical damping effect produced by the resistor [21]. Although these features remain as the number of natural modes considered in the model increases, they shift always to lower frequencies, close to the fundamental resonance frequency of the plate without patches, as it can be seen in plots (b), (c) and (d). It can also be noted that, the frequency gap between the resonance peak in short circuit and open circuit tends to decrease and also the damping produced by the resistive shunt. For a high number of modes, and as it usually is in real applications, the short and open circuit and resonance peaks are very close to each other and the damping produced by the resistive shunt is rather small.

This example suggests that the modal overlap of the modal responses of the plate with the piezoelectric transducers is relevant even at low frequencies near the fundamental resonance frequency of the plate.

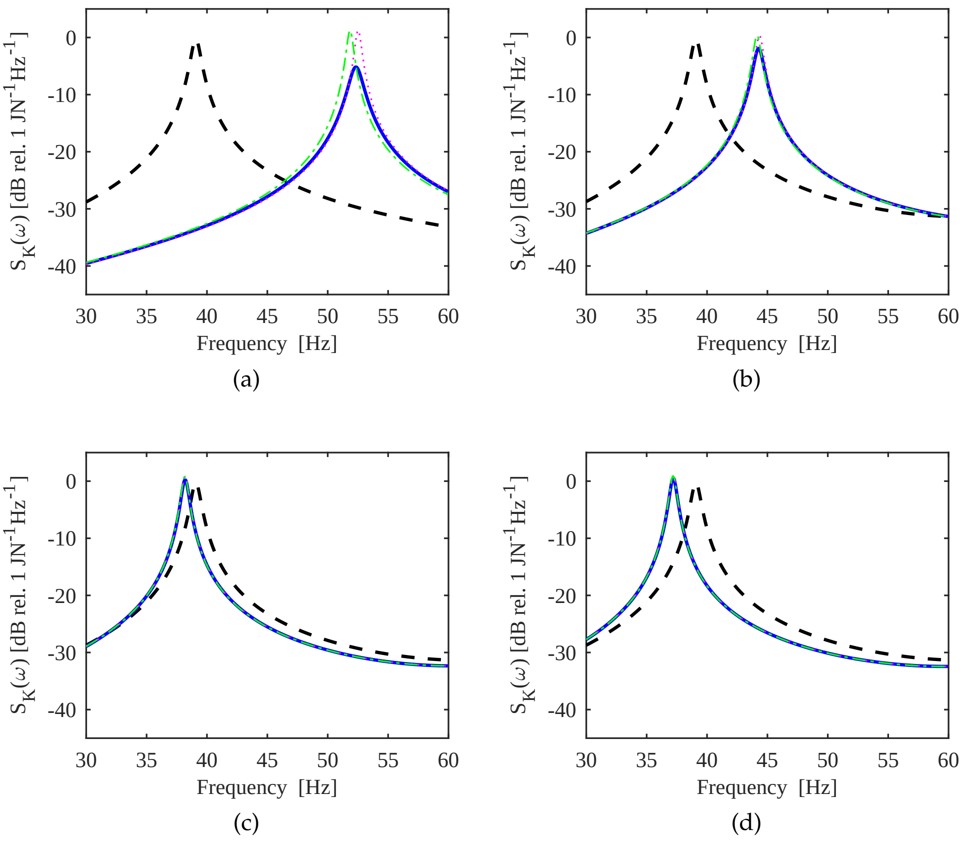

Figure 4.4.: PSD of the total flexural kinetic energy of the plate without the piezoelectric transducers (dashed thick black line) and with them in short circuit (dash-dotted thin green line), in open circuit (thin dotted magenta line) and with a purely resistive shunt (solid blue line) obtained with a model that considers the (a) first mode, (b) first five modes, (c) first fifty modes and (d) first one hundred and fifty modes of the plate and piezoelectric transducers.

4.3.2 *Tuning law for a simplified system*

Hagood and von Flotow [21] showed that the optimal tuning of the electromechanical vibration absorber formed by a shunted piezoelectric patch can be found using the classical formulation proposed by Ormondroyd and Den Hartog [97] for a mechanical vibration absorber. Several norms have been defined over the years to identify the optimal tuning parameters of a classical mechanical vibration absorber, as summarised by Zilletti and Elliott [98]. Here, the optimal values for the RL shunt are derived from an H2 norm [9] given by the time averaged kinetic energy of the plate and piezoelectric transducers per unit rain on the roof excitation; calculated considering the contribution of only the first natural mode and a simplified model where the structural damping is considered to be zero. Then, the performance index to be minimized is given by:

$$I_1 = \frac{1}{2} M_{11} \int_{-\infty}^{\infty} |\hat{Y}_{11}(\omega)|^2 d\omega \tag{4.120}$$

where Y_{11} is the mobility function for the first mode of the plate and transducers, which according to equation (4.114) is given by:

$$\hat{Y}_{11}(\omega) = \frac{j\omega}{-\omega^2 \hat{M}_{11} + j\omega Z_{spe} \hat{\Pi}_{11} + \hat{K}_{11}} \tag{4.121}$$

where $\hat{M}_{11}$, $\hat{K}_{11}$ and $\hat{\Pi}_{11}$ are the modal mass, stiffness and electromechanical transduction coefficient related to the first mode of the plate and patches. The solution of the integral presented in equation (4.120) is obtained using the formulation found in the appendix of reference [99], which leads to:

$$I_1 = \frac{1}{2} \hat{M}_{11} \frac{\pi(N_1 + N_2 + N_3 + N_4 + N_5 + N_6 + N_7 + N_8)}{D_1 + D_2 + D_3} \tag{4.122}$$

where:

$$\begin{aligned}
N_1 &= A_0^2 A_3 B_3^2 & D_1 &= A_0^2 A_3^2 A_4 \\
N_2 &= -A_0 A_1 A_2 B_3^2 & D_2 &= A_0 A_1^2 A_4^2 \\
N_3 &= 2 A_0 A_1 A_4 B_1 B_3 & D_3 &= A_0 A_1 A_2 A_3 A_4 \\
N_4 &= -A_0 A_1 A_4 B_2^2 \\
N_5 &= -A_0 A_3 A_4 B_2^1 \\
N_6 &= 2 A_0 A_3 A_4 B_0 B_2 \\
N_7 &= A_1 A_4^2 B_0^2 \\
N_8 &= -A_2 A_3 A_4 B_0^2
\end{aligned}$$

Considering that:

$$\begin{aligned}
A_0 &= \hat{K}_{11} R_s & B_0 &= 0 \\
A_1 &= \hat{K}_{11} L_s & B_1 &= R_s \\
A_2 &= \hat{M}_{11} R_s + \hat{K}_{11} R_s L_s C_{pe} + L_s R_s \hat{\Pi}_{11} & B_2 &= L_s \\
A_3 &= \hat{M}_{11} L_s & B_3 &= R_s L_s C_{pe} \\
A_4 &= \hat{M}_{11} R_s L_s C_{pe}
\end{aligned}$$

equation (4.122) becomes

$$I_1 = \frac{1}{2} \hat{M}_{11} \frac{\pi(A_0^2 A_3 B_3^2 - A_0 A_1 A_2 B_3^2 + 2 A_0 A_1 A_4 B_1 B_3 - A_0 A_1 A_4 B_2^2 - A_0 A_3 A_4 B_2^1)}{A_0^2 A_3^2 A_4 + A_0 A_1^2 A_4^2 + A_0 A_1 A_2 A_3 A_4} \tag{4.123}$$

To find the shunt optimal values, the derivatives of the performance index I_1 with respect to the inductance and resistance are set to zero:

$$\frac{\partial I_1}{\partial L_s} = 0 \tag{4.124}$$

$$\frac{\partial I_1}{\partial R_s} = 0 \tag{4.125}$$

Solving the derivative in equation (4.124) gives:

$$-C_{pe} L_s \hat{K}_{11} + \hat{M}_{11} = 0 \tag{4.126}$$

and from here the optimal inductance value is found to be:

$$L_{s1}^{opt} = \frac{\hat{M}_{11}}{\hat{K}_{11} C_{pe}} \tag{4.127}$$

On the other hand, solving the derivative in equation (4.125) gives the following expression:

$$(C_{pe}^2 \hat{K}_{11}^2 L_s^2 + \hat{\Gamma}_{11} C_{pe} \hat{K}_{11} L_s^2 - 2C_{pe} \hat{M}_{11} \hat{K}_{11} L_s + \hat{M}_{11}^2) R_s^2 = \hat{M}_{11} \hat{K}_{11} L_s^2 \tag{4.128}$$

Then, considering the optimal inductance of equation (4.127) it is possible to find the following expression for the optimal resistance:

$$R_{s1}^{opt} = \sqrt{\frac{\hat{M}_{11}}{\hat{\Gamma}_{11} C_{pe}}} \tag{4.129}$$

The equation (4.127) found for the optimal inductance is similar to the ones derived in references [21, 100, 101]. Instead, the expression (4.129) found for the optimal resistance is different than the ones found in the latter references.

4.3.3 *Tuning based on the multiple mode formulation*

Figure 4.5 presents also four plots in which the PSD of the total flexural kinetic energy is calculated using the (a) first, (b) first five, (c) first fifty and (d) first one hundred and fifty modes of the system. Each plot shows the total flexural kinetic energy PSD of the plate without the piezoelectric transducers (dashed thick black line), with the transducers in short circuit (dash-dotted thin green line), with the transducers connected to an inductive shunt (solid thin red line) and with the transducers connected to an RL shunt (thick solid blue line).

The values for the shunt are the optimal inductance L_{s1}^{opt} and resistance R_{s1}^{opt} obtained in Section 4.3.2.

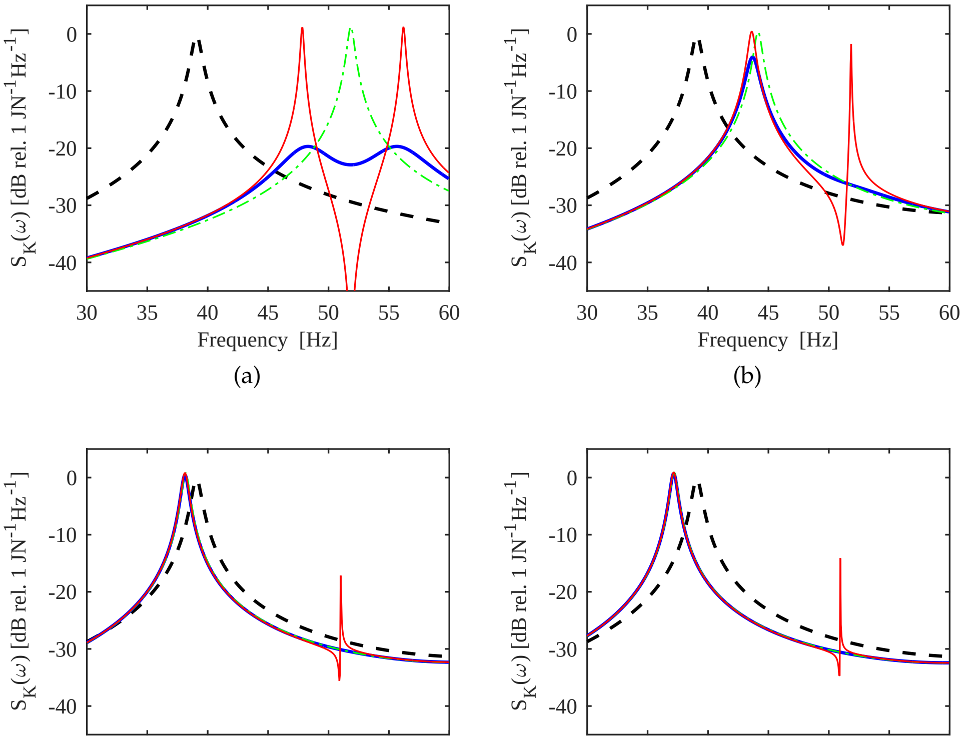

(a) (b)

(c) (d)

Figure 4.5.: PSD of the total flexural kinetic energy of the plate without the piezoelectric transducers (dashed thick black line) and with them in short circuit (dash-dotted thin green line), using an inductive shunt (solid thin red line) and with an RL shunt (thick solid blue line) obtained with a model that considers the (a) first mode, (b) first five modes, (c) first fifty modes and (d) first one hundred and fifty modes of the plate and piezoelectric transducers.

Plot (a) of figure 4.5 shows the classical spectra that characterise the response of a plate with piezoelectric transducers connected to a purely inductive shunt and to an RL shunt perfectly tuned. The shunt with only the inductance L_{s1}^{opt} produces an antiresonance narrow trough at the same frequency where the resonance peak of the short circuited patches occur, and a pair of lightly damped resonance peaks at each side of the narrow trough with the same amplitude than the peak of the system with short circuited patches. These two resonance peaks are rounded off when the optimal resistance R_{s1}^{opt} is added to the shunt, achieving a reduction of their amplitudes of around 20 dB. Plots (b), (c) and

(d) show that by increasing the number of considered modes in the simulation these features are progressively lost. Furthermore, from the two peaks produced by the purely inductive shunt, the one at lower frequency tends to shift significantly to lower frequencies following the response of the short circuited system; while the second peak remains around the same position but has a progressively lower amplitude. In fact, when the resistor is also added to the shunt this second peak disappears and it is difficult to distinguish the response of the RL shunt from the one of the shunt in short circuit. This means that the optimal values for the shunt presented in equations (4.127) and (4.129) for a simplified one mode model are not accurate any more when the model takes into consideration higher order modes.

Because of this, a parametric study was conducted to analyse the tuning of the RL shunt considering an incremental number of modes of the plate and piezoelectric patches in the model. In this study the optimal values for the inductance and resistance are found numerically using a genetic algorithm, whose implementation is discussed in appendix C.

The response of the structure was calculated for a range of pairs of inductance and resistance values in order to obtain three-dimensional plots where the x-axis is the shunt resistance, y-axis is the shunt inductance and the z-axis is the reduction of the total flexural kinetic energy PSD in dB in the 30-60 Hz frequency range. Figure 4.6 shows this surface plots in a top view considering the (a) first, (b) first five, (c) first fifty and (d) first one hundred and fifty modes of the panel. The four plots are characterised by an inverted bell shaped surface, which as the number of considered modes increases is progressively flattened along the horizontal axis. In addition, the minimum tends to shift by small inductance values and much higher resistance values. These plots show that the tuning for the inductance must be quite precise since small variations from the optimal value would produce substantial degradation to the control performance of the piezoelectric vibration absorber. They also suggest that a large number of modes should be used for a correct tuning of the shunt, particularly for the resistance. This is due to two concurrent effects: first, the fact that a plate is characterised by a high modal overlap that rises with frequency such that, at each frequency, the response of the plate is the superposition of multiple modal responses and second, as discussed in Section 4.2, the mechanical and electromechanical coupling between the piezoelectric transducers and the plate occurs along the edges of the transducers, generating high cross coupling effects of the fundamental mode with higher order modes of the panel and transducers.

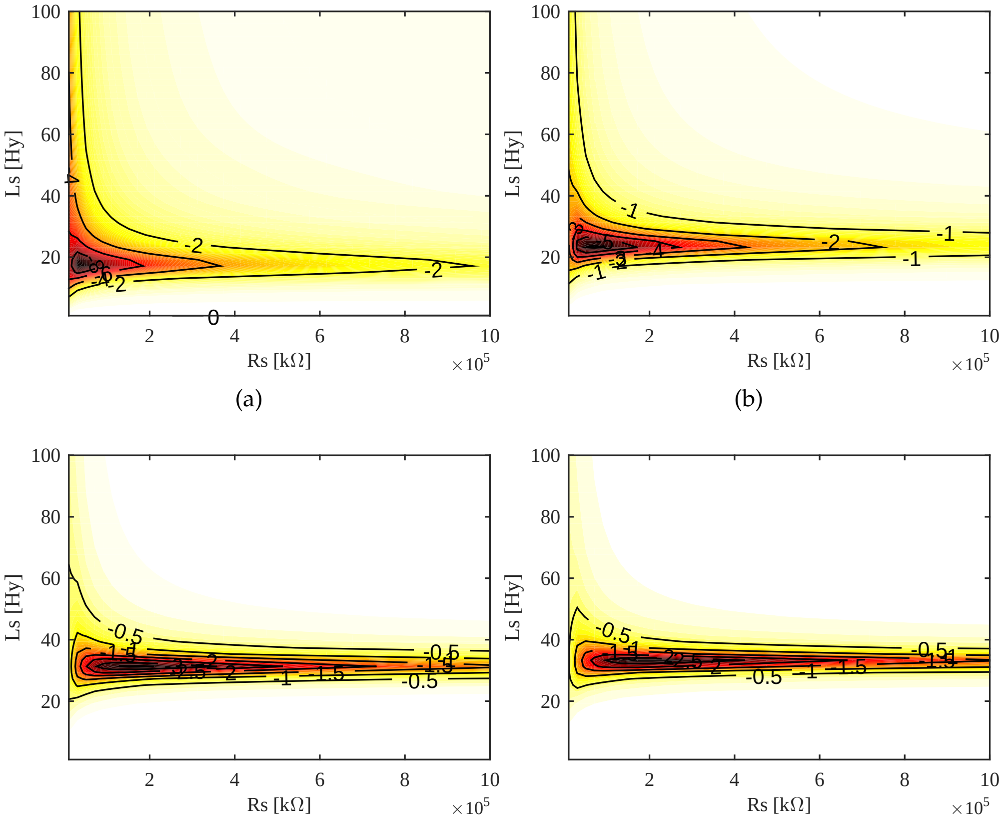

(a) (b) (c) (d)

Figure 4.6.: Reduction in dB of the PSD of the time averaged total flexural kinetic energy of the panel in the 30-60 Hz frequency range calculated with a model that considers the (a) first mode, (b) first five modes, (c) first fifty modes and (d) first one hundred and fifty modes of the plate and piezoelectric transducers.

Figure 4.7 shows the spectra of the plate total flexural kinetic energy PSD when the optimal values shown in figure 4.6 are used. These plots show the response of the plate without piezoelectric transducers (dashed thick black line), with the transducers in open circuit (dotted thin magenta line), in short circuit (dash-dotted thin green line) and connected to an RL shunt (thick solid blue line). In this plots it is possible to see that as the amount of considered modes increases the performance of the shunted vibration absorber diminishes from around 25 dB of peak reduction when only the first mode is taken into account to around 11 dB when 150 modes are used in the simulation.

In order to find the minimum number of modes that should be taken into account to accurately describe the control effect of the RL shunt and to find accurate values for the inductance and resistance, the response of the panel has been calculated iteratively considering from only the first mode up to the first

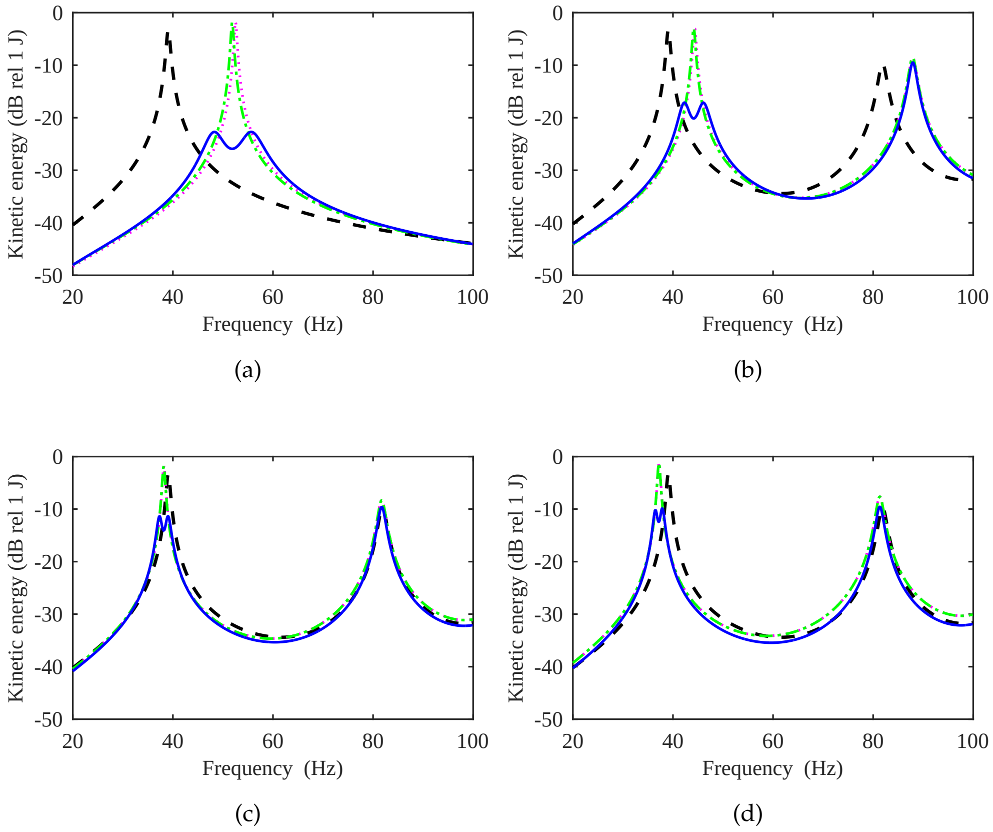

(a)

(b)

(c)

(d)

Figure 4.7.: PSD of the total flexural kinetic energy of the plate without the piezoelectric transducers (dashed thick black line) and with them in open circuit (dotted thin magenta line), in short circuit (dash-dotted thin green line) and connected to a properly tuned RL shunt (thick solid blue line) obtained with a model that considers the (a) first mode, (b) first five modes, (c) first fifty modes and (d) first one hundred and fifty modes of the plate and piezoelectric transducers.

300 modes of the plate and piezoelectric transducers. Figure 4.8a shows the convergence of the total flexural kinetic energy PSD peak reduction in dB in the 30-60 frequency range. The value stabilises to around 11.5 dB when at least the first one hundred modes are considered in the model.

Plot (b) of figure 4.8b shows the convergence of the optimal shunt inductance (blue circles) and resistance (orange crosses); which shows that for an accurate tuning at least 150 modes of the plate with the piezoelectric patches have to be taken into account. The optimal inductance and resistance obtained using only the first mode of the plate and patches are respectively around 50% and 75% lower than the values obtained considering a large number of modes. The values used for figure 4.8 are presented in table 4.3.

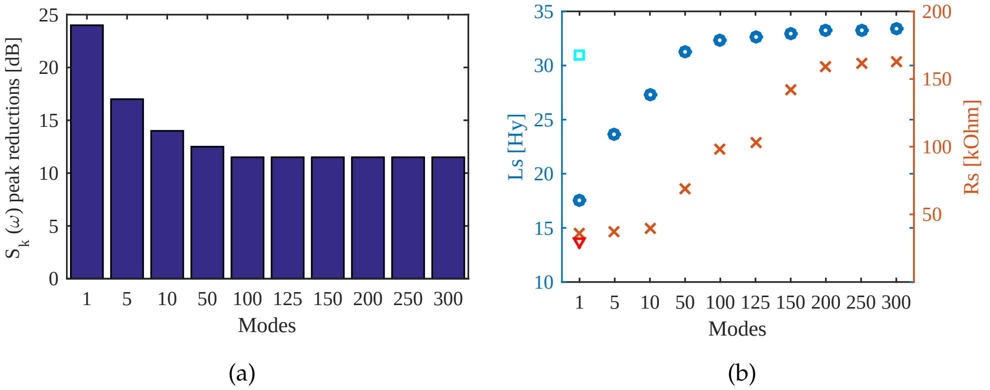

Figure 4.8.: Convergence of the (a) panel total flexural kinetic energy PSD peak reduction and (b) of the optimal inductance and resistance values as the number of considered modes in the model increases. Plot (b): blue circles and orange crosses are respectively the optimal inductance and resistance values considering an increasing amount of natural modes; the cyan square and red triangular markers show the optimal inductance and resistance considering only the first mode of the plain plate.

It is also interesting to note that if the shunt inductance was calculated using the first mode of the plain plate only (square cyan marker in figure 4.8b) the value would be quite close to the one obtained 150 modes of the plate and piezoelectric patches. The same is not true for the resistance, which when calculated using the first mode of the plate only (red triangular marker in figure 4.8b) is much lower than the value obtained considering 150 modes of the plate and piezoelectric patches. The importance of considering a large number of natural modes to predict the response of two dimensional thin structures with piezoelectric patches was also noticed by Elliot *et al.* [52] who considered the response of a plate equipped with multiple feedback loops using small piezoelectric patch actuators.

To conclude this analysis, figure 4.9 shows the spectrum of the total flexural kinetic energy PSD of the plate with no piezoelectric transducers (dashed thick black line), with the transducers connected to a shunt composed of only the optimal inductance and to the optimal inductance and resistance. In contrast to the results shown in figure 4.5d, when the accurate inductance is used, the spectrum of the flexural response is characterised by the two sharp peaks (thin solid red line) which are smoothened by around 11 dB when the accurate resistance is also added to the shunt (thick solid blue line). Another interesting feature shown in figure 4.9 is the effect of adding a negative capacitance to the shunt to reduce the inherent capacitance of the transducer; in this case, by a 75%. By

Table 4.3.: Shunt optimal values and total flexural kinetic energy PSD peak reductions convergence.

Modes	L_s^{opt} $[H]$	R_s^{opt} $[k\Omega]$	S_{K1} peak reduction [dB]
1	17.6	35.5	24
5	23.7	37.5	17
10	27.3	39.2	14
50	31.3	69.2	12.5
100	32.4	98.3	11.5
125	32.6	102.8	11.5
150	33.1	142.2	11.5
200	33.2	159.4	11.5
250	33.3	161.2	11.5
300	33.4	163.1	11.5

reducing the global capacitance of the resonant LC circuit, the two sharp peaks are spread further apart from each other (thin dash-dotted magenta line) and when the optimal resistance is also used (thick dashed-dotted green line) the two peaks are smoothened by around 15 dB. As references [25, 27–31, 36] suggested, the RLC shunt using a negative capacitance is able to produce larger vibration reductions in a frequency band that comprises the response of the targeted mode of the structure.

4.4 ANALYSIS OF THE PIEZOELECTRIC TRANSDUCER DIMENSIONS

A parametric study to asses the effect of the transducers dimensions on the control performance of the shunted piezoelectric vibration absorber is presented in this section. Table 4.4 shows the initial and final dimensions of the pair of piezoelectric transducers. The study considers the flexural vibration control effects at frequencies near the fundamental resonance frequency of the panel. The pair of shunted transducers produce two effects of the panel: a purely me-

Table 4.4.: Dimensions of the piezoelectric transducers for the parametric study.

Dimension	Value
d_x/l_x	5% to 90%
d_y/l_y	5% to 90%
h_{pe}/h_p	10% to 100%

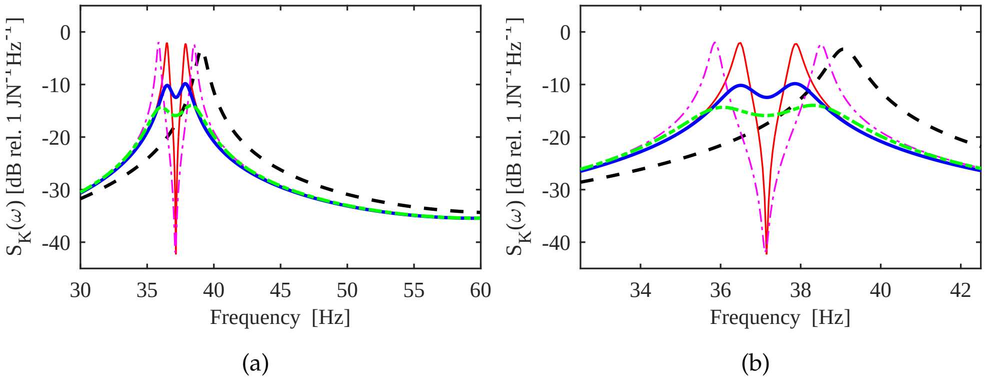

Figure 4.9.: PSD of the total flexural kinetic energy of the plate without the piezoelectric transducers (dashed thick black line) and with them connected to a shunt composed of the optimal inductance only (thin solid red line), the optimal inductance and resistance (thick solid blue line), a negative capacitance and the optimal inductance (thin dash-dotted magenta line) and a negative capacitance and the optimal inductance and resistance (thick dashed-dotted green line) considering the first 150 modes of the plate and transducers for a (a) 30-60 Hz and (b) 33-42.5 Hz frequency range.

chanical stiffness and inertia effect and a vibration absorption electromechanical effect. Figure 4.10a shows the ratio of the total flexural kinetic energy PSD peak value in the 30-60 Hz frequency range for the plate with the transducers in short circuit and the plain plate. This plot suggests that the passive stiffness and inertia effects produced by the pair of piezoelectric transducers have little impact on the peak flexural response of the panel at frequencies close to the fundamental resonance frequency of the panel. In fact, recalling figure 4.4d, the spectrum of the total flexural kinetic energy PSD of the panel with short circuited transducers remains quite similar to the one of the plain plate, with the resonance peak shifted by little to lower frequencies. On the other hand, figure 4.10b presents the ratio of the total flexural kinetic energy PSD peak value of the plate with the transducers connected to an optimally tuned RL shunt and with the transducers in short circuit in the 30-60 Hz frequency band. This plots shows that when the surface and thickness of the patches increases the peak flexural response of the panel drops substantially. The larger is the surface area the higher is the reduction of the peak response of the first natural mode. Also, the blue curve overlapped to plot (b) indicates that the optimal thickness of the piezoelectric patches tends to rise as the lateral dimensions of the patches are increased. This can be explained by the fact that the thicker are the piezoelectric patches the larger is the electromechanical coupling factor and the larger is the bending stiffness of the plate and piezoelectric patches laminate. Then,

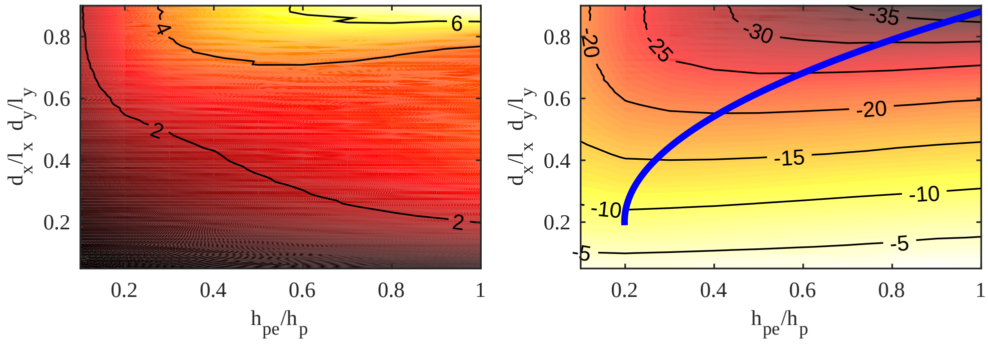

(a) (b)

Figure 4.10.: Ratio in dB of the total flexural kinetic energy PSD peak value in the 30-60 Hz frequency band for the plate (a) with the piezoelectric transducers in short circuit and the plain plate and (b) with the optimally shunted transducers and the short circuited transducers.

while the former effect tends to increase the conversion of the bending strain into electric current flowing into the shunt the second effect tends to reduce the bending strain of the piezoelectric patch and thus the electric current flow into the shunt so that the maximum conversion of mechanical strain energy in electrical energy is obtained for an optimal thickness of the piezoelectric patch [87]. Generally speaking, figure 4.10b indicates that the best vibration control effect is obtained with piezoelectric patches that cover the largest possible portion of the panel and have thickness equal to the one of the panel.

In order to provide a deeper insight on how the dimension, surface area and thickness, of the piezoelectric transducers influence the response of the structure, four cases are taken into consideration: (1) small and thin transducers, (2) small and thick transducers, (3) large and thin transducers and (4) large and thick transducers. The dimensions for the four considered cases are presented in table 4.5. Figure 4.11 shows the spectra of the total flexural kinetic energy

Table 4.5.: Dimensions of the piezoelectric transducers for the plots presented in figure 4.11.

Case	Figure	Type of patches	Surface area A_{pe}/A_p	Thickness h_{pe}/h_p
1	(a)	Small and thin	1%	30%
2	(b)	Small and thick	1%	30%
3	(c)	Large and thin	64%	90%
4	(d)	Large and thick	64%	90%

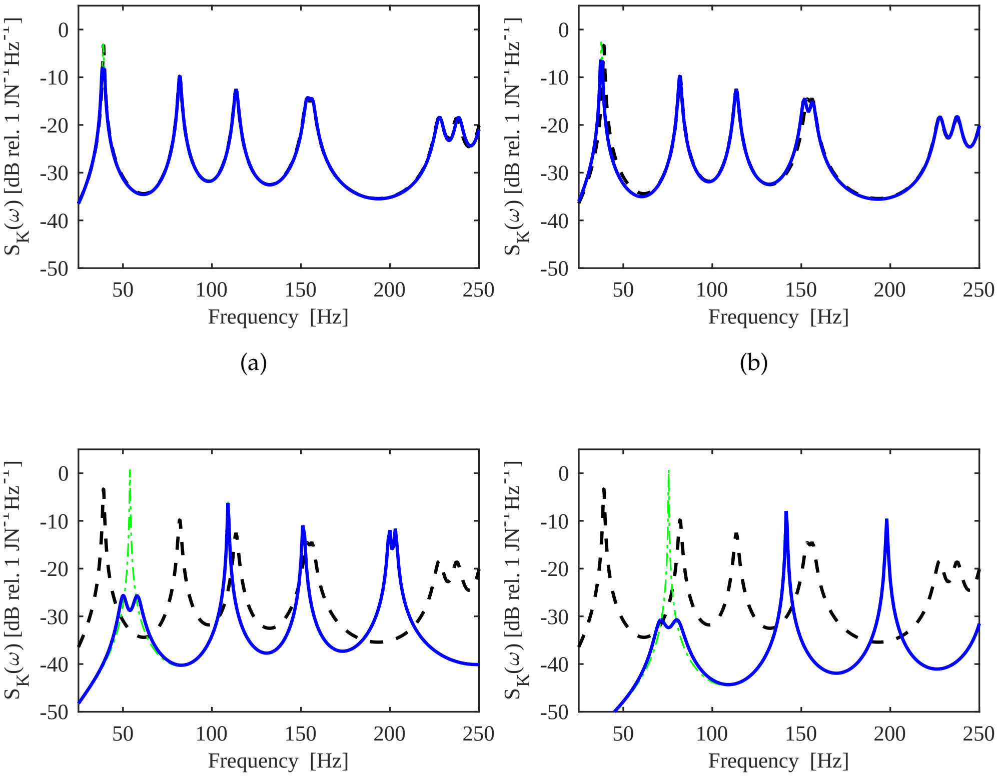

(a) (b)

(c) (d)

Figure 4.11.: PSD of the total flexural kinetic energy of the plate without the piezoelectric transducers (dashed thick black line) and with them in short circuit (dash-dotted thin green line) and connected to a properly tuned RL shunt (thick solid blue line) for four different patch dimensions as described in table 4.5.

PSD of the plain panel (thick dashed black line) and of the panel with the piezoelectric transducers either in short circuit (thin dash-dotted green line) or connected to the optimal RL shunt (thick solid blue line) in the 30-250 Hz frequency band for all four analysed cases. Plots (a) and (b) indicate that if the transducers are small, regardless of whether they are thin or thick, the shunted piezoelectric vibration absorbers have little impact on the flexural response of the panel and produce a reduction of around 3-4 dB of the amplitude of the first resonance peak. In contrast, plots (c) and (d) show that large transducers produce a substantial variation of the dynamic response. More specifically, the dash-dotted green line in plot (c) shows that, for the vibration absorber composed of the large and thin patches, the spectrum of the response is characterised by a shift to higher frequencies of the resonance peaks. In other words, the transducers produce on the panel a higher stiffening effect than the inertial effect. Also, the solid blue line in plot (c) shows that the shunt successfully reduces the amplitude of the first resonance peak by about 25 dB for a pair of large and thin patches. Considering the large and thick patches, the thin dash-dotted green and the thick solid blue lines in plot (d) shows that the spectrum of the response is characterised by even a greater shift to higher frequencies of the resonance peaks and that the shunt effectively reduces the amplitude of the first resonance peak by more than 30 dB.

The four plots of figure 4.11 are useful to provide clear and enlightening insights on the parametric study presented in figure 4.10, which indicate how large and thin or large and thick piezoelectric patches produce the best combination of mechanical and electromechanical effects for the reduction of the flexural response of the fundamental natural mode of the panel at the first resonance frequency. The analysis presented in this section is limited to the control of the first natural mode of the panel, which is characterised by a volumetric mode shape that effectively couples to a patch that covers the whole surface of the panel [70]. It is likely that shaped piezoelectric patches should be used to effectively control higher order modes, as it happens with radiation modes [70]. Nevertheless, the transducers should be kept as large as possible to maximise the electromechanical coupling.

Another interesting thing to analyse is how the electrical parameters of the resonant circuit vary with the transducers dimensions considered in this study. Figure 4.12 shows the piezoelectric patches inherent capacitance; as it is for parallel plate capacitors, the patches inherent capacitance is directly proportional to the surface area of the patches and inversely proportional to the thickness of the patches. As it was discussed in section 4.3.3, the piezoelectric transducers capacitance determines the aperture, which relates directly to the maximum at-

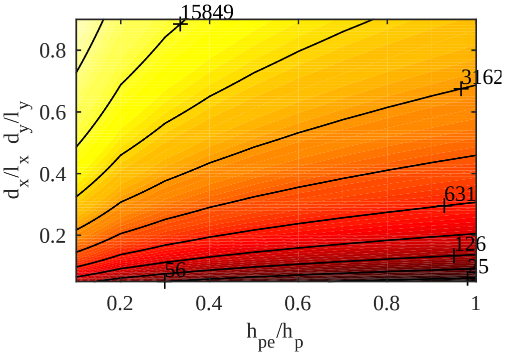

Figure 4.12.: Piezoelectric transducers inherent capacitance in pF for the considered surface area and thickness of the transducers.

tenuation, of the double resonance peak produced by the shunted piezoelectric vibration absorber in correspondence to the targeted resonance frequency of the panel. It is possible to affirm that when large piezoelectric transducers are used, the implementation of a negative capacitance effect in the shunt to reduce the inherent capacitance of the piezoelectric patch may significantly increase the vibration control effect produced by the shunted piezoelectric transducer vibration absorber.

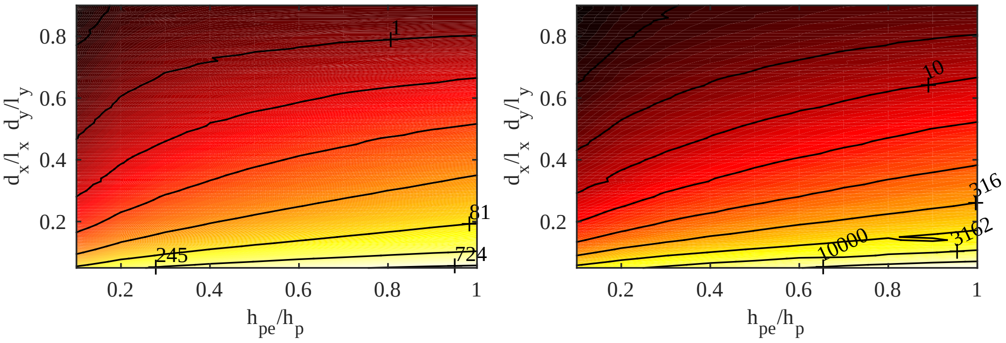

(a) (b)

Figure 4.13.: Optimal values for the shunt (a) inductance in H and (b) resistance in $k\Omega$ for the considered surface area and thickness of the transducers.

Figure 4.13 on the other hand, shows the variation of the optimal inductance and resistance values in plots (a) and (b) respectively. These plots show that both the inductance and resistance values tend to decrease as the transducers surface area increases and as the transducers thickness decreases. Thus, in general, it is preferable to use piezoelectric patches with the largest possible surface area and thickness similar to the one of the plate for the practical realisation of the shunt circuit.

4.5 CHAPTER CONCLUDING REMARKS

This chapter presented a theoretical study on shunted piezoelectric vibration absorbers bonded on a thin rectangular panel to control its flexural response at frequencies near a resonance frequency of the panel. A fully coupled electromechanical analytical model was presented, which was developed considering the classical laminated plate theory.

This study shows that the classical analytical formulae for the optimal tuning values of the RL shunt circuit based on simplified lumped parameters model are not adequate when the patches are bonded on two-dimensional distributed structures such as a thin plate. Two effects could explain this:

1. the high modal overlap factor that characterises thin structures, and
2. the fact that the coupling between the plate and the transducers is characterised by large self and cross mechanical and electromechanical modal coupling factors.

Finally, the last part of the chapter deals with a parametric study that gives general guidelines about how the surface and thickness dimensions of the piezoelectric transducers affect the performance of the vibration absorber system. To control the response near the first resonance frequency of the plate, the piezoelectric patches should be very large, covering most of the panel surface and a thickness equal to the one of the plate. The control of the flexural response near resonances at higher frequencies is expected to require large patches, but with specific shapes, maximising the electromechanical coupling effect of the targeted resonating mode.

5

TIME-VARYING SHUNTED PIEZOELECTRIC VIBRATION ABSORBERS

This chapter deals with a simulation study concerning the low and mid frequencies control of flexural vibration in a lightly damped thin plate, which is excited by a rain-on-the-roof broad band frequency stationary disturbance and equipped with time-varying shunted piezoelectric vibration absorbers. The study considers discrete or continuous variations over time of the RL shunts in such a way as to switch between given values or to sweep between given ranges the shunt parameters and in this way control the resonant response of certain targeted flexural modes or the flexural response of the plate due to all modes in the 20 Hz and 1 kHz frequency band. First a system considering a single vibration absorber unit is presented and then a system with five vibration absorbers.

Contents

5.1 INTRODUCTION

Recent studies have shown the possibility of controlling the flexural response of thin structures over a broad frequency band using time-varying mechanical vibration absorbers [64, 102, 103]. The working principle of this type of vibration absorbers is to vary the stiffness and damping parameters of the vibration absorber within given ranges to produce a control action over a desired frequency band. A voice coil transducer with the magnet suspended on soft springs was used to experimentally demonstrate this type of time-varying mechanical vibration absorber [102].

On the other hand, the use of shunted piezoelectric transducers to control mechanical vibrations was introduced in chapter 4. However, as a shunted piezoelectric patch connected to an RL shunt can control the resonant response of only one specific natural mode of the plate, multi-resonant circuits were investigated [32, 33, 104–109], in which the shunt is composed of n RL or RLC branches to control n natural modes of the plate. In this case the first branch is an RL shunt and the rest are RLC shunts; with each additional branch the values of the previous branches must be recalculated. No closed-form tuning solution was found for this technique, but the shunts values can be found numerically [18].

In this work, and as an alternative to the multi-resonant shunt circuits, the use of time-varying shunts is proposed. Two operation modes are presented: the first one in which the inductance and resistance of the shunt are cyclically switched between three values in order to control the flexural response of three natural modes of the plate; and the second, in which the shunt parameters are swept between given ranges to control the flexural response of all the natural modes of the plate in a given frequency band.

In this chapter the implementation of time-varying shunted piezoelectric vibration absorbers for broadband flexural vibration control is considered. As depicted in figure 5.1 the shunt is composed of a time-varying inductance and resistance. The same thin aluminium panel as in chapter 4 is considered here, with dimensions and physical properties summarised in table 4.1. On the other hand, in this study thin rectangular piezoelectric transducers are considered, whose dimensions and physical parameters are presented in table 5.1, and as shown in figure 5.1 the central patch is bonded on the backside of the plate. It must be noted that for the considered frequency range the membrane effect can be neglected. Finally, as shown in figure 5.2 the panel is exposed to a white

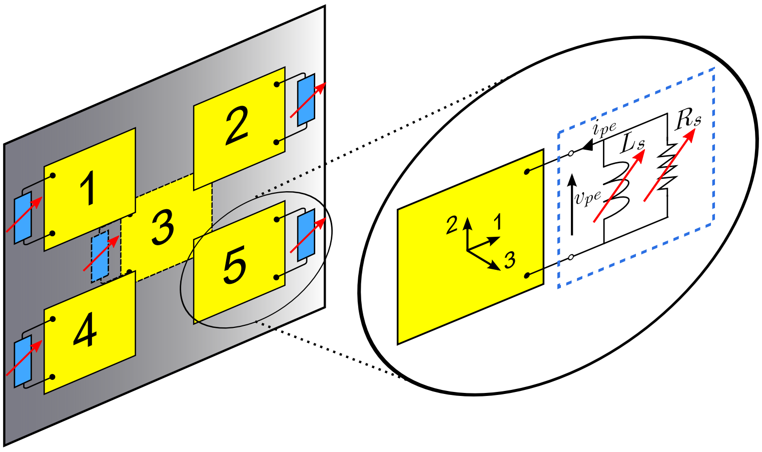

Figure 5.1.: Plate equipped with five shunted piezoelectric vibration absorbers implementing time-varying RL shunts.

noise rain-on-the-roof excitation, which is modelled by an array of 4×4 uncorrelated point forces uniformly distributed over the plate surface.

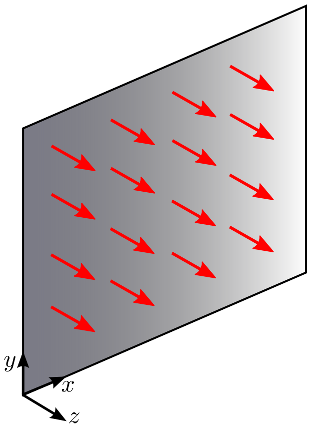

Figure 5.2.: Plate subject to a rain-on-the-roof excitation modelled using an array of 4×4 point forces.

First, a panel with only the top left piezoelectric vibration absorber will be analysed and then the five patches configuration will be considered. The vibration control performance produced by the time-varying piezoelectric vibration absorbers will be compared to the one produced by single and five fixed tuning shunted piezoelectric vibration absorbers.

5.2 MATHEMATICAL MODEL

The mathematical model used to obtain the electromechanical equations of motion for the flexural response of the panel with the piezoelectric transducers

Table 5.1.: Dimensions and physical properties of the piezoelectric transducers.

Parameter	Value	Units
Thickness	$h_{pe} = 1$	mm
Width	$d_x = 80$	mm
Length	$d_y = 80$	mm
Centre position	$x_{c3} = \frac{l_x}{2},\ y_{c3} = \frac{l_y}{2}$	mm
$j = 1, 2, 4, 5$	$x_{cj} = \frac{l_x}{2} \mp 60,\ y_{cj} = \frac{l_y}{2} \mp 60$	mm
Density	$\rho_{pe} = 7600$	kg/m^3
Young's Modulus	$Y_{pe} = 50 \times 10^9$	N/m^2
Poisson's ratio	$\nu_{pe} = 0.35$	—
Permittivity	$\varepsilon_{33}^T = 14.18 \times 10^{-9}$	F/m
Inherent capacitance	$C_{pe} = 55.6 \times 10^{-9}$	F
Strain/charge constants	$d_{31} = -190 \times 10^{-12}$	m/V
	$d_{32} = -190 \times 10^{-12}$	m/V
	$d_{36} \approx 0$	m/V

is quite similar to the one presented in chapter 4. Nevertheless, a numerical approach is used together with the state space formulation to integrate the equation of motion of this time-invariant system. The reason for this is that the stochastic nature of the primary forces acting on the plate and the time-varying behaviour of the shunt circuits cannot be addressed using the standard frequency domain formulation based on frequency dependent PSDs and transfer functions [99].

As the initial part of this formulation is the same as the one presented in chapter 4 for a pair of piezoelectric transducers forming a symmetric laminate around the mid-surface of the plate, this section presents a reduced version where the differences are highlighted. In summary, the same variational indicator as presented in equation (4.57) is used, but in this case the kinetic coenergy, the elastic potential energy, the electrical coenergy and the work done by non conservative actions are defined respectively by the following expressions [92]

$$T^* = \frac{1}{2}\int_{V_p} \rho_p \dot{w}^2 \, \mathrm{d}V_p + \frac{1}{2}\int_{V_{pe}} \rho_{pe} \dot{w}^2 \, \mathrm{d}V_{pe} \tag{5.1}$$

$$V = \frac{1}{2}\int_{V_p} \mathbf{S}^T \mathbf{T} \, \mathrm{d}V_p + \frac{1}{2}\int_{V_{pe}} \mathbf{S}^T \mathbf{T} \, \mathrm{d}V_{pe} \tag{5.2}$$

$$W_e^* = \frac{1}{2}\int_{V_{pe}} E_{pe} D_{pe} \, \mathrm{d}V_{pe} \tag{5.3}$$

$$W_{nc} = \sum_{i=1}^{N} f_{pi} w_i - \int_{A_p} \mu \dot{w} w \, \mathrm{d}A_p - q_{pe} v_{pe} \tag{5.4}$$

where f_{pj} are the point forces acting on the plate and q_{pe} are the charges on the piezoelectric patch. Following the same procedure as in chapter 4.2 it is possible to arrive to the following set of modal equations

$$\left[\mathbf{M}_p + \mathbf{M}_{pe}\right] \ddot{\mathbf{q}}(t) + \mathbf{C}_p \dot{\mathbf{q}}(t) + \left[\mathbf{K}_p + \mathbf{K}_{pe}\right] \mathbf{q}(t) + \boldsymbol{\Theta}_{pe} v_{pe}(t) = \boldsymbol{\Phi}_p \mathbf{f}_p(t) \tag{5.5}$$

$$-\boldsymbol{\Theta}_{pe}^T \mathbf{q}(t) + C_{pe} v_{pe}(t) = q_{pe}(t) \tag{5.6}$$

$$i_{pe}(t) = -\frac{1}{R_s} v_{pe}(t) - \frac{1}{L_s} \int v_{pe}(t) \mathrm{d}t \tag{5.7}$$

where q_{pe} is the total charge produced by the piezoelectric transducers, $\mathbf{M}_p$, $\mathbf{C}_p$, $\mathbf{K}_p$ are the modal mass, modal damping and modal stiffness matrix of the plate defined in equations (4.77), (4.78) and (4.79) respectively, $\mathbf{M}_{pe}$, $\mathbf{K}_{pe}$ and $\boldsymbol{\Theta}_{pe}$ are the modal mass, modal stiffness and modal electromechanical transduction coefficient of the piezoelectric patches, C_{pe} is the capacitance of the piezoelectric patch and $\boldsymbol{\Phi}$ is the vector with the modal amplitudes of the generalized primary forces. These matrices and vectors are defined as:

$$\mathbf{M}_{pe} = m_{pe} \int_{A_{pe}} \boldsymbol{\varphi}^T(x,y) \boldsymbol{\varphi}(x,y) \mathrm{d}A_{pe} \tag{5.8}$$

$$\mathbf{K}_{pe} = I_{pe} \int_{A_{pe}} \boldsymbol{\psi}^T(x,y) \mathbf{c}_{pe}^E \boldsymbol{\psi}(x,y) \mathrm{d}A_{pe} \tag{5.9}$$

$$\boldsymbol{\Theta}_{pe} = z_{pe} \int_{A_{pe}} \boldsymbol{\psi}^T(x,y) \mathbf{e}_{pe} \mathrm{d}A_{pe} \tag{5.10}$$

$$C_{pe} = \frac{\varepsilon_{pe}^S A_{pe}}{h_{pe}} \tag{5.11}$$

where $\mathbf{I}$ is an identity $R \times R$ matrix, ξ_p is the modal damping ratio assumed to be equal for all modes and defined in table 4.1, $\boldsymbol{\psi}(x,y)$ is defined in equation (4.85) and

$$\boldsymbol{\Phi}_p = \begin{bmatrix} \boldsymbol{\varphi}(x_1, y_1) \\ \vdots \\ \boldsymbol{\varphi}(x_{16}, y_{16}) \end{bmatrix}, \quad \mathbf{f}_p = \begin{bmatrix} f_{p1} \\ \vdots \\ f_{p16} \end{bmatrix} \tag{5.12}$$

where $f_{p1}, \dots, f_{p16}$ are the sixteen forces applied on the plate.

5.2.1 *State space formulation*

The set of differential electromechanical equations represented by equations (5.5), (5.6) and (5.7) can be casted in the following state space matrix formulation

$$\dot{\mathbf{x}}(t) = \mathbf{A}\mathbf{x}(t) + \mathbf{B}\mathbf{f}_p(t) \tag{5.13}$$

$$\dot{\mathbf{q}}(t) = \mathbf{C}\mathbf{x}(t) \tag{5.14}$$

where the state space vector is defined as

$$\mathbf{x}(t) = \begin{bmatrix} x_1(t) \\ x_2(t) \\ x_3(t) \\ x_4(t) \end{bmatrix} = \begin{bmatrix} \mathbf{q}(t) \\ \dot{\mathbf{q}}(t) \\ \int \mathbf{v}_{pe}(t)\mathrm{d}t \\ \mathbf{v}_{pe}(t) \end{bmatrix} \tag{5.15}$$

Equations (5.5), (5.6) can be rewritten as:

$$\mathbf{M}\ddot{\mathbf{q}}(t) + \mathbf{C}_p\dot{\mathbf{q}}(t) + \mathbf{K}\mathbf{q}(t) + \mathbf{\Theta}_{pe}v_{pe}(t) = \mathbf{\Phi}_p\mathbf{f}_p(t) \tag{5.16}$$

$$-\mathbf{\Theta}_{pe}^T\dot{\mathbf{q}}(t) + C_{pe}\dot{v}_{pe}(t) = i_{pe}(t) \tag{5.17}$$

where $\mathbf{M}$ is the sum of $\mathbf{M}_p$ and $\mathbf{M}_{pe}$ and $\mathbf{K}$ is the sum of $\mathbf{K}_p$ and $\mathbf{K}_{pe}$. Using the state variables defined in equation (5.15), equations (5.16), (5.17) and (5.7) can be expressed as

$$\mathbf{M}\dot{x}_2(t) + \mathbf{C}_p\dot{x}_1(t) + \mathbf{K}x_1(t) + \mathbf{\Theta}_{pe}\dot{x}_3(t) = \mathbf{\Phi}_p\mathbf{f}_p(t) \tag{5.18}$$

$$-\mathbf{\Theta}_{pe}^T x_2(t) + C_{pe}\dot{x}_4(t) = i_{pe}(t) \tag{5.19}$$

$$i_{pe}(t) = -\frac{1}{R_s}x_4(t) - \frac{1}{L_s}x_3(t) \tag{5.20}$$

Then, substituting equation (5.20) into (5.19) and solving for $\dot{x}_4(t)$ the following expression is obtained:

$$\dot{x}_4(t) = \frac{\mathbf{\Theta}_{pe}^T}{C_{pe}}\dot{\mathbf{q}}(t) - \frac{1}{L_s C_{pe}}\int v_{pe}(t)\mathrm{d}t - \frac{1}{R_s C_{pe}}v_{pe}(t) \tag{5.21}$$

Solving equation (5.16) for $\dot{x}_2(t)$

$$\dot{x}_2(t) = -\mathbf{M}^{-1}\mathbf{C}_p\dot{x}_1(t) - \mathbf{M}^{-1}\mathbf{K}x_1(t) - \mathbf{M}^{-1}\mathbf{\Theta}_{pe}\dot{x}_3(t) + \mathbf{M}^{-1}\mathbf{\Phi}_p\mathbf{f}_p(t) \tag{5.22}$$

Using the latter two equations and recalling that the values for $\dot{x}_1(t)$ and $\dot{x}_3(t)$ are stated in equation (5.15) it is possible to express equations (5.13) and (5.14) in matrix form as

$$\begin{bmatrix} \dot{x}_1(t) \\ \dot{x}_2(t) \\ \dot{x}_3(t) \\ \dot{x}_4(t) \end{bmatrix} = \begin{bmatrix} \mathbf{0} & \mathbf{I} & \mathbf{0} & \mathbf{0} \\ -\mathbf{M}^{-1}\mathbf{K} & -\mathbf{M}^{-1}\mathbf{C}_p & \mathbf{0} & \mathbf{M}^{-1}\mathbf{\Theta}_{pe} \\ \mathbf{0} & \mathbf{0} & 0 & 1 \\ \mathbf{0} & \frac{\mathbf{\Theta}_{pe}^T}{C_{pe}} & \frac{-1}{C_{pe}L_s} & \frac{-1}{C_{pe}R_s} \end{bmatrix} \begin{bmatrix} x_1(t) \\ x_2(t) \\ x_3(t) \\ x_4(t) \end{bmatrix} + \begin{bmatrix} \mathbf{0} \\ -\mathbf{M}^{-1}\mathbf{\Phi}_p \\ 0 \\ 0 \end{bmatrix} \mathbf{f}_p(t) \tag{5.23}$$

$$\dot{q}(t) = [\mathbf{0}, \mathbf{I}, 0, 0] \begin{bmatrix} x_1(t) \\ x_2(t) \\ x_3(t) \\ x_4(t) \end{bmatrix} \tag{5.24}$$

The state **A**, input **B** and output **C** matrices are defined as

$$\mathbf{A} = \begin{bmatrix} \mathbf{0}^{R\times R} & \mathbf{I}^{R\times R} & \mathbf{0}^{R\times 1} & \mathbf{0}^{R\times 1} \\ -\mathbf{M}^{-1}\mathbf{K} & -\mathbf{M}^{-1}\mathbf{C}_p & \mathbf{0}^{R\times 1} & \mathbf{M}^{-1}\mathbf{\Theta}_{pe} \\ \mathbf{0}^{1\times R} & \mathbf{0}^{1\times R} & 0 & 1 \\ \mathbf{0}^{1\times R} & \frac{\mathbf{\Theta}_{pe}^T}{C_{pe}} & \frac{-1}{C_{pe}L_s} & \frac{-1}{C_{pe}R_s} \end{bmatrix} \tag{5.25}$$

$$\mathbf{B} = \begin{bmatrix} \mathbf{0}^{R\times 1} \\ -\mathbf{M}^{-1}\mathbf{\Phi}_p \\ 0 \\ 0 \end{bmatrix} \tag{5.26}$$

$$\mathbf{C} = \left[\mathbf{0}^{R\times R}, \mathbf{I}^{R\times R}, 0, 0\right] \tag{5.27}$$

where the dimensions of the zeros and identity sub-matrices are indicated as superscripts for clarity. This state space representation is valid for the single patch configuration, while the matrices for the multiple patch systems can be obtained following the same approach. In this case, the state vector is defined as follows

$$\mathbf{x}(t) = \begin{bmatrix} x_1(t) \\ x_2(t) \\ x_3(t) \\ x_4(t) \\ x_5(t) \\ x_6(t) \\ x_7(t) \\ x_8(t) \\ x_9(t) \\ x_{10}(t) \\ x_{11}(t) \\ x_{12}(t) \end{bmatrix} = \begin{bmatrix} \mathbf{q}(t) \\ \dot{\mathbf{q}}(t) \\ \int \mathbf{v}_{pe1}(t)\mathrm{d}t \\ \mathbf{v}_{pe1}(t) \\ \int \mathbf{v}_{pe2}(t)\mathrm{d}t \\ \mathbf{v}_{pe2}(t) \\ \int \mathbf{v}_{pe3}(t)\mathrm{d}t \\ \mathbf{v}_{pe3}(t) \\ \int \mathbf{v}_{pe4}(t)\mathrm{d}t \\ \mathbf{v}_{pe4}(t) \\ \int \mathbf{v}_{pe5}(t)\mathrm{d}t \\ \mathbf{v}_{pe5}(t) \end{bmatrix} \tag{5.28}$$

And the state **A**, input **B** and output **C** matrices are defined as

$$\mathbf{A} = \begin{bmatrix} \mathbf{0}^{R\times R} & \mathbf{I}^{R\times R} & \mathbf{0}^{R\times 1} & \mathbf{0}^{R\times 1} & \mathbf{0}^{R\times 1} & \mathbf{0}^{R\times 1} & \mathbf{0}^{R\times 1} & \mathbf{0}^{R\times 1} & \mathbf{0}^{R\times 1} & \mathbf{0}^{R\times 1} & \mathbf{0}^{R\times 1} & \mathbf{0}^{R\times 1} \\ -\mathbf{M}^{-1}\mathbf{K} & -\mathbf{M}^{-1}\mathbf{C}_p & \mathbf{0}^{R\times 1} & \mathbf{M}^{-1}\boldsymbol{\Theta}_{pe1} & \mathbf{0}^{R\times 1} & \mathbf{M}^{-1}\boldsymbol{\Theta}_{pe2} & \mathbf{0}^{R\times 1} & \mathbf{M}^{-1}\boldsymbol{\Theta}_{pe3} & \mathbf{0}^{R\times 1} & \mathbf{M}^{-1}\boldsymbol{\Theta}_{pe4} & \mathbf{0}^{R\times 1} & \mathbf{M}^{-1}\boldsymbol{\Theta}_{pe5} \\ \mathbf{0}^{1\times R} & \mathbf{0}^{1\times R} & 0 & 1 & 0 & 0 & 0 & 0 & 0 & 0 & 0 & 0 \\ \mathbf{0}^{1\times R} & \frac{\boldsymbol{\Theta}_{pe1}^T}{C_{pe}} & \frac{-1}{C_{pe}L_{s1}} & \frac{-1}{C_{pe}R_{s1}} & 0 & 0 & 0 & 0 & 0 & 0 & 0 & 0 \\ \mathbf{0}^{1\times R} & \mathbf{0}^{1\times R} & 0 & 0 & 0 & 1 & 0 & 0 & 0 & 0 & 0 & 0 \\ \mathbf{0}^{1\times R} & \frac{\boldsymbol{\Theta}_{pe2}^T}{C_{pe}} & 0 & 0 & \frac{-1}{C_{pe}L_{s2}} & \frac{-1}{C_{pe}R_{s2}} & 0 & 0 & 0 & 0 & 0 & 0 \\ \mathbf{0}^{1\times R} & \mathbf{0}^{1\times R} & 0 & 0 & 0 & 0 & 0 & 1 & 0 & 0 & 0 & 0 \\ \mathbf{0}^{1\times R} & \frac{\boldsymbol{\Theta}_{pe3}^T}{C_{pe}} & 0 & 0 & 0 & 0 & \frac{-1}{C_{pe}L_{s3}} & \frac{-1}{C_{pe}R_{s3}} & 0 & 0 & 0 & 0 \\ \mathbf{0}^{1\times R} & \mathbf{0}^{1\times R} & 0 & 0 & 0 & 0 & 0 & 0 & 0 & 1 & 0 & 0 \\ \mathbf{0}^{1\times R} & \frac{\boldsymbol{\Theta}_{pe4}^T}{C_{pe}} & 0 & 0 & 0 & 0 & 0 & 0 & \frac{-1}{C_{pe}L_{s4}} & \frac{-1}{C_{pe}R_{s4}} & 0 & 0 \\ \mathbf{0}^{1\times R} & \mathbf{0}^{1\times R} & 0 & 0 & 0 & 0 & 0 & 0 & 0 & 0 & 0 & 1 \\ \mathbf{0}^{1\times R} & \frac{\boldsymbol{\Theta}_{pe5}^T}{C_{pe}} & 0 & 0 & 0 & 0 & 0 & 0 & 0 & 0 & \frac{-1}{C_{pe}L_{s5}} & \frac{-1}{C_{pe}R_{s5}} \end{bmatrix} \tag{5.29}$$

$$\mathbf{B} = \left[\mathbf{0}^{1\times R}, -\boldsymbol{\Phi}_p^T\mathbf{M}^{-1}, \mathbf{0}^{1\times 10}\right]^T \tag{5.30}$$

$$\mathbf{C} = \left[\mathbf{0}^{R\times R}, \mathbf{I}^{R\times R}, \mathbf{0}^{\times 10}\right] \tag{5.31}$$

5.2.2 *Numerical integration of stochastic differential equations*

The time integration of the equation of motion is performed considering the spectral analysis for cyclostationary processes [96] and implementing a specific Runge-Kutta algorithm developed by Kasdin [110]. The following two assumptions are made: the primary disturbances are treated as uncorrelated white noise and the shunted piezoelectric vibration absorbers as time-varying components, allowing the cyclic change of the inductance and resistance values.

The method proposed by Kasdin [110] does not require the explicit calculation of the derivatives of the function, instead it calculates an approximated solution at each time step. It is worth mentioning that commercially available functions use variable time step according to a certain tolerance value. This is not so when dealing with random processes as it is not possible to calculate an approximated error at each step, that is why a fixed time step is used. Then, for stochastic disturbances the differential equation (5.13) can be expressed as

$$\dot{\mathbf{x}}(t) = f_1(\mathbf{x}, t) + \mathbf{B}\mathbf{f}_p(t) \tag{5.32}$$

where the first term accounts for the deterministic dependence of $\mathbf{x}$ and t while the second one for the stochastic dependence of the disturbance. The approximated solution of equation (5.13) at time t_{k+1} can be defined as [110]

$$\mathbf{x}_{k+1} = \mathbf{x}_k + \alpha_1 k_1 + \alpha_2 k_2 + \cdots + \alpha_n k_n \tag{5.33}$$

with

$$k_1 = g f_1(\mathbf{x}_k, t_k) + h\mathbf{B}\mathbf{f}_{p1} \tag{5.34}$$

$$k_j = g f_1(\mathbf{x}_k + \sum_{i=0}^{j-1} \sigma_{ij}\mathbf{k}_i \ , \ t_k + \eta_j g) + g\mathbf{B}\mathbf{f}_{pj} \tag{5.35}$$

where $\mathbf{f}_{pj}$ is a vector of random forces generated at each time step. In order for the numerical solution $\mathbf{x}_k$ to have the same statistical properties than the exact solution $\mathbf{x}(t)$, the coefficients α_i, σ_{ij} and η_j are determined by matching the coefficients of the Taylor expansion of the covariance matrix of the exact solution $\mathbf{x}(t)$ and the approximated one $\mathbf{x}_k$. The values of these three coefficients for the fourth order Runge-Kutta algorithm used in this study can be found in [110]. In the implementation a time vector of 60 seconds is considered with a fixed sampling frequency of 20 kHz; in other words a fixed time step with a length of 50 microseconds. At each time step, the algorithm calculates the approximated solution, updates the value of the state matrix $\mathbf{A}$ and continues using as initial condition the state vector of the previous iteration.

5.2.3 *Energy formulation*

As in section 4.2.6 of the previous chapter, once that the time response of the plate flexural vibration is obtained, a frequency domain formulation is derived as noise and vibration problems subject to stationary random disturbances are usually studied in the frequency domain. The flexural response of the plate with the piezoelectric transducers is studied in terms of the panel total flexural kinetic energy PSD, which as shown in [12] can be derived with the following expression [95, 96]

$$\begin{aligned} S_K(\omega) = & \frac{1}{2} \int_{A_p} \rho_p h_p \lim_{T \to \infty} \left[\frac{1}{T} \dot{w}^*(x, y, \omega) \dot{w}(x, y, \omega) \right] dA_p \\ & + \frac{1}{2} \int_{A_{pe}} \rho_{pe} h_p \lim_{T \to \infty} \left[\frac{1}{T} \dot{w}^*(x, y, \omega) \dot{w}(x, y, \omega) \right] dA_{pe} \end{aligned} \tag{5.36}$$

Equation (5.36) is very similar to (4.109), and the procedure is the same as in section 4.2.6, therefore a reduced formulation is presented here. Equation (5.36) can be expressed as

$$S_K(\omega) = \frac{1}{2} Tr \left[\mathbf{M} \mathbf{S}_{\mathbf{qq}}(\omega) \right] \tag{5.37}$$

where for a linear and time invariant system the matrix $\mathbf{S}_{\mathbf{qq}}(\omega)$ containing the PSDs of the plate modal velocities can be defined as

$$\mathbf{S}_{\mathbf{qq}}(\omega) = \mathbf{Y}(\omega) \mathbf{S}_{\mathbf{f}_p \mathbf{f}_p} \mathbf{Y}^T(\omega) \tag{5.38}$$

where the mobility matrix $\mathbf{Y}(\omega)$ is defined as

$$\mathbf{Y}(\omega) = j\omega \left[-\omega^2 \mathbf{M} + j\omega \left(\mathbf{C} + Z_{spe} \mathbf{\Pi} \right) + \mathbf{K} \right]^{-1} \tag{5.39}$$

and where the matrix $\mathbf{S}_{\mathbf{f}_p \mathbf{f}_p}$ contains the PSD functions of the 16 uncorrelated white noise forces acting on the panel and is given by a 16×16 identity matrix. Substituting equation (5.38) into (5.37) gives the total flexural kinetic energy PSD

$$S_K(\omega) = \frac{1}{2} Tr \left[\mathbf{M} \mathbf{Y}(\omega) \mathbf{S}_{\mathbf{f}_p \mathbf{f}_p} \mathbf{Y}^T(\omega) \right] \tag{5.40}$$

When the time-varying shunted vibration absorbers are used the time history of the total flexural kinetic energy is not anymore stationary and therefore the total flexural kinetic energy PSD cannot be defined [95, 96]. However, both the switching and sweeping operation modes can be classified as cyclostationary allowing a Fourier transform analysis to estimate the kinetic energy PSD in the frequency domain [111].

The total flexural kinetic energy PSD is not derived from equation (5.40); instead, once the vector $\dot{\mathbf{q}}(t)$ is obtained using the numerical integration algorithm presented in section 5.2.2, its finite Fourier transform $\dot{\mathbf{q}}(\omega)$ is calculated and then substituted in equation (5.37). To prove the validity of this approach, figure 5.3 shows the spectrum of the total flexural kinetic energy PSD of the plate in steady state condition obtained following the above description (thick solid red line) and calculated using equation (5.37) (thin black solid line). The curves match quite well, there is only some difference at the first natural frequency at around 38 Hz, where the response calculated via the finite Fourier transform of the instantaneous total kinetic energy of the panel is somewhat underestimated. Nevertheless, this was found to be the best trade-off between the random error present in the signal and the underestimation of the peaks [96]. The thick solid red line is obtained using MATLAB® *pwelch* function, whose output is the PSD estimate of the input signal, and whose parameters with the values used in this study are:

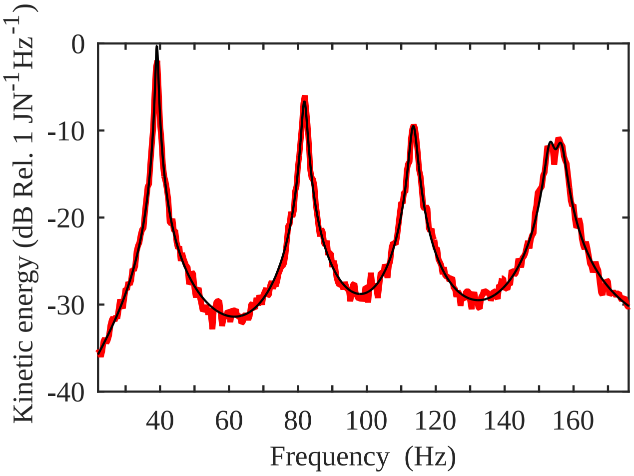

Figure 5.3.: Total flexural kinetic energy PSD of the plain plate obtained using equation (5.37) (thin solid black line) and using the numerical approach (thick solid red line).

window: divides the input signal vector in sub-vectors, this study considered windows of 50000 samples which means windows with a length of 2.5 seconds;

noverlap: specifies the overlap in samples, set to 50%;

nfft: sets the number of DFT points, also 50000 samples were considered which gives a resolution of 0.05 Hz for the output vector;

fs: indicates the sampling frequency of the input time vector, set to 20 kHz.

5.3 SINGLE PATCH SYSTEMS

In this section only the top left shunted piezoelectric transducer shown in figure 5.1 is considered. The vibration control effects are analysed considering the piezoelectric patch is connected to a time-invariant fixed shunt, to a time-varying switching shunt and to a time-varying sweeping shunt. As summarised in table 5.2, the fixed shunt is tuned to control the flexural response of the plate first natural mode, which resonates at 38 Hz. Instead, the switching shunt is tuned to iteratively control the resonant response of the plate first three flexural natural modes, which are located at around 38, 81 and 114 Hz. And the sweeping shunt is set to control the resonant response of the plate between 38 and 114 Hz.

Table 5.2.: Single patch systems control range.

Shunt type	Target frequency [Hz]
Fixed shunt	38
Switching	38, 81 and 114
Sweeping	38 to 114

One of the issues with shunted piezoelectric vibration absorbers is their proper tuning, as discussed in chapter 4, it is then interesting to analyse their effect when the shunt is not accurately tuned to the target frequency. Then, the system will also be studied when a shunt with a mistuning of 25% of the optimal inductance and resistance is implemented.

5.3.1 *Fixed tuning shunt*

The optimal resistive and inductive components of the shunt have been derived with a trial and error procedure, starting from the values obtained with equations (4.127) and (4.129) derived in the previous chapter. Figure 5.4 presents the spectrum of the total flexural kinetic energy PSD of the plate with the transducer N°1 in short circuit (thin solid black lines) in the 22-176 Hz frequency band. This spectrum is characterised by a series of five peaks due to the res-

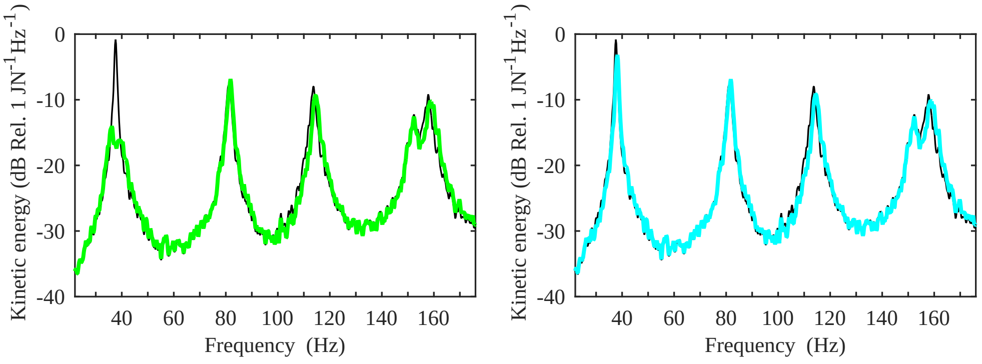

(a)

(b)

Figure 5.4.: PSD of the total flexural kinetic energy of the plate with the piezoelectric transducer N°1 in short circuit (thin solid black line) and connected to (a) an optimally tuned RL shunt (thick solid green line) and (b) to a mistuned RL shunt (thick solid cyan line) by 25% of the optimal inductance and resistance values.

onances of the panel low order natural modes, with the last two peaks being apart only 5 Hz distant from each other. Figure 5.4a shows the spectrum of the total flexural kinetic energy PSD of the plate with the piezoelectric transducer connected to an optimally tuned RL shunt (thick solid green line) set to control the resonant response of the first flexural mode of the plate. The spectrum is characterised by a large reduction of about 13.5 dB of the first resonance peak produced by the shunted piezoelectric vibration absorber. On the other hand, figure 5.4b presents the spectrum of the flexural response of the system when the shunt inductance and resistance values are mistuned by 25% (thick solid cyan line) with respect to their optimal values. In this condition the mistuned piezoelectric shunted vibration absorber has little impact on the response of the panel, achieving about 2 dB reduction at the target frequency, and as the accurately tuned it lightly enhances the response near the second resonance peak and produces around 1 dB reduction at the third resonance peak.

5.3.2 *Switching shunt*

In this operation mode the piezoelectric vibration absorber is equipped with a control algorithm that switches the shunt inductance and resistance between three pair of tuning values to control sequentially the resonant response of the first three flexural modes of the plate. As it was done for the fixed tuning shunt, the three pairs of RL values have been derived iteratively starting from

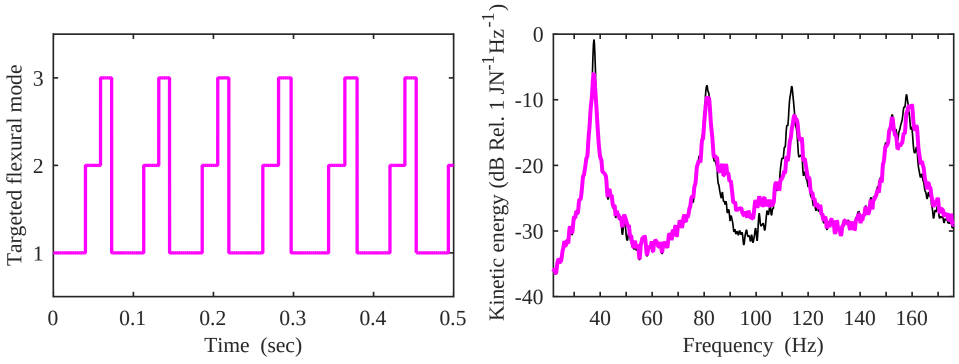

(a) (b)

Figure 5.5.: (a) Time history of the switching sequence and (b) PSD of the total flexural kinetic energy of the plate with the piezoelectric transducer N°1 in short circuit (thin solid black line) and connected to an RL switching shunt tuned to the first three resonant frequencies (thick solid magenta line).

equations (4.127) and (4.129) for each of the three targeted modes. To allow smooth transitions between consecutive states, the switching events occur only when the piezoelectric patch is not strained, that is when the voltage across its terminals is equal to zero.

The free response of the shunt circuit is characterised by an exponential decay defined by the time constant

$$\tau_n' = \frac{1}{\zeta_{s,n}\omega_{s,n}} \tag{5.41}$$

where $\zeta_{s,n}$ and $\omega_{s,n}$ are respectively the damping ratio and natural frequency of the electric circuit formed by the piezoelectric patch capacitance and RL elements of the shunt set to control the resonant response of the n-th flexural mode of the plate; recalling that for an RLC parallel circuit the damping ratio and natural frequency are defined as:

$$\zeta_{RLC} = \frac{1}{2R}\sqrt{\frac{L}{C}} \tag{5.42}$$

$$\omega_{RLC} = \sqrt{\frac{1}{LC}} \tag{5.43}$$

Then, in order to allow at least 63% of the transient occurs at each iteration, the duration of each tuning configuration is set to be

$$\tau_n = \tau_n' + \Delta t \tag{5.44}$$

where Δt represents the fraction of time necessary to reach the zero strain condition to implement a smooth transition from one tuning to the next one. Table 5.3 shows the set of values for the inductance, resistance and τ for each of the targeted flexural modes. In summary, to control the resonant response of the first three natural modes of the plate, the following switching sequence has been implemented: $\tau_1 + \Delta t$, $\tau_2 + \Delta t$, $\tau_3 + \Delta t$. Plot (a) of figure 5.5a shows a brief portion of the time history of the variable that controls to which flexural mode the shunt is tuned to at a particular instant, with time in the horizontal axis and the targeted flexural modes in the vertical axis.

Table 5.3.: Switching shunt control parameters.

Flexural mode	Inductance [H]	Resistance [kΩ]	τ_n [milliseconds]
1	181.9	357.3	$39.8 + \Delta t$
2	39.1	165.6	$18.4 + \Delta t$
3	20.6	120.2	$13.4 + \Delta t$

Following the same approach as in the previous subsection, the thin solid black line in figure 5.5b shows the 22–176 Hz spectrum of the total flexural kinetic energy PSD of the plate with the piezoelectric patch N°1 in short circuit. The thick solid cyan line in figure 5.5b shows the spectrum of the total flexural kinetic energy PSD of the plate with the piezoelectric patch N°1 connected to the switching RL shunt, which is characterised by a reduction of about 5.2 dB of the first resonance peak and about 1.8 dB and 4.5 dB reductions at the 2nd and 3rd resonances. The switching operation mode still produce a good vibration control effect at the first resonance accompanied by a good reduction at the third resonance and lower level performance at the second one. It is important to emphasise that this result depends also on the coupling between the piezoelectric patch and the controlled modes; which means that it is likely that the lower control effects produced at the 2nd and 3rd resonance frequencies could be ascribed also to a worst coupling between the patch and the 2nd and 3rd natural modes of the plate. Nevertheless, this initial result suggests that the single piezoelectric patch with the proposed switching shunt is able to produce an overall reduction of the resonating response of the three targeted flexural modes of the hosting plate.

5.3.3 *Sweeping shunt*

No specific tuning of the RL shunt elements is required for the sweeping operation mode. Instead, in this operation mode the shunt natural frequency is swept between the lower and upper limits of the frequency control range according to the following law:

$$\omega_s = \omega_i + (\omega_f - \omega_i) sin^2(2\pi f_{sw}) \tag{5.45}$$

where ω_i and ω_o are the lower and upper value of the targeted frequency band shown in table 5.2 and f_{sw} is the frequency is the sweeping frequency set to 6 Hz after a process of trial and error to find its optimal value. Figure 5.6a shows the variation over time of the RLC circuit natural frequency (thick red line), which has lower and upper limit values at around 40 Hz and 115 Hz respectively. The

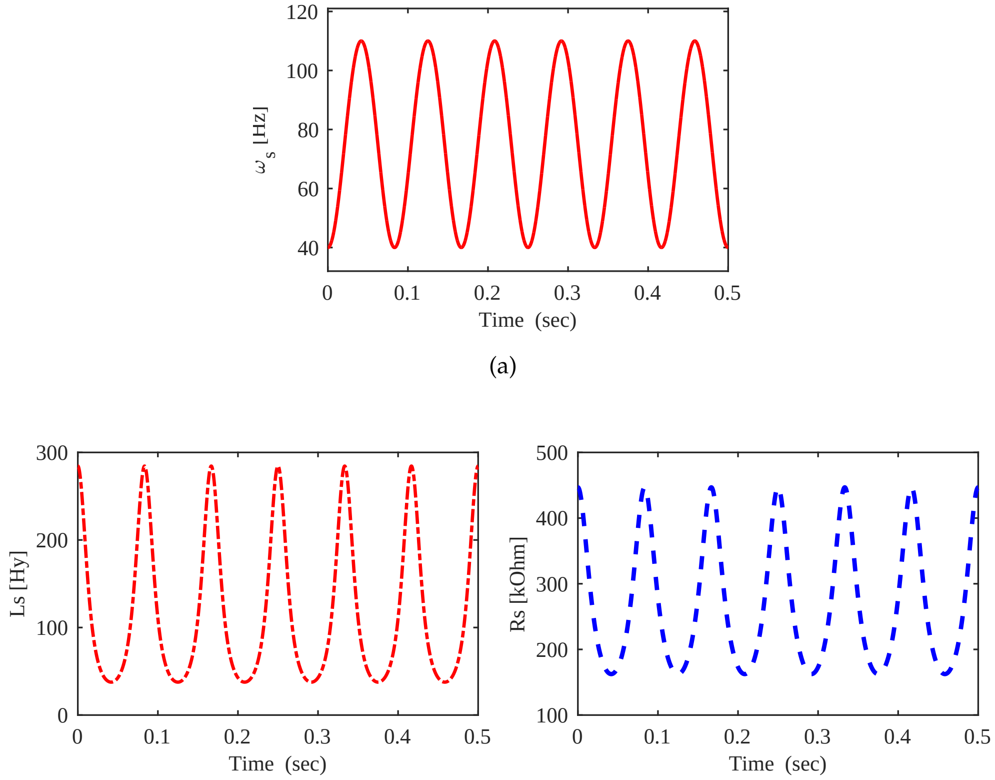

(a)

(b) (c)

Figure 5.6.: (a) Time history of the sweeping shunt resonance frequency and correspondent values for the sweeping shunt (b) inductance and (c) resistance in H and kΩ respectively.

inductance is obtained from equation (5.43) with the following expression:

$$L_s = \frac{1}{\omega_s^2 C_{pe}} \tag{5.46}$$

Also the shunt resistance is varied over time in such a way as to maintain a constant damping ratio equal to 30%, similar approach was used in references [64, 102, 112]. Then, using equation (5.42) the value of resistance is obtained as:

$$R_s = \frac{1}{2\zeta_s}\sqrt{\frac{L_s}{C_{pe}}} \tag{5.47}$$

Plots (b) and (c) of figure 5.6 show respectively the variation over time of the sweeping shunt inductance (dash-dotted red line) and resistance (dashed blue line). As the inductance has a quadratic relation with the shunt natural frequency, it can be noticed in plot (b) that the peaks are narrow and the function spends more time in the mid lower values than in the upper ones. The inductance value vary from a minimum of around 37 H to a maximum of about 285 H. Plot 5.6 shows a similar behaviour over time for the resistance, with minimum and maximum values of about 160 kΩ and 450 kΩ respectively.

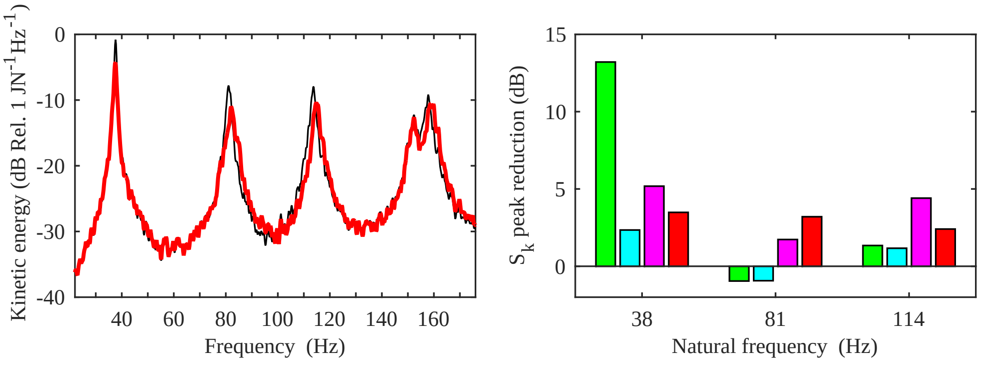

(a)

(b)

Figure 5.7.: (a) PSD of the total flexural kinetic energy of the plate with the piezoelectric transducer N°1 in short circuit (thin solid black line) and connected to an RL sweeping shunt set to control the 38-114 Hz frequency band (thick solid red line) and (b) total flexural kinetic energy PSD peak reduction for the first three resonance peaks of the system for all considered shunted piezoelectric vibration absorbers.

Following the same criteria as for the fixed tuning and switching shunts, the thin solid black line in figure 5.7a show the 22–176 Hz total flexural kinetic energy PSD spectrum of the plate with the piezoelectric transducer N°1 in short circuit. The thick solid red line, on the other hand, shows the spectrum of the total flexural kinetic energy PSD of the plate with the piezoelectric patch N°1 connected to the sweeping RL shunt. In this case, the spectrum is characterised by reductions of about 3.5 dB, 3.2 dB and 2.5 dB of the first three resonance peaks. Thus, despite the shunt is operated blindly without tuning the RL elements to precise natural frequencies and damping ratios of the plate natural modes comprised in the targeted frequency range, reasonable reductions of the resonance peaks are generated in the frequency range between 38 and 114 Hz. This is a rather interesting result since it suggest a simple operation mode of the shunt, which does not require prior knowledge of the dynamic response of the structure and, quite importantly, which is robust to changes of operation conditions that may vary the dynamic response of the hosting structure (tensioning effects, temperature variations, etc.).

Plot (b) in figure 5.7 summarises the results obtained with the four considered cases:

- fixed tuning shunt set to control the first natural frequency of the plate, first green column starting from the left-hand side;
- detuned fixed tuning shunt, second cyan column starting from the left-hand side;
- switching shunt set to control the first three natural frequencies of the plate, third magenta column starting from the left-hand side and
- sweeping shunt set to control the 38-114 frequency band, fourth red column starting from the left-hand side.

5.4 MULTIPLE PATCH SYSTEMS

The results obtained in the previous section with a single piezoelectric transducer indicate that the proposed time-varying shunts may be effectively used to control the flexural response of the plate in a broad frequency band. The effects produced by the five shunted piezoelectric vibration absorber shown in figure 5.1 are analysed in this section.

The five shunted piezoelectric vibration absorbers are operated in such a way as to control the flexural response of the plate in a relatively large frequency range comprised between 30 Hz to 1 kHz that encompass both the low-frequency range, where the response is characterised by the well separated narrow band resonance peaks, and the mid-frequency range, where the response is characterised by wide band crests and troughs due to the combined response

Table 5.4.: Multiple patch systems control frequencies or frequency bands.

Shunt type	Absorber 1	Absorber 2	Absorber 3	Absorber 4	Absorber 5
Fixed tuning	39 Hz	115 Hz	254 Hz	455 Hz	768 Hz
Switching series	39, 79, 115 Hz	156, 165, 233 Hz	165, 254, 431 Hz	455, 513, 569 Hz	698, 728, 769 Hz
Switching parallel	39, 79, 115, 156, 165, 233, 165, 254, 431, 455, 513, 569, 698, 728 and 768 Hz				
Sweeping series	30 to 100 Hz	80 to 230 Hz	210 to 440 Hz	400 to 670 Hz	670 to 1000 Hz
Sweeping parallel	from 30 Hz to 1000 Hz with a phase shift of $pi/5$ between consecutive piezoelectric vibration absorbers				

of clusters of modes [70]. The performance achieved by five fixed shunts set to control the resonant response of the flexural modes with natural frequencies listed in the first row of table 5.4 is used as a benchmark result to assess the effectiveness of switching and sweeping operation modes.

The targeted natural frequencies for the fixed tuning shunt have been chosen in such a way as to divide the total frequency band in five sub-bands covering the 30 Hz to 1 kHz frequency range and each vibration absorber is acting on one of these five sub-bands. Also in this study a mistuned fixed shunt is included in the analysis. Furthermore, two operation modes are defined for the time-varying shunts: A *Series mode* in which each vibration absorber acts on one of the previously discussed sub-bands, and a *Parallel mode* in which the five vibration absorbers are acting on the whole control frequency band asynchronously, with a phase shift of $pi/5$ between each other. Table 5.4 also summarises either the targeted frequencies or frequency bands for the series/parallel switching and sweeping operation modes. The frequency bands for the series sweeping mode are characterised by an overlap of 20 to 50 Hz.

5.4.1 *Fixed tuning shunt*

The optimal resistive and inductive elements of the five shunts have been derived following the same approach as for the single vibration absorbers systems in section 5.3.1, i.e. with a trial and error procedure using the values obtained with equations (4.127) and (4.129) as starting point, for the five flexural modes with natural frequencies listed in the first row of table 5.4.

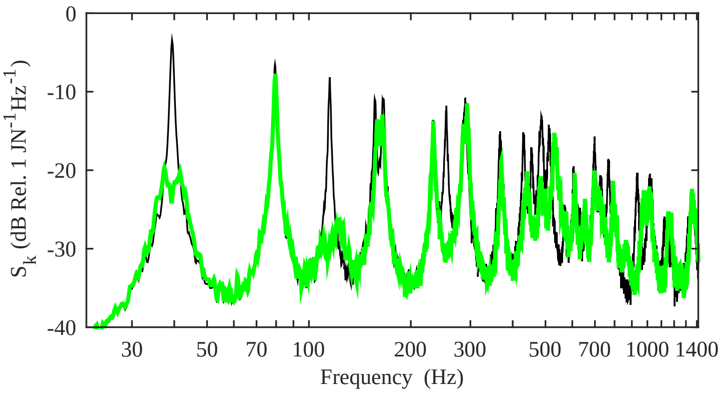

(a) Optimally tuned fixed RL shunts.

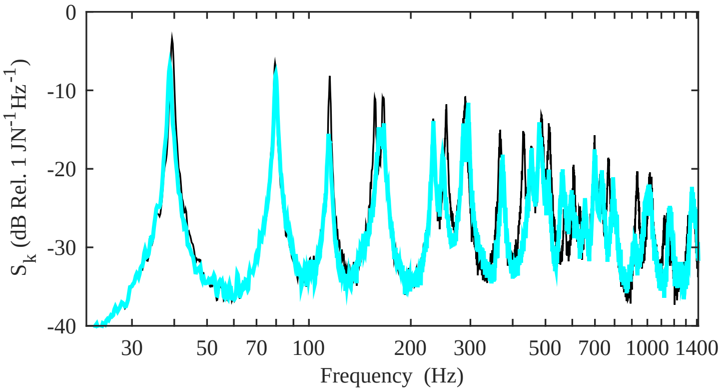

(b) Mistuned fixed RL shunts.

Figure 5.8.: PSD of the total flexural kinetic energy of the plate with the five piezoelectric transducers in short circuit (thin solid black line) and connected to fixed RL shunts (a) optimally tuned (thick solid green line) to the resonance frequencies as specified in table 5.4 and (b) mistuned (thick solid cyan line) 25% of the optimal inductance and resistance values.

The thin solid black line in both plots of figure 5.8 shows the 22–1414 Hz spectrum of the total flexural kinetic energy PSD of the plate with the five piezoelectric patches in short circuit. The spectrum is characterized by a series of well separated and sharp resonance peaks up to about 400 Hz. At higher frequencies, at each frequency the response is controlled by the resonant response of clusters of modes, which give rise to a sequence of crests and troughs. The thick solid green line in figure 5.8a shows the spectrum of the total flexural kinetic energy PSD of the plate with the piezoelectric patches connected to the optimal fixed RL shunts. The spectrum is characterised by large reductions comprised between 10 dB and 18 dB of the peaks produced by the resonant responses of the five targeted flexural modes. As expected, the fixed tuning produce large vibration control effects, which however are limited to the resonance frequencies of the targeted flexural modes.

Figure 5.8b shows the effect of using mistuned RL shunts; as for the single patch system, the shunt inductance and resistance are mistuned by 25% of their optimal values. The thick solid cyan line in plot (b) of figure 5.8 indicates that there is little impact on the global response of the structure when the shunts are mistuned. Although there are a few resonance peaks in which the mistuned system is able to achieve a reduction of the flexural response amplitude in the order of 3-8 dB. This is probably due to the fact that a shunt that is not properly tuned to control a particular frequency could be tuned to a different one.

5.4.2 *Switching shunt*

The series and parallel switching operation modes are implemented using control algorithms that switch sequentially the RL elements to the optimal values for the control of the resonant responses of the flexural modes with natural frequencies listed in rows 2 and 3 of table 5.4. Following the same strategy as in Section 5.3.2, the switching sequences are implemented in such a way as to ensure a decay of at least 63% of the response of the targeted modes at each iteration. The duration of each tuning configuration is defined by equations (5.41), (5.42) and (5.44). As for the single vibration absorber of Section 5.3.2, to allow smooth transitions between the RL values, the switching events are implemented only when the piezoelectric patches are not strained, i.e when the voltage across their terminals are zero. Then, the duration of each tuning configuration is set to be $\tau + \Delta t$, where Δt represents the fraction of time necessary to reach the zero strain condition essential to implement a smooth transition from one tuning to the next one.

Table 5.5.: Series switching time constants.

τ [ms]	Absorber 1	Absorber 2	Absorber 3	Absorber 4	Absorber 5
$\tau_{1-5,1}$	30.8	7.6	7.4	5.3	1.1
$\tau_{1-5,2}$	15.3	7.4	4.8	2.4	1.1
$\tau_{1-5,3}$	10.6	17.4	2.4	2.8	1.6

Table 5.6.: Parallel switching time constants, bold numbers indicate the starting value for each vibration absorber.

τ [ms]	Absorber 1	Absorber 2	Absorber 3	Absorber 4	Absorber 5
τ_{1-15}	**7.4**, 4.8, 2.4, **7.6**, 7.4, 17.4, **30.8**, 15.3, 10.6, **5.32**, 2.4, 2.8, **1.1**, 1.1 and 1.6				

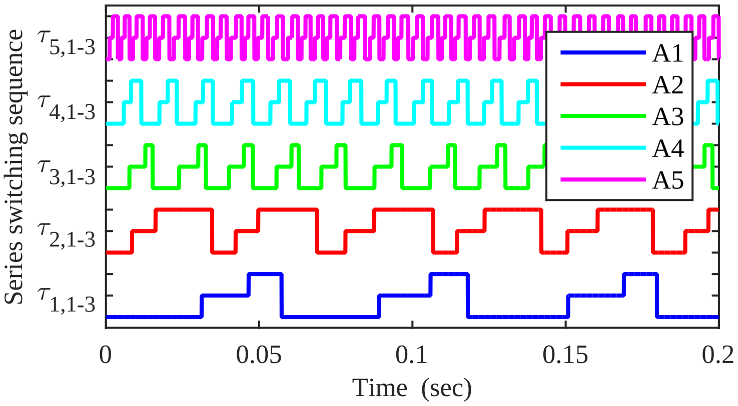

(a) Series switching sequence.

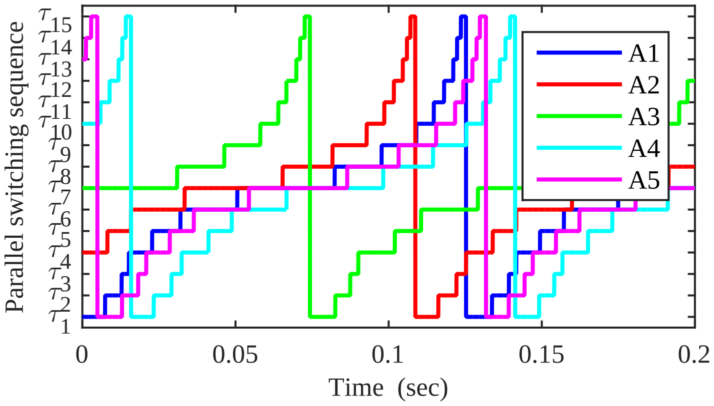

(b) Parallel switching sequence.

Figure 5.9.: Time history of the switching sequences for the (a) series and (b) parallel operation modes.

Table 5.5 shows the values for the switching time constants in milliseconds for each vibration absorber. It is important to mention that these values are not taking into account the extra time Δt to perform a smooth transition between consecutive tunings.

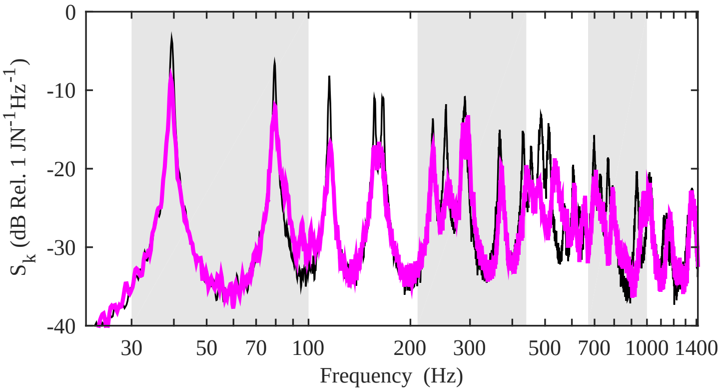

(a) Series switching.

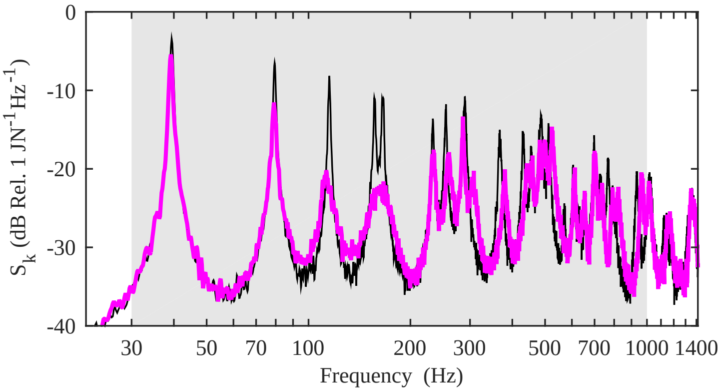

(b) Parallel switching.

Figure 5.10.: PSD of the total flexural kinetic energy of the plate with the five piezoelectric transducers in short circuit (thin solid black line) and connected to switching RL shunts (thick solid magenta line) operating in (a) series and (b) parallel mode tuned to the resonance frequencies as specified in table 5.4.

Figure 5.9 shows the switching sequence over time of both operation modes. Plot (a) presents the series mode switching sequence for all five vibration absorbers, where the legends A1 to A5 are used to respectively identify vibration absorbers N°1 to 5. It can be noticed that the time period of the vibration absorber N°1 (thick solid blue line) is much greater than the rest, with the N°2 (thick solid red line) being some 7 milliseconds faster, N°3 (thick solid green line) and N°4 (thick solid cyan line) having similar periods and N°5 (thick solid magenta line) period has a very brief duration of about 4 milliseconds. On the other hand, plot 5.9b shows the parallel mode switching sequence, the same colours as in plot 5.9a are used to identify each vibration absorber. In this operation mode all vibration absorbers are iteratively tuned to all 15 considered flexural modes as shown in table 5.4 and the switching time constants in milliseconds are presented in table 5.6 where the bold numbers indicate the starting configuration for each of the five vibration absorbers. Also in this case these values are neglecting the extra time Δt to perform a smooth transition between one set of RL values to the next one.

The thin solid black line in both plots of figure 5.10 show the 22–1414 Hz spectrum of the total flexural kinetic energy PSD of the plate with the five piezoelectric patches in short circuit, while the thick solid cyan lines in show the spectrum of the total flexural kinetic energy PSD of the plate when the five piezoelectric patches implement respectively the series and parallel switching operation modes. Stripes with darker colour has been added in the background of plot (a) to easily recognize the frequency ranges for each one of the five vibration absorber in the 30 to 1 kHz band, while for plot (b) as they all have the same control frequency band only one stripe has been used. The two plots show significant reductions of most resonance peaks comprised between 30 Hz and 1 kHz. The series mode is able to control the response of most flexural modes resonating in this frequency range. The parallel mode produces relatively lower control effects at the first resonance peak, but then produces remarkable control effects at higher frequencies, in particular between 100 and 200 Hz. Additional simulation results have shown that the low frequency control performance could be improved if the time interval for lower frequencies are increased, particularly the time set to control the flexural response at the first natural frequency of the plate.

5.4.3 *Sweeping shunt*

The series and parallel sweeping operation modes are implemented in such a way the shunts natural frequencies are swept between the lower and upper limits of the targeted frequency range, just as for the single vibration absorber system presented in section 5.3.3. For the series mode, the five shunts operate individually in a given frequency sub-band whose lower and upper frequency limits are summarised in table 5.4. The series control laws for the five sweeping piezoelectric vibration absorbers is then derived from equation (5.45) as follows:

$$\omega_{series,n} = \omega_{i,n} + (\omega_{f,n} - \omega_i) sin^2(2\pi f_{sw}) \tag{5.48}$$

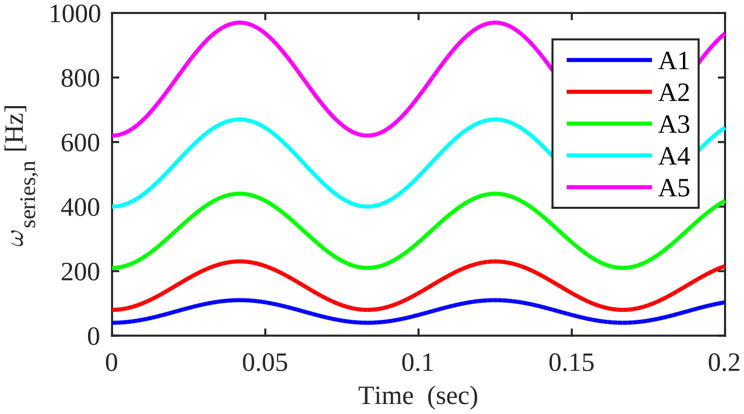

(a) Series sweeping.

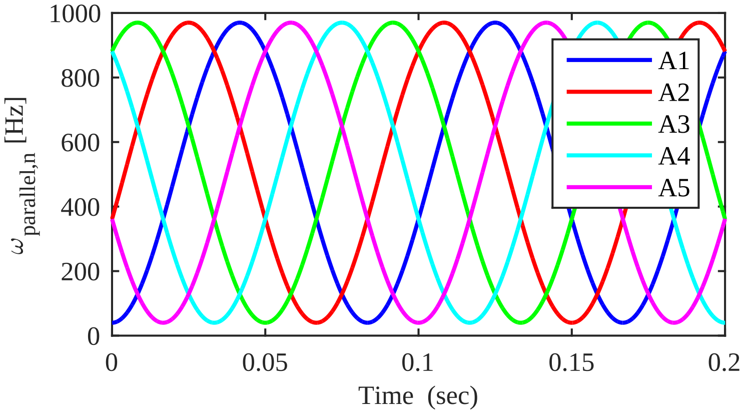

(b) Parallel sweeping.

Figure 5.11.: Time history of the sweeping shunts resonance frequencies for the (a) series and (b) parallel operation modes.

where $\omega_{i,n}$ and $\omega_{o,n}$ are the lower and upper value of each targeted frequency sub-band as shown in table 5.4 and f_{sw} is the sweeping frequency which, as for the single vibration absorber system, is set to 6 Hz. Figure 5.11a shows the variation over time of each RLC circuit natural frequency, same colours are used to identify each vibration absorber as in section 5.4.2. It is possible to notice the overlap between consecutive sweeping shunts and that as frequency rises the sweeping vibration absorbers cover a wider frequency band.

On the other hand, the expression for the control laws for the parallel operation mode, which is also derived from equation (5.45), are defined as:

$$\omega_{parallel,n} = \omega_i + (\omega_f - \omega_i) sin^2(2\pi f_{sw} + (n-1)\frac{\pi}{5}) \qquad (5.49)$$

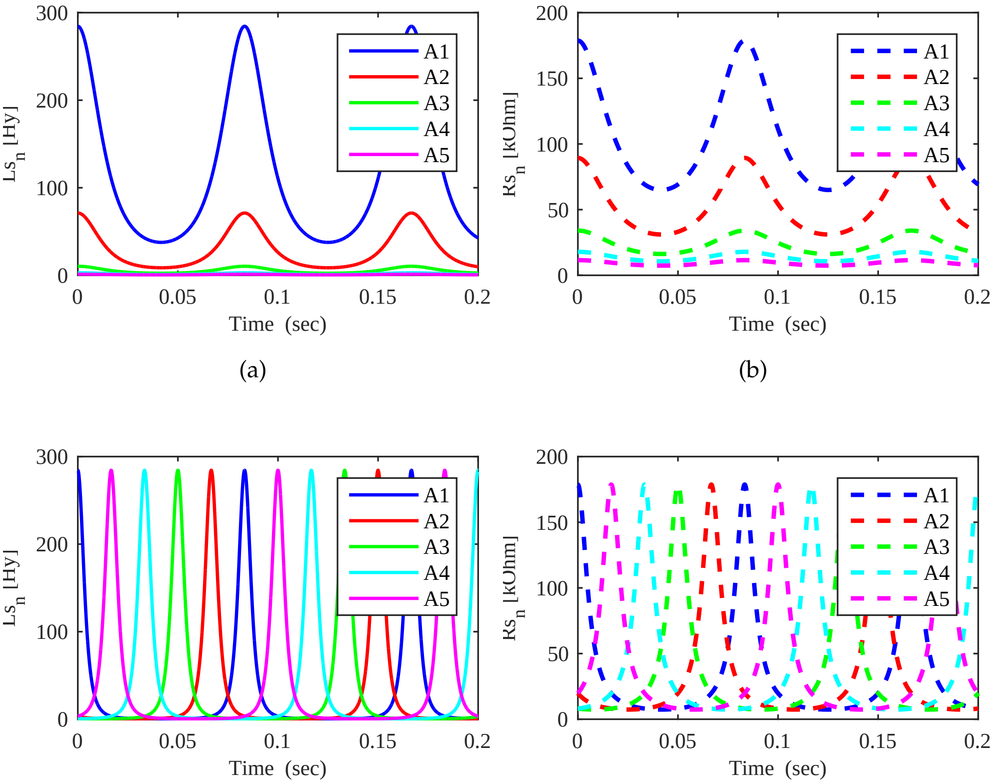

(a) (b) (c) (d)

Figure 5.12.: Evolution over time of the shunts inductance (plots (a) and (c)) and resistance (plots (b) and (d)) values for the series (plots (a) and (b)) and parallel (plots (c) and (d)) operation modes.

where ω_i and ω_o are the lower and upper value of the whole control frequency band as shown in table 5.4. Plot (b) of figure 5.11 shows the evolution over time of the control variables $\omega_{parallel,n}$. In this case it can be seen that the five sweeping vibration absorbers work on the same frequency band, and that the phase shift between consecutive vibration absorbers allows a uniform distribution of the control frequency band over time between the five sweeping vibration absorbers.

The values for each shunt inductance and resistance are obtained, for both series and parallel operation modes, using equations (5.43) and (5.42) with a damping coefficient ζ_s, which has a constant value of 20% for all five vibration absorbers and both operation modes. It is also interesting to analyse the evolution over time, presented in figure 5.12, of the shunts inductance and resistance values. Plots (a) and (b) show the values for the series operation mode of the shunt inductance and resistance respectively. It can be seen much longer ranges for the values corresponding to the vibration absorber N°1 for both shunt elements, with maximum values of about 290 H and 180 kΩ and minimum values of 35 H and 65 kΩ. For the vibration absorber N°2, the inductance is swept between around 9 to 72 H and the resistance between about 30 to 90 kΩ. Then, for vibration absorbers N°3, 4 and 5 the inductance has much shorter excursions, respectively from around 2.3 to 10 H, 1 to 2.8 H and 0.5 to 1.2 H. The same is valid for the resistance, with the following minimum and maximum values: 16 to 34 kΩ, 10 to 18 kΩ and 7 to 11.5 kΩ.

Considering the parallel operation mode, the shunt values are shown respectively in plots (c) and (d) of figure 5.12 for the inductance and resistance. As expected, the maximum and minimum values for the inductance are the same for all vibration absorbers as the only difference in the control law is the phase shift, with around 0.5 H as lower limit and 285 H as upper limit. The same is valid for the resistance in plot (d), with a minimum value of 7 kΩ and a maximum one of 180 kΩ.

The thin solid black line in both plots of figure 5.13 show the 22–1414 Hz spectrum of the total flexural kinetic energy PSD of the plate with the five piezoelectric transducers, illustrated in Section 5.2, in short circuit. The thick solid red lines in plots (a) and (b) show the spectrum of the total flexural kinetic energy PSD of the plate when the five piezoelectric patches implement respectively the series and parallel sweeping operation modes, also here with stripes with different background colour to identify the control frequency range of each vibration absorber. The two plots show remarkable reductions of most resonance peaks comprised between 30 Hz and 1 kHz. In the series mode, the system produces good flexural vibration reductions below 200 Hz comprised between 6 dB and 12 dB. The performance drops to around 4 dB reduction of the flexural vibration for the resonances comprised in the 200-300 Hz band and then very good control effects are obtained between 300 and 500 Hz, with reductions of the resonance peak amplitudes between 6 and 12 dB. The system also works well between 550 Hz and 750 Hz achieving about 6 dB reductions of the peaks in this band and some extra reductions can be seen at higher frequencies in the 750-950 Hz band. The parallel sweeping operation mode also shows very good performances at low and mid frequencies, with improved control effects at the first resonance peak.

Figure 5.14 summarizes the reductions in dB at the peaks with higher amplitudes obtained with all the studied type of vibration absorbers and operation modes. The green and cyan bars, first and second starting from the left-hand side, present respectively the total flexural kinetic energy PSD peak reduction

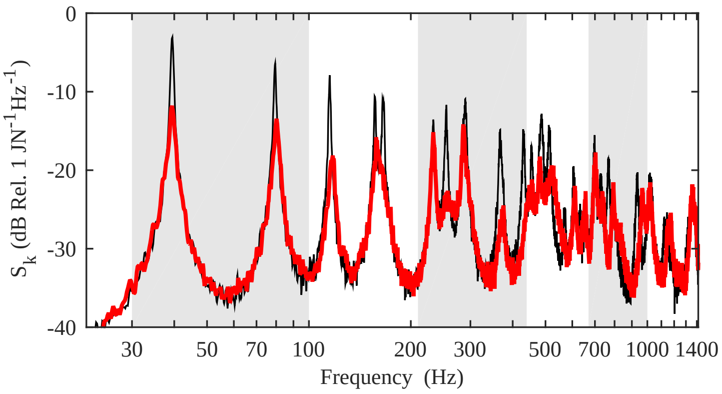

(a) Series sweeping.

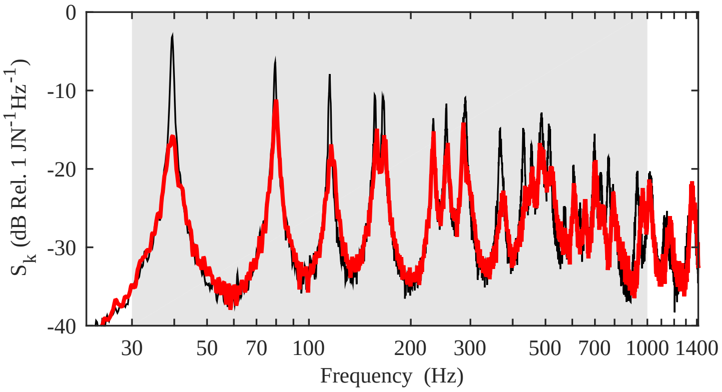

(b) Parallel sweeping.

Figure 5.13.: PSD of the total flexural kinetic energy of the plate with the five piezoelectric transducers in short circuit (thin solid black line) and connected to sweeping RL shunts (thick solid red line) operating in (a) series and (b) parallel mode tuned to the resonance frequencies as specified in table 5.4.

at many of the resonances in the 30 to 1 kHz frequency band for the fixed and optimally tuned RL shunts and for the mistuned RL shunts. The fixed shunt system achieves very good reductions of the flexural response at the five targeted resonances, with reductions ranging from a minimum of 3 dB for the resonance peak at 768 Hz to around 18 dB for the resonance at 115 Hz. On the other hand, when the shunts are mistuned by 25% of their optimal values, they have little impact at the resonance peaks located at 455 Hz and 768 Hz but they are still able to reduce the amplitude of the flexural response by about 3.5 to 7 dB at 39, 115 and 255 Hz. Nevertheless, the fact that they are mistuned for a particular frequency does not exclude that they can be tuned to a different one; which can explain the good reduction of around 11 dB obtained at 430 Hz, 6

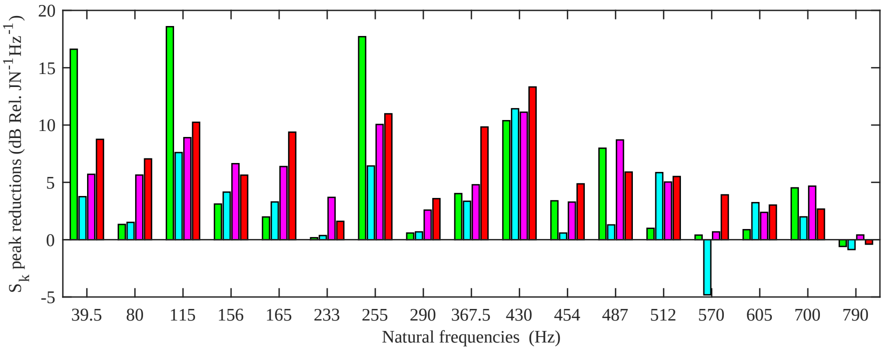

(a) Series operation mode.

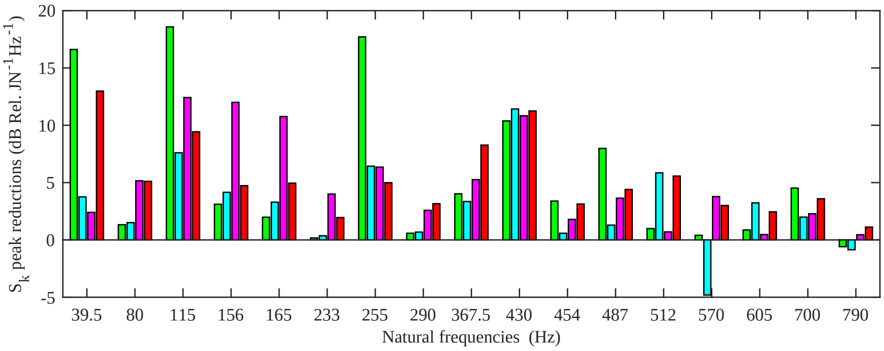

(b) Parallel operation mode.

Figure 5.14.: Flexural kinetic energy PSD peak reduction at resonance frequencies for the plate with the five piezoelectric transducers implementing a fixed tuned RL shunt (first green column from the left), a mistuned RL shunt (second cyan column from the left), a (a) series and (b) parallel switching RL shunt (third magenta column from the left) and a (a) series and (b) parallel sweeping RL shunt (fourth red column from the left).

dB obtained at 512 Hz and 7 dB obtained at 935 Hz. In contrast they enhance the flexural response of the plate by almost 5 dB at the resonance peaks around 570 Hz.

The series time-varying vibration absorbers shown in (a) achieve good reductions for almost all the resonance peaks, with a higher performance of the series sweeping operation mode. Plot (a) shows the parallel operation mode, which works very well at low frequencies below 200 Hz in particular for the switching vibration absorber although it has not a good performance on the first resonance peak where the sweeping achieves an amplitude reduction of almost 13 dB. It is expected that adjusting the time constant of the first resonance peak the performance would increase. Generally speaking the sweeping series mode is the one with the better performance, this piezoelectric shunted vibration absorber is able to consistently reduce the amplitude of the flexural response at most of the resonance peaks in the 30 to 1 kHz frequency band.

5.5 CHAPTER CONCLUDING REMARKS

The study presented in this chapter has shown the effects of using time-varying shunted piezoelectric vibration absorbers bonded on a thin lightly damped plate to control its flexural response up to 1 kHz when using five vibration absorber units. A system composed of only a single vibration absorber unit was also analysed.

Discrete and continuous variations of the shunt were proposed and analysed, in particular: switching and sweeping operation modes, with their respective control laws. It was shown that these kind of time-varying shunted piezoelectric vibration absorbers, in particular the sweeping vibration absorber, is able to reduce the flexural response of the panel both at low frequencies, where the plate total flexural kinetic energy spectrum is characterised by well separated resonance peaks, and at mid frequencies were it is characterised by wide band crests due to the overlap of clusters of natural modes.

Keeping in mind that the sweeping vibration absorbers work without a precise shunt tuning, only the damping ratio and initial and final values of a frequency range are needed, they could offer significant advantages for the development of robust, effective, modular and easy to use devices. Furthermore, they could be operated without the need of system identification of the hosting structure physical properties.

6

CONCLUSIONS AND FUTURE WORK

The research presented in this thesis is focused on the broadband vibration control of thin structures using piezoelectric transducers. Considering that this type of system could be applied in a wide variety of applications, active and semi-passive strategies were presented for the control of the flexural response of a thin aluminium panel.

Novel shaped piezoelectric actuators were proposed in chapter 3 to increase the open loop stability and therefore the global performance of the velocity feedback loop. The proposed actuator is composed of 6 triangular leafs arranged to form an hexagon. In the ideal hexagonal piezoelectric actuator the moments produced along the edges of consecutive triangular leafs are cancelled; as a result the actuation effect of the transducer can be described by moments along the edges of the hexagon and transversal point forces at its vertices balanced by a transversal point force at the centre of the hexagon which is collocated with the accelerometer sensor. Due to constructive reasons, the patch used in the prototype presents gaps between consecutive triangular leafs, which may lead to a disadvantageous situation where the internal moments are not properly cancelled and the transversal force is not at the centre of the hexagon but at the tip of each triangular leaf, resulting in a weaker collocation effect with the accelerometer sensor. Simulation and off-line experimental results were presented for SISO and MIMO configurations. The theoretical work predicted impressive results for both the SISO and MIMO configurations and the experimental ones, despite the issue described above, showed good reductions at most of the resonance peaks in the considered frequency range.

Considering the semi-passive strategy for a shunted piezoelectric vibration absorber, chapter 4 presents a fully coupled model of the panel with a pair of identical piezoelectric transducers, which form a symmetric laminate around the mid-plane of the panel. The equations of motion of plate with the shunted piezoelectric transducers are obtained using the extended form of Hamilton's principle. Then, a simplified system that neglects the structural damping and considers only the first natural mode of the structure is considered to obtain analytical expressions for the optimal values of the RL shunt that maximize its vibration absorption effect. These values are then compared to the ones obtained using a genetic algorithm for an increasing number of considered modes in the fully coupled model of the panel with the pair of piezoelectric transducers. This study showed that the values found for the simplified system are not accurate for two-dimensional distributed structures and that at least 150 natural modes of the structure must be considered for the flexural kinetic energy PSD reduction and the inductance and resistance variables to converge. This phenomena could be explained by two effect: the high modal overlap of thin structures and by the large self and cross mechanical and electromechanical modal coupling factors which characterise the coupling between the plate and the pair of transducers.

The second study presented in chapter 4 deals with the effects of the transducers dimension on the performance of a shunted piezoelectric vibration absorber. In order to control the flexural response of the plate in frequencies near its first resonance, the transducers should have a thickness equal to the one of the plate and be quite large, covering most of the panel.

In chapter 5 two control strategies are proposed for a time-varying semi-passive shunted piezoelectric absorber to produce a broadband control effect instead of the narrowband effect of the classical shunted piezoelectric absorbers usually found in the literature. The switching operation mode, in which the values of the shunt inductance and resistance are iteratively varied to control the flexural response of the structure near three different resonance frequencies. And the sweeping operation mode in which there is no proper tuning of the shunt, a sine function with the initial and final values of the targeted frequency band is used to obtain the current value for the shunt inductance while the resistance value is obtained by fixing the damping ratio of the electrical circuit. It must be noted that if the frequency band is chosen to be too large, the control effect of the absorbers will be spread and lower performance will be seen at the resonance peaks. Single and multiple patch configurations were analysed with promising results for the sweeping operation mode, reducing the flexural response of the panel both at low and mid-high frequencies. Considering that there is no need to perform a system identification of the hosting structure to determine its physical properties, as this sweeping absorbers only require the initial and final values of the targeted frequency band and the damping ratio value, they can offer significant practical advantages for the development of effective, robust and easy to use modular devices.

6.1 FUTURE WORK

The following works could be carried out concerning the active vibration system presented in chapter 3:

- reduce the gap between consecutive triangular leafs of the hexagonal MFC patch or consider different construction methods or materials such as PVDF and conduct experimental test on these new patches.
- Investigate the viscous elastic effects of the bonding layer to obtain a more accurate result of the actuation effect of the piezoelectric actuator bonded on the panel.
- It could also be interesting to model the system using a numerical method (e.g. using finite element analysis) to confirm the negative influence of these gaps on the stability of the feedback loop.

In addition, regarding the semi-passive shunted piezoelectric absorbers presented in chapters 4 and 5, the following ideas emerged as a natural continuation of the current research:

- implement the switching and sweeping shunted vibration absorbers on a prototype and compare the results to the ones obtained in the simulations presented in chapter 5.
- Study the possibility of replacing the resistor in the shunt with an energy harvesting circuit; determine how much energy could be extracted for a tonal excitation first, which matches a natural frequency of the system and then for different types of excitations.
- Consider the possibility of self-powered semi-passive shunted piezoelectric vibration absorbers. Multiple shunted transducers systems could be used in which some of the units harvest sufficient electrical energy to drive the sweeping control system of the rest of them.

LIST OF PUBLICATIONS

INTERNATIONAL PEER REVIEWED JOURNAL PUBLICATIONS

1. D. E. Casagrande, P. Gardonio and M. Zilletti, *Smart panel with time-varying shunted piezoelectric patch absorbers for broadband vibration control*, submitted to Journal of Sound and Vibration (in review), 2016.
2. P. Gardonio and D. E. Casagrande, *Shunted piezoelectric patch vibration absorber on two-dimensional thin structures: tuning considerations*, submitted to the Journal of Sound and Vibration (in review), 2016.

FULL PAPERS IN PROCEEDINGS OF INTERNATIONAL CONFERENCES

1. D. E. Casagrande and P. Gardonio, *Experimental implementation of a velocity feedback loop with a hexagonal piezoelectric patch actuator*, Proceedings of the International Conference on Noise and Vibration Engineering (ISMA), 2014, Leuven, Belgium.
2. D. E. Casagrande, P. Gardonio and M. Zilletti, *Time-varying shunted piezoelectric patch absorbers for broadband vibration control*, Proceedings of the 22nd International Congress on Sound and Vibration (ICSV), 2015, Florence, Italy.
3. D. E. Casagrande, P. Gardonio and M. Zilletti, *Sweeping piezoelectric patch vibration absorbers*, Proceedings of the International Conference on Motion and Vibration Control (13th MoViC) and of the International Conference on Recent Advances in Structural Dynamics (12th RASD), 2016, Southampton, UK.
4. P. Gardonio and D. E. Casagrande, *Parametric study of shunted piezoelectric transducers bonded on a thin plate*, Proceedings of the International Conference on Noise and Vibration Engineering (ISMA), 2016, Leuven, Belgium.
5. M. Zientek, P. Gardonio and D. E. Casagrande, *Smart metamaterials for noise and vibration control*, Proceedings of the International Conference on Noise and Vibration Engineering (ISMA), 2016, Leuven, Belgium.

ABSTRACT IN PROCEEDINGS OF INTERNATIONAL WORKSHOPS

1. D. E. Casagrande and P. Gardonio, *Hexagonal composite piezoelectric patch actuator for vibration control*, Proceedings of the International Workshop Ceramics for Energy (CEn), 2015, Faenza, Italy.
2. D. E. Casagrande and P. Gardonio, *Piezoelectric sweeping absorbers for broadband vibration control*, Proceedings of the Industrial Workshop on Energy Efficiency Management for Vehicles and Machines, 2015, Viena, Austria.

AWARDS AND RECOGNITIONS

1. Best presentation award during the International Conference on Motion and Vibration Control (13th MoViC) and of the International Conference on Recent Advances in Structural Dynamics (12th RASD), 2016, Southampton, UK.

A

MOBILITY FUNCTIONS FOR A SIMPLY SUPPORTED PLATE

The expressions for the natural frequencies and natural modes of a simply supported plate can be defined as [70]

$$\phi_n(x,y) = 2\sin\left(\frac{r_1 \pi x}{l_x}\right)\sin\left(\frac{r_2 \pi y}{l_y}\right) \tag{A.1}$$

$$\omega_n = \sqrt{\frac{Y_p h_p^2}{12\rho_p(1-\nu_p^2)}}\left[\left(\frac{r_1\pi}{l_x}\right)^2 + \left(\frac{r_2\pi}{l_y}\right)^2\right] \tag{A.2}$$

where r_1 and r_2 are the mode indexes, Y_p and ν_p are the Young's modulus and Poisson's ratio of the panel, l_x, l_y and h_p are the length, width and thickness of the panel and ρ_p is the density of the panel.

A.1 SISO SYSTEM

The mobility functions $G_{cp}(\omega)$, $G_{cF_c}(\omega)$, $G_{cF_v}(\omega)$ and $G_{cM_e}(\omega)$ presented in equations 3.19 and 3.21 for the simulation of the SISO system were derived using a modal summation approach [70], and are defined as follows:

$$G_{cp}(\omega) = j\omega \sum_{n=1}^{\infty} \frac{\phi_n(x_c,y_c)\phi_m(x_{F_p},y_{F_p})}{M_b(\omega_n^2(1+j\eta)-\omega^2)} \tag{A.3}$$

$$G_{cF_v}(\omega) = j\omega \sum_{n=1}^{\infty} \frac{\phi_n(x_c,y_c)\phi_m(x_{F_v},y_{F_v})}{M_b(\omega_n^2(1+j\eta)-\omega^2)} \tag{A.4}$$

$$G_{cM_e}(\omega) = j\omega \sum_{n=1}^{\infty} \frac{\phi_n(x_c,y_c)\phi_m(x_{M_e},y_{M_e})}{M_b(\omega_n^2(1+j\eta)-\omega^2)} \tag{A.5}$$

$$G_{cF_c}(\omega) = j\omega \sum_{n=1}^{\infty} \frac{\phi_n(x_c,y_c)\phi_m(x_{F_c},y_{F_c})}{M_b(\omega_n^2(1+j\eta)-\omega^2)} \tag{A.6}$$

where M_b is the total mass of the plate; η is the loss factor assumed to be 2%; ω_n are the natural frequencies for a pinned-pinned panel [70]; ω is the frequency that varies from 30 Hz to 50 kHz; (x_c, y_c), (x_{M_e}, y_{M_e}), (x_{F_c}, y_{F_c}), (x_{F_v}, y_{F_v}) and (x_{F_p}, y_{F_p}) are, respectively, the coordinates of the control position and of the application points of all the moments M_e and of the force F_c, the 6 forces F_v and the force F_p; and all the different $\phi_n(x, y)$ are the mode shapes at the above mentioned positions. It must be noted that the moments M_e at the edges of the patch are modelled as couples of forces (F^+, F^-), where the distance between the two forces is defined by the smallest wavelength of interest divided by 5 (around 4 mm). Then, M_e is defined as the difference between the mode shapes at the application points of F^+ and F^-. The simulation considers three pair of forces acting on each one of the six edges of the hexagonal patch, this separation is defined by the smallest wavelength of interest divided by 2 (around 1 cm).

A.2 MIMO SYSTEM

The following matrices were used to simulate the MIMO system:

$$\dot{\mathbf{w}}_c(\omega) = \begin{bmatrix} \dot{w}_{c1}(\omega) \\ \dot{w}_{c2}(\omega) \\ \dot{w}_{c3}(\omega) \\ \dot{w}_{c4}(\omega) \\ \dot{w}_{c5}(\omega) \end{bmatrix} \tag{A.7}$$

$$\mathbf{G}_{cc}(\omega) = \begin{bmatrix} G_{11}(\omega) & G_{12}(\omega) & G_{13}(\omega) & G_{14}(\omega) & G_{15}(\omega) \\ G_{21}(\omega) & G_{22}(\omega) & G_{23}(\omega) & G_{24}(\omega) & G_{25}(\omega) \\ G_{31}(\omega) & G_{32}(\omega) & G_{33}(\omega) & G_{34}(\omega) & G_{35}(\omega) \\ G_{41}(\omega) & G_{42}(\omega) & G_{43}(\omega) & G_{44}(\omega) & G_{45}(\omega) \\ G_{51}(\omega) & G_{52}(\omega) & G_{53}(\omega) & G_{54}(\omega) & G_{55}(\omega) \end{bmatrix} \tag{A.8}$$

$$\mathbf{G}_c(\omega) = \begin{bmatrix} G_c(\omega) & 0 & 0 & 0 & 0 \\ 0 & G_c(\omega) & 0 & 0 & 0 \\ 0 & 0 & G_c(\omega) & 0 & 0 \\ 0 & 0 & 0 & G_c(\omega) & 0 \\ 0 & 0 & 0 & 0 & G_c(\omega) \end{bmatrix} \tag{A.9}$$

$$\mathbf{G}_{cp}(\omega) = \begin{bmatrix} G_{c_1 p}(\omega) \\ G_{c_2 p}(\omega) \\ G_{c_3 p}(\omega) \\ G_{c_4 p}(\omega) \\ G_{c_5 p}(\omega) \end{bmatrix} \tag{A.10}$$

where $G_c(\omega)$ is the same compensator used in the SISO system, and each element of the $\mathbf{G}_{cc}(\omega)$ matrix is obtained using equation 3.21.

B

MODAL MATRICES OF A PIEZOELECTRIC PATCH

This appendix shows how the modal matrices for the mass, stiffness and transduction coefficient of a piezoelectric patch are obtained from equations (4.80), (4.81) and (4.82).

For clarity, equation (4.73) can be expressed as:

$$\boldsymbol{\varphi}_m(x,y) = 2\,\sin\left(K_{m1}x\right)\sin\left(K_{m2}y\right) \tag{B.1}$$

where

$$K_{m1} = \frac{m_1\pi}{l_x}, \quad K_{m2} = \frac{m_2\pi}{l_y} \tag{B.2}$$

B.1 MODAL MASS MATRIX

Starting from equation (4.80), the modal mass matrix for one piezoelectric transducer can be expressed as:

$$\mathbf{M}_{pe} = 2\rho_{pe}h_{pe}\int_{A_{pe}} 2\,\sin\left(K_{m1}x\right)\sin\left(K_{m2}y\right)2\,\sin\left(K_{n1}x\right)\sin\left(K_{n2}y\right)\mathrm{d}A_{pe} \tag{B.3}$$

Then, the area integral can be broken into two integrals along the x and y directions:

$$\mathbf{M}_{pe} = 8\rho_{pe}h_{pe}\int_{x_1}^{x_2}\sin\left(K_{m1}x\right)\sin\left(K_{n1}x\right)\mathrm{d}x\int_{y_1}^{y_2}\sin\left(K_{m2}y\right)\sin\left(K_{n2}y\right)\mathrm{d}y \tag{B.4}$$

where x_1, x_2 and y_1, y_2 are respectively the x and y coordinates where the transducer begins and ends. Then, the following trigonometric identity can be used:

$$\sin\left(ax\right)\sin\left(bx\right) = \frac{1}{2}\left[\cos\left((a-b)x\right) - \cos\left((a+b)x\right)\right] \tag{B.5}$$

so that equation (B.4) becomes

$$\mathbf{M}_{pe} = 2\rho_{pe}h_{pe}\int_{x_1}^{x_2}\left[\cos\left(Ax\right) - \cos\left(Bx\right)\right]\mathrm{d}x\int_{y_1}^{y_2}\left[\cos\left(Cy\right) - \cos\left(Dy\right)\right]\mathrm{d}y \quad \text{(B.6)}$$

where

$$A = K_{m1} - K_{n1} \quad \text{(B.7)}$$

$$B = K_{m1} + K_{n1} \quad \text{(B.8)}$$

$$C = K_{m2} - K_{n2} \quad \text{(B.9)}$$

$$D = K_{m2} + K_{n2} \quad \text{(B.10)}$$

Solving these integrals yields:

$$\mathbf{M}_{pe} = 2\rho_{pe}h_{pe}A_{pe} \quad \text{(B.11)}$$

with

$$A_{pe} = \left[\frac{\sin\left(Ax\right)}{A} - \frac{\sin\left(Bx\right)}{B}\right]_{x_1}^{x_2}\left[\frac{\sin\left(Cy\right)}{C} - \frac{\sin\left(Dy\right)}{D}\right]_{y_1}^{y_2} \quad \text{(B.12)}$$

Then, depending on the values of the coefficients A, B, C and D there are four expressions to calculate A_{pe} listed below.

CASE 1: $A = 0$, which means $K_{m1} = K_{n1}$

$$A_{pe} = \left[x_2 - x_1 - \frac{\sin\left(Bx_2\right) - \sin\left(Bx_1\right)}{B}\right] l_{pe_y} \quad \text{(B.13)}$$

CASE 2: $C = 0$, which means $K_{m2} = K_{n2}$

$$A_{pe} = l_{pe_x}\left[y_2 - y_1 - \frac{\sin\left(Dy_2\right) - \sin\left(Dy_1\right)}{D}\right] \quad \text{(B.14)}$$

CASE 3: $A = 0$ and $C = 0$, which means $K_{m1} = K_{n1}$ and $K_{m2} = K_{n2}$

$$A_{pe} = \left[x_2 - x_1 - \frac{\sin\left(Bx_2\right) - \sin\left(Bx_1\right)}{B}\right]\left[y_2 - y_1 - \frac{\sin\left(Dy_2\right) - \sin\left(Dy_1\right)}{D}\right] \quad \text{(B.15)}$$

CASE 4: the most general case, when $A \neq 0$ and $C \neq 0$

$$A_{pe} = l_{pe_x} l_{pe_y} \quad \text{(B.16)}$$

where

$$l_{pe_x} = \frac{\sin(Ax_2) - \sin(Ax_1)}{A} - \frac{\sin(Bx_2) - \sin(Bx_1)}{B} \tag{B.17}$$

$$l_{pe_y} = \frac{\sin(By_2) - \sin(By_1)}{B} - \frac{\sin(Dy_2) - \sin(Dy_1)}{D} \tag{B.18}$$

B.2 MODAL STIFFNESS MATRIX

Equation (4.81) can be written as

$$\mathbf{K}_{pe} = 2I_{pe} \int_{A_{pe}} \begin{bmatrix} \boldsymbol{\varphi}_{m,xx} & \boldsymbol{\varphi}_{m,yy} & 2\boldsymbol{\varphi}_{m,xy} \end{bmatrix} \begin{bmatrix} \frac{Y^{\mathbf{E}}_{pe}}{1-\nu^{\mathbf{E}2}_{pe}} & \frac{\nu^{\mathbf{E}}_{pe} Y^{\mathbf{E}}_{pe}}{1-\nu^{\mathbf{E}2}_{pe}} & 0 \\ \frac{\nu^{\mathbf{E}}_{pe} Y^{\mathbf{E}}_{pe}}{1-\nu^{\mathbf{E}2}_{pe}} & \frac{Y^{\mathbf{E}}_{pe}}{1-\nu^{\mathbf{E}2}_{pe}} & 0 \\ 0 & 0 & \frac{Y^{\mathbf{E}}_{pe}}{2(1+\nu^{\mathbf{E}}_{pe})} \end{bmatrix} \begin{bmatrix} \boldsymbol{\varphi}_{n,xx} \\ \boldsymbol{\varphi}_{n,yy} \\ 2\boldsymbol{\varphi}_{n,xy} \end{bmatrix} \mathrm{d}A_{pe} \tag{B.19}$$

$$\mathbf{K}_{pe} = 2I_{pe} \frac{Y^{\mathbf{E}}_{pe}}{1-\nu^{\mathbf{E}2}_{pe}} \int_{A_{pe}} \begin{bmatrix} \boldsymbol{\varphi}_{m,xx} & \boldsymbol{\varphi}_{m,yy} & 2\boldsymbol{\varphi}_{m,xy} \end{bmatrix} \begin{bmatrix} 1 & \nu^{\mathbf{E}}_{pe} & 0 \\ \nu^{\mathbf{E}}_{pe} & 1 & 0 \\ 0 & 0 & \frac{1-\nu^{\mathbf{E}}_{pe}}{2} \end{bmatrix} \begin{bmatrix} \boldsymbol{\varphi}_{n,xx} \\ \boldsymbol{\varphi}_{n,yy} \\ 2\boldsymbol{\varphi}_{n,xy} \end{bmatrix} \mathrm{d}A_{pe} \tag{B.20}$$

$$\begin{aligned} \mathbf{K}_{pe} = 2I_{pe} \frac{Y^{\mathbf{E}}_{pe}}{1-\nu^{\mathbf{E}2}_{pe}} \int_{A_{pe}} \Big[& \boldsymbol{\varphi}_{m,xx}\boldsymbol{\varphi}_{n,xx} + \nu^{\mathbf{E}}_{pe}(\boldsymbol{\varphi}_{m,yy}\boldsymbol{\varphi}_{n,xx} + \boldsymbol{\varphi}_{m,xx}\boldsymbol{\varphi}_{n,yy}) + \\ & \boldsymbol{\varphi}_{m,yy}\boldsymbol{\varphi}_{n,yy} + 2(1-\nu^{\mathbf{E}}_{pe})\boldsymbol{\varphi}_{m,xy}\boldsymbol{\varphi}_{n,xy} \Big] \mathrm{d}A_{pe} \end{aligned} \tag{B.21}$$

Then, the next step is to calculate the second derivatives of $\phi(x,y)$ with respect to x and y:

$$\boldsymbol{\varphi}_{m,x} = 2K_{m1}\cos(K_{m1}x)\sin(K_{m2}y) \tag{B.22}$$

$$\boldsymbol{\varphi}_{m,xx} = -2K^2_{m1}\sin(K_{m1}x)\sin(K_{m2}y) \tag{B.23}$$

$$\boldsymbol{\varphi}_{m,y} = 2K_{m2}\sin(K_{m1}x)\cos(K_{m2}y) \tag{B.24}$$

$$\boldsymbol{\varphi}_{m,yy} = -2K^2_{m2}\sin(K_{m1}x)\sin(K_{m2}y) \tag{B.25}$$

$$\boldsymbol{\varphi}_{m,xy} = 2K_{m1}K_{m2}\sin(K_{m1}x)\sin(K_{m2}y) \tag{B.26}$$

Replacing these expressions into (B.21) yields

$$\begin{aligned}\mathbf{K}_{pe} = 2I_{pe}\frac{Y^{\mathbf{E}}_{pe}}{1-\nu^{\mathbf{E}^2}_{pe}}\Bigg[&\beta_1\int_{A_{pe}} 4\sin\left(K_{m1}x\right)\sin\left(K_{m2}y\right)\sin\left(K_{n1}x\right)\sin\left(K_{n2}y\right)\mathrm{d}A_{pe}+\\ &\beta_2\int_{A_{pe}} 4\cos\left(K_{m1}x\right)\cos\left(K_{m2}y\right)\cos\left(K_{n1}x\right)\cos\left(K_{n2}y\right)\mathrm{d}A_{pe}\Bigg]\end{aligned} \tag{B.27}$$

where

$$\beta_1 = K^2_{m1}K^2_{n1} + \nu^{\mathbf{E}}_{pe}K^2_{m2}K^2_{n1} + \nu^{\mathbf{E}}_{pe}K^2_{m1}K^2_{n2} + K^2_{m2}K^2_{n2} \tag{B.28}$$

$$\beta_2 = K_{m1}K_{m2}K_{n1}K_{n2} \tag{B.29}$$

For clarity, the two surface integrals of equation (B.27) are named $A^{\beta_1}_{pe}$ and $A^{\beta_2}_{pe}$, so that equation (B.27) is re-written as

$$\mathbf{K}_{pe} = 2I_{pe}\frac{Y^{\mathbf{E}}_{pe}}{1-\nu^{\mathbf{E}^2}_{pe}}\left[\beta_1 A^{\beta_1}_{pe} + \beta_2 A^{\beta_1}_{pe}\right] \tag{B.30}$$

Then, solving $A^{\beta_1}_{pe}$, which can be broken into two integrals gives:

$$A^{\beta_1}_{pe} = \int_{x_1}^{x_2} 2\sin\left(K_{m1}x\right)\sin\left(K_{n1}x\right)\mathrm{d}x\int_{y_1}^{y_2} 2\sin\left(K_{m2}y\right)\sin\left(K_{n2}y\right)\mathrm{d}y \tag{B.31}$$

Using the trigonometric identity presented in equation (B.5) and the values A, B, C and D defined in equations (B.7)-(B.10), equation (B.31) becomes

$$A^{\beta_1}_{pe} = \int_{x_1}^{x_2}\left[\cos\left(Ax\right) - \cos\left(Bx\right)\right]\mathrm{d}x\int_{y_1}^{y_2}\left[\cos\left(Cy\right) - \cos\left(Dy\right)\right]\mathrm{d}y \tag{B.32}$$

And solving these integrals gives

$$A^{\beta_1}_{pe} = \left[\frac{\sin\left(Ax\right)}{A} - \frac{\sin\left(Bx\right)}{B}\right]_{x_1}^{x_2}\left[\frac{\sin\left(Cy\right)}{C} - \frac{\sin\left(Dy\right)}{D}\right]_{y_1}^{y_2} \tag{B.33}$$

On the other hand, the same procedure is conducted for the second integral:

$$A^{\beta_2}_{pe} = \int_{x_1}^{x_2} 2\cos\left(K_{m1}x\right)\cos\left(K_{n1}x\right)\mathrm{d}x\int_{y_1}^{y_2} 2\cos\left(K_{m2}y\right)\cos\left(K_{n2}y\right)\mathrm{d}y \tag{B.34}$$

Using the following trigonometric identity

$$\cos\left(ax\right)\cos\left(bx\right) = \frac{1}{2}\left[\cos\left((a-b)x\right) + \cos\left((a+b)x\right)\right] \tag{B.35}$$

equation (B.34) becomes

$$A_{pe}^{\beta_2} = \int_{x_1}^{x_2} \left[\cos\left(Ax\right) + \cos\left(Bx\right)\right] \mathrm{d}x \int_{y_1}^{y_2} \left[\cos\left(Cy\right) + \cos\left(Dy\right)\right] \mathrm{d}y \tag{B.36}$$

And solving these integrals yields

$$A_{pe}^{\beta_2} = \left[\frac{\sin\left(Ax\right)}{A} + \frac{\sin\left(Bx\right)}{B}\right]_{x_1}^{x_2} \left[\frac{\sin\left(Cy\right)}{C} + \frac{\sin\left(Dy\right)}{D}\right]_{y_1}^{y_2} \tag{B.37}$$

As for the modal mass matrix, depending on the values of the coefficients A, B, C and D there are for cases, which are listed below.

CASE 1: $A = 0$, which means $K_{m1} = K_{n1}$

$$A_{pe}^{\beta_1} = \left[x_2 - x_1 - \frac{\sin\left(Bx_2\right) - \sin\left(Bx_1\right)}{B}\right] l_{pe_y}^{\beta_1} \tag{B.38}$$

$$A_{pe}^{\beta_2} = \left[x_2 - x_1 + \frac{\sin\left(Bx_2\right) - \sin\left(Bx_1\right)}{B}\right] l_{pe_y}^{\beta_2} \tag{B.39}$$

$$\tag{B.40}$$

CASE 2: $C = 0$, which means $K_{m2} = K_{n2}$

$$A_{pe}^{\beta_1} = l_{pe_x}^{\beta_1} \left[y_2 - y_1 - \frac{\sin\left(Dy_2\right) - \sin\left(Dy_1\right)}{D}\right] \tag{B.41}$$

$$A_{pe}^{\beta_2} = l_{pe_x}^{\beta_2} \left[y_2 - y_1 + \frac{\sin\left(Dy_2\right) - \sin\left(Dy_1\right)}{D}\right] \tag{B.42}$$

CASE 3: $A = 0$ and $C = 0$, which means $K_{m1} = K_{n1}$ and $K_{m2} = K_{n2}$

$$A_{pe}^{\beta_1} = \left[x_2 - x_1 - \frac{\sin\left(Bx_2\right) - \sin\left(Bx_1\right)}{B}\right] \left[y_2 - y_1 - \frac{\sin\left(Dy_2\right) - \sin\left(Dy_1\right)}{D}\right] \tag{B.43}$$

$$A_{pe}^{\beta_2} = \left[x_2 - x_1 + \frac{\sin\left(Bx_2\right) - \sin\left(Bx_1\right)}{B}\right] \left[y_2 - y_1 + \frac{\sin\left(Dy_2\right) - \sin\left(Dy_1\right)}{D}\right] \tag{B.44}$$

CASE 4: the most general case, when $A \neq 0$ and $C \neq 0$

$$A_{pe}^{\beta_1} = l_{pe_x}^{\beta_1} l_{pe_y}^{\beta_1} \tag{B.45}$$

$$A_{pe}^{\beta_2} = l_{pe_x}^{\beta_2} l_{pe_y}^{\beta_2} \tag{B.46}$$

where

$$l_{pe_x}^{\beta_1} = \frac{\sin(Ax_2) - \sin(Ax_1)}{A} - \frac{\sin(Bx_2) - \sin(Bx_1)}{B} \tag{B.47}$$

$$l_{pe_y}^{\beta_1} = \frac{\sin(By_2) - \sin(By_1)}{B} - \frac{\sin(Dy_2) - \sin(Dy_1)}{D} \tag{B.48}$$

$$l_{pe_x}^{\beta_2} = \frac{\sin(Ax_2) - \sin(Ax_1)}{A} + \frac{\sin(Bx_2) - \sin(Bx_1)}{B} \tag{B.49}$$

$$l_{pe_y}^{\beta_2} = \frac{\sin(By_2) - \sin(By_1)}{B} + \frac{\sin(Dy_2) - \sin(Dy_1)}{D} \tag{B.50}$$

B.3 MODAL TRANSDUCTION COEFFICIENT MATRIX

Recalling equations (4.27) and (4.85), the modal electromechanical transduction coefficient presented in equation (4.82) can be expressed as:

$$\boldsymbol{\Theta}_{pe} = 2z_{pe} \int_{A_{pe}} \left[\phi_{m,xx} e_{31} + \phi_{m,yy} e_{32}\right] \mathrm{d}A_{pe} \tag{B.51}$$

$$\boldsymbol{\Theta}_{pe} = 2z_{pe} \int_{A_{pe}} \left[-2K_{m1}^2 e_{31} + -2K_{m2}^2 e_{32}\right] \sin(K_{m1}x) \sin(K_{m2}y) \mathrm{d}A_{pe} \tag{B.52}$$

$$\boldsymbol{\Theta}_{pe} = -4z_{pe} \left[K_{m1}^2 e_{31} + K_{m2}^2 e_{32}\right] \int_{x_1}^{x_2} \sin(K_{m1}x) \mathrm{d}x \int_{y_1}^{y_2} \sin(K_{m2}y) \mathrm{d}y \tag{B.53}$$

$$\boldsymbol{\Theta}_{pe} = 4z_{pe} \left[K_{m1}^2 e_{31} + K_{m2}^2 e_{32}\right] \left[\frac{\cos(K_{m1}x)}{K_{m1}}\right]_{x_1}^{x_2} \left[\frac{\cos(K_{m2}y)}{K_{m2}}\right]_{y_1}^{y_2} \tag{B.54}$$

$$\boldsymbol{\Theta}_{pe} = 4z_{pe} \frac{K_{m1}^2 e_{31} + K_{m2}^2 e_{32}}{K_{m1} K_{m2}} l_{pe_x} l_{pe_y} \tag{B.55}$$

where

$$l_{pe_x} = [\cos(K_{m1}x_2) - \cos(K_{m1}x_1)] \tag{B.56}$$

$$l_{pe_y} = [\cos(K_{m2}y_2) - \cos(K_{m2}y_1)] \tag{B.57}$$

C

OPTIMUM SHUNT CALCULATION USING GENETIC ALGORITHMS

Genetic algorithms are used for solving constrained and unconstrained optimization problems inspired by the concepts of natural selection and natural genetics found in biological evolution [113].

Starting from an initial number or population of solutions the GA iteratively modifies individuals of these populations. At each step it randomly selects and uses individuals from the current population as parents to produce the children for the next generation. By selecting the proper parameters and iterations the algorithm converges to an optimal solution.

The basic items used in a typical genetic algorithm are:

1. an initial population of guesses of the solution to the problem;
2. a method to calculate the accuracy or suitability of the individual solutions of the population;
3. a method to combine fragments of the better solutions to create new ones;
4. and the last item is a mutation operator, in this way there is no loss of diversity within the population.

There are two main differences between GA and classical optimisation algorithms [114]:

1. a GA generates a population of individuals at each iteration where the best ones converge to an optimal solution; while a classical algorithm generates a single point at each iteration where the sequence of points converge to an optimal solution.
2. in a GA the next population is chosen using a random number generator while in a classical algorithm the next point is calculated by a deterministic computation.

C.1 GA IMPLEMENTATION

The GA used in this work is the one provided by MATLAB optimisation toolbox. This algorithm in particular works in the following way [114]:

1. an initial population is randomly created or given as input.
2. The genetic algorithm iteratively creates sets of new populations, to do this the following steps are performed:
    a) a fitness value is calculated for each individual in the population,
    b) the parents are chosen based on this fitness values,
    c) the individuals with the best fitness value are called *elite*, these are passed directly to the next population,
    d) children are created from the parents using two methods: by making random changes to a single parent (i.e mutation) or by combining some properties of a pair of parents (i.e. crossover),
    e) the current population is replaced with the new one formed by the children and elite members.
3. When one of the stopping criteria is accomplished the GA stops.

You can apply the genetic algorithm to solve problems that are not well suited for standard optimization algorithms, including problems in which the objective function is discontinuous, nondifferentiable, stochastic, or highly nonlinear.

MATLABs GA function has a variety of parameters that can be set to meet different needs, for the full list see reference [115]. In this work the following parameters were used:

fitnessfcn: this is the function that calculates the fitness value for each individual in the population, in this case the function calculated the time averaged flexural kinetic energy defined in equation (4.119);

nvars: specifies the number of variables used in the fitness function, set to 2 as both the optimal inductance and optimal resistance of the shunt are to be found;

lb: defines a set of lower bounds for the considered variables, set to 1 H and 100 kΩ;

ub: defines a set of upper bounds for the considered variables, set to 2000 H and 5 MΩ.

options: this parameters can be used to define a wide range of parameters, such as the initial population, the number of individuals in the population, the number of iterations, set particular parameters for the crossovers and mutations, enabling the use of parallel computing and more.

BIBLIOGRAPHY

[1] PI Ceramic, “Piezoelectric ceramic products: fundamentals, characteristics and applications.” https://www.piceramic.com/en/piezo-technology/fundamentals/#c10760, 2016.

[2] A. Preumont, *Mechatronics*. Dordrecht: Springer, 2006.

[3] M. Griffin, *Handbook of human vibration*. London: Academic press, 1990.

[4] N. Mansfield, *Human response to vibration*. Boca Raton, Florida: CRC Press, 2005.

[5] D. Mead, *Passive vibration control*. Chichester: John Wiley & sons, 2000.

[6] C. Fuller, S. Elliot, and P. Nelson, *Active Control of Vibration*. London: Academic Press, 1997.

[7] S. Elliot, *Signal processing for active control*. London: Academic Press, 2000.

[8] A. Preumont, *Vibration control of active structures (3rd ed.)*. Berlin: Springer-Verlag, 2011.

[9] R. Clark, W. Saunders, and G. Gibbs, *Adaptive Structures (1st ed.)*. New York: John Wiley and Sons Inc., 1998.

[10] O. Baumann and S. Elliot, The stability of decentralized multichannel velocity feedback controllers using inertial actuators, *Journal of the Acoustical Society of America*, vol. 121, pp. 188–196, 2007.

[11] Y. Aoki, P. Gardonio, and S. Elliottt, Modelling of a piezoceramic patch actuator for velocity feedback control, *Journal of Smart Materials and Structures*, vol. 17, pp. 015052:1–015052:13, 2008.

[12] P. Gardonio, S. Miani, F. Blanchini, D. Casagrande, and E. S. J., Plates with decentralised velocity feedback loops. power absorption and kinetic energy considerations, *Journal of sound and vibration*, vol. 331, no. 8, pp. 1722–1741, 2012.

[13] P. Gardonio, Y. Aoki, and S. Elliott, Smart panel with active damping wedges along the perimeter, *Journal of Smart Materials and Structures*, vol. 19, pp. 1–15, 2010.

[14] Y. Aoki, P. Gardonio, M. Gavagni, C. Galassi, and S. Elliottt, Parametric study of a piezoceramic patch actuator for proportional velocity feedback control loop, *Journal of Vibration and Acoustics*, vol. 132, no. 6, pp. 061007:1–061007:10, 2010.

[15] P. Gardonio, Composite smart panels for active control of sound radiation, in *Wiley encyclopedia of composites* (L. Nicolais and A. Borzacchiello, eds.), John Wiley & Sons, 2011.

[16] J. Dosch, D. Inman, and E. Garcia, A self-sensing piezoelectric actuator for collocated control, *Journal of Intelligent Materials Systems and Structures*, vol. 3, no. 1, p. 166–185, 1992.

[17] E. Anderson, N. Hagood, and J. Goodliffe, Self-sensing piezoelectric actuation: analysis and application to controlled structures, in *Proceedings of the AIAA/ASME/ASCE/AHS/ASC Structures, Structural Dynamics, Materials Conference*, (Dallas, USA), pp. 2141–2155, 1992.

[18] S. Moheimani, A survey of recent innovations in vibration damping and control using shunted piezoelectric transducers, *IEEE Transactions on Control Systems Technology*, vol. 11, no. 1, pp. 482–494, 2003.

[19] R. Forward, Electronic damping of vibrations in optical structures, *Applied optics*, vol. 18, no. 5, pp. 690–697, 1979.

[20] K. Uchino and T. Ishii, Mechanical damper using piezoelectric ceramics, *Journal of the Ceramic Society of Japan*, vol. 96, no. 8, pp. 863–867, 1988.

[21] N. Hagood and A. von Flotow, Damping of structural vibrations with piezoelectric materials and passive electrical networks, *Journal of Sound and Vibration*, vol. 146, no. 2, pp. 243–268, 1991.

[22] J. Den Hartog, *Mechanical Vibrations*. New York: McGraw-Hill, 1956.

[23] M. Ahmadian and P. De Guilio, Recent advances in the use of piezoceramics for vibration suppression, *The shock and Vibration Digest*, vol. 33, no. 1, 2001.

[24] S. Moheimani, A. Fleming, and S. Behrens, On the feedback structure of wideband piezoelectric shunt damping systems, *Smart Materials and Structures*, vol. 12, no. 3, pp. 49–56, 2003.

[25] R. Forward, "Electromechanical transducer-coupled mechanical structure with negative capacitance compensation circuit." United States patent, 1979. Number 4.158.787.

[26] M. Tsai and K. Wang, On the structural damping characteristics of active piezoelectric actuators with passive shunt, *Journal of Sound and Vibration*, vol. 221, pp. 1–22, 1999.

[27] J. Tang and K. Wang, Active-passive hybrid piezoelectric networks for vibration control: comparison and improvement, *Smart Materials and Structures*, vol. 10, no. 4, pp. 794–806, 2001.

[28] S. Wu, Broadband piezoelectric shunts for passive structural vibration control, in *Proceedings of SPIE – Smart Structures and Materials 2001: Damping and isolation, Newport Beach CA, USA*, pp. 251–261, 2001.

[29] M. Tsai and K. Wang, A coupled robust control/optimization approach for active-passive hybrid piezoelectric networks, *Smart Materials and Structures*, vol. 11, no. 3, pp. 389–395, 2002.

[30] R. A. Morgan and K. W. Wang, An active-passive piezoelectric absorber for structural vibration control under harmonic excitations with time-varying frequency, part 2: algorithm development and analysis, *Journal of Vibration and Acoustic*, vol. 124, pp. 77–83, 2002.

[31] C. Park and A. Baz, Vibration control of beams with negative capacitive shunting of interdigitated electrode piezoceramics, *Journal of Vibration and Control*, vol. 11, pp. 331–346, 2005.

[32] S. Moheimani, A. Fleming, and S. Behrens, Highly resonant controller for multimode piezoelectric shunt damping, *Electronics letters*, vol. 37, pp. 1505–1506, 2001.

[33] S. Moheimani and S. Behrens, Multimode piezoelectric shunt damping with a highly resonant impedance, *IEEE Transactions on Control Systems Technology*, vol. 12, pp. 484–491, 2004.

[34] S. Behrens, A. Fleming, and S. Moheimani, A broadband controller for shunt piezoelectric damping of structural vibration, *Smart materials and Structures*, vol. 12, pp. 18–28, 2003.

[35] A. Fleming and S. Moheimani, Control orientated synthesis of high-performance piezoelectric shunt impedances for structural vibration control, *IEEE Transactions on Control Systems Technology*, vol. 13, pp. 98–112, 2005.

[36] E. Fukada, M. Date, K. Kimura, T. Okubo, H. Kodama, P. Mokry, and Y. Yamamoto, Sound isolation by piezoelectric polymer films connected to negative capacitance circuits ieee transactions on dielectrics and electrical insulation, *Smart Materials and Structures*, vol. 11, pp. 328–333, 2004.

[37] K. Wang, J. Lai, and K. Yu, An energy based parametric control approach for structural vibration suppression via semi-active piezoelectric networks, *Journal of vibration and acoustics*, vol. 118, pp. 505–509, 1996.

[38] D. Guyomar, C. Richard, and S. Mohammadi, Semi-passive vibration control based on statistics, *Journal of Sound and Vibration*, vol. 307, p. 818–833, 2007.

[39] M. Lallart, S. Harari, L. Petit, D. Guyomar, T. Richard, C. Richard, and L. Gaudiller, Blind switching damping (bsd): a self-adaptive semi-active damping technique, *Journal of Sound and Vibration*, vol. 328, p. 29–41, 2009.

[40] H. Ji, J. Qiu, P. Xia, and D. Guyomar, The influence of switching phase and frequency of voltage on the vibration damping effect in a piezoelectric actuator, *Journal of Smart Materials and Structures*, vol. 20, p. 015008:1–16, 2011.

[41] F. Casadei, M. Ruzzene, L. Dozio, and K. Cunefare, Broadband vibration control through periodic arrays of resonant shunts: experimental investigation on plates, *Smart Materials and Structures*, vol. 19, p. 015002(13pp), 2009.

[42] M. Zientek, P. Gardonio, and D. Casagrande, Smart metamaterials for noise and vibration control, in *Proceedings of the International Conference on Noise and Vibration Engineering (ISMA), Katholieke Universiteit Leuven, Belgium*, 2016.

[43] B. Lossouarn, J. Deü, and M. Aucejo, Multimodal vibration damping of a beam with a periodic array of piezoelectric patches connected to a passive electrical network, *Smart Materials and Structures*, vol. 24, p. 115037(14pp), 2015.

[44] S. Moheimani and A. Fleming, *Piezoelectric transducers for vibration control and damping*. London: Springer-Verlag, 2006.

[45] B. Jaffe, W. R. Cook, and H. Jaffe, *Piezoelectric Ceramics*. London: Academic Press, 1971.

[46] J. Reddy, *Theory and Analysis of Elastic Plates and Shells*. Boca Raton: CRC Press, 2006.

[47] J. Reddy, *Energy and Variational Methods in Applied Mechanics*. New York: Wiley and Sons, 1984.

[48] C. González Diaz, C. Paulitsch, and P. Gardonio, Smart panel with active damping units.implementation of decentralized control, *Journal of the Acoustic Society of America*, vol. 124, no. 2, pp. 898–910, 2008.

[49] J. Rohlfing, P. Gardonio, and D. Thompson, Comparison of decentralized velocity feedback control for thin homogeneous and stiff sandwich panels using electrodynamic proof-mass actuators, *Journal of sound and vibration*, vol. 330, pp. 843–867, 2011.

[50] E. Bianchi, P. Gardonio, and S. Elliot, Smart panel with multiple decentralized units for the control of sound transmission. part iii: Control system implementation, *Journal of Sound and Vibration*, vol. 274, pp. 215–232, 2004.

[51] B. Petitjean, I. Legrain, F. Simon, and S. Pauzin, Active control experiments for acoustic radiation reduction of a sandwich panel: feedback and feeforward investigations, *Journal of Sound and Vibration*, vol. 252, no. 1, pp. 19–36, 2002.

[52] S. Elliott, P. Gardonio, T. Sors, and M. Brennan, Active vibro-acoustic control with multiple feedback loops, *Journal of the Acoustical Society of America*, vol. 111, no. 2, pp. 908–915, 2001.

[53] V. Jayachadran and J. Sun, Unconditional stability domains of structural control systems using dual actuator-sensor pairs, *Journal of Sound and Vibration*, vol. 208, no. 1, pp. 159–166, 1997.

[54] S. Joshi, *Control of Large Flexible Space Structures*. Berlin: Springer Verlag, 1989.

[55] M. Balas, Direct velocity feedback of large space structures, *Journal of Guidance and control*, vol. 2, pp. 252–253, 1979.

[56] M. Zilletti, S. Elliott, and E. Rustighi, Self-tuning control systems of decentralised velocity feedback, *Journal of sound and vibration*, vol. 329, pp. 2738–2750, 2010.

[57] H. Banks, R. Smith, and Y. Wang, *Smart Material Structures, Modeling, Estimation and Control*. Chichester: Wiley and Sons, 1996.

[58] P. Gardonio, E. Bianchi, and S. Elliott, Smart panel with multiple decentralised units for the control of sound transmission. part ii: design of the decentralised control units, *Journal of Sound and Vibration*, vol. 274, pp. 193–213, 2004.

[59] J. Sun, Some observations on physical duality and collocation of structural control sensors and actuators, *Journal of Sound and Vibration*, vol. 194, no. 5, pp. 765–770, 1996.

[60] M. Brennan, S. Elliott, and R. Pinnington, The dynamic coupling between piezoceramic actuators and a beam, *Journal of the Acoustical Society of America*, vol. 102, pp. 1931–1942, 1997.

[61] G. Gatti, M. Brennan, and P. Gardonio, Active damping of a beam using a physically collocated accelerometer and piezoelectric patch actuator, *Journal of Sound and Vibration*, vol. 303, pp. 798–813, 2007.

[62] P. Gardonio and S. Elliott, Smart panels for active structural acoustic control, *Smart Materials and Structures*, vol. 13, pp. 1314–1336, 2004.

[63] P. Gardonio and M. Zilletti, Semi-active multimodal vibration absorber, in *International Conference on Noise and Vibration Engineering (ISMA 2012), Katholieke Universiteit Leuven, Belgium, 2012 September 17-19*, pp. 475–488, 2012.

[64] P. Gardonio and M. Zilletti, Integrated tuneable vibration absorbers: a theoretical study, *Journal of the Acoustical Society of America*, vol. 134, no. 5, pp. 3631–3644, 2013.

[65] P. Gardonio and J. Elliot, Smart panels with velocity feedback control systems using triangularly shaped strain actuators, *Journal of the Acoustic Society of America*, vol. 117, pp. 2046–2064, 2005.

[66] P. Gardonio, Velocity feedback loops with composite hexagonal and circular piezoelectric patch actuators, in *Recent Advances in Structural Dynamics (RASD), Pisa (Italy), July 1-3*, p. 120, 2013.

[67] A. Schonecker, T. Rödig, U. Keitel, T. Daue, W. Esler, and P. Wierach, Low profile piezocomposite transducers for smart structure applications, in *Proceedings of ACTUATOR 2004, The International Conference on New Actuators, Bremen, Germany, 2004 June 14-16*, 2004.

[68] A. Bent, N. Hagood, and J. Rogers, Anisotropic actuation with piezoelectric fiber composites, *Journal of Intelligent Material Systems and Structures*, vol. 6, 1995.

[69] W. Wilkie, D. Inman, J. High, and R. Williams, Recent developments in nasa piezocomposite actuator technology, Tech. Rep. 20040082248, NASA, Hampton, VA, United States, April 2004.

[70] F. J. Fahy and P. Gardonio, *Sound and Structural Vibration*. Oxford: Academic Press, 2007.

[71] C. Lee, Theory of laminated piezoelectric plates of the design of distributed sensors/actuators. part i: Governing equations and reciprocal relationships, *Journal of the Acoustical Society of America*, vol. 87, pp. 1144–1158, 1990.

[72] A. Deraemaeker, G. Tondreau, and F. Bourgeois, Equivalent loads for two-dimensional distributed anisotropic piezoelectric transducers with

arbitrary shapes attached to thin plate structure, *Journal of the Acoustical Society of America*, vol. 129, pp. 681–690, 2011.

[73] E. Bianchi, P. Gardonio, and S. Elliot, Smart panel with multiple decentralized units for the control of sound transmission. part ii: design of the decentralized control units, *Journal of Sound and Vibration*, vol. 274, pp. 193–213, 2004.

[74] K. Yamada, H. Matsuhisa, H. Utsuno, and K. Sawada, Optimum tuning of series and parallel lr circuits for passive vibration suppression using piezoelectric elements, *Journal of Sound and Vibration*, vol. 329, pp. 5036–5057, 2010.

[75] J. Hogsberg and S. Krenk, Balanced calibration of resonant shunt circuits for piezoelectric vibration control, *Journal of Intelligent Materials Systems and Structures*, vol. 23, pp. 1937–1948, 2012.

[76] P. Soltani, G. Kerschen, G. Tondreau, and Deraemaeker, Piezoelectric vibration damping using resonant shunt circuits:an exact solution, *Smart Materials and Structures*, vol. 23, 2014.

[77] L. Cremer, M. Heckl, and E. Ungar, *Sound and Structural Vibration*. Berlin: Academic Press, 1988.

[78] R. Langley and F. Fahy, High-frequency structural vibration, in *Fundamentals of Noise and Vibration* (F. Fahy and J. Walker, eds.), pp. 490–529, London: E. & F.N. Spon, 1998.

[79] S. Wu, Piezoelectric shunts with parallel rl circuits for structural damping and vibration control, in *Proceedings of the SPIE*, vol. 2720, pp. 259–269, 1996.

[80] J. Kim, Smart panel technology for broadband noise reduction, *Noise and Vibration Worldwide*, vol. 34, pp. 13–22, 2003.

[81] J. Reddy, *Mechanics of Laminated Composite Plates and Shells: Theory and Analysis*. Boca Raton: CRC Press, 2004.

[82] C. Liang and C. Rogers, Behavior of shape memory alloy actuators embedded in composites, in *Proceedings of the 1989 International Composite Conference*, (Beijing, China), 1989.

[83] E. Crawley and J. de Luis, Use of piezoelectric actuators as elements of intelligent structures, *AIAA Journal*, vol. 25, pp. 1373–1385, 1987.

[84] E. Crawley and E. Anderson, Detailed models of piezoceramic actuation of beams, *Journal of Intelligent Materials Systems and Structures*, vol. 1, pp. 4–24, 1990.

[85] E. Dimitriadis, C. Fuller, and C. Rogers, Piezoelectric actuators for distributed vibration excitation of thin plates, *Journal of Vibration and Acoustics*, vol. 113, pp. 100–107, 1991.

[86] E. Crawley and K. Lazarus, Induced strain actuation of isotropic and anisotropic plates, *AIAA Journal*, vol. 29, pp. 944–951, 1991.

[87] S. Kim and J. Jones, Optimal design of piezoactuators for active noise and vibration control, *AIAA Journal*, vol. 29, pp. 2047–2053, 1991.

[88] S. Burke and J. Hubbard Jr., Distributed piezoelectric polymer active vibration control of a cantilever beam, *Journal of Guidance and Control*, vol. 8, pp. 605–611, 1985.

[89] B. Wang and C. Rogers, Laminate plate theory for spatially distributed induced strain actuators, *Journal of Composite Materials*, vol. 25, pp. 433–452, 1989.

[90] S. Burke and J. Hubbard Jr., Distributed transducers for structural measurement and control, *Control and Dynamic Systems*, vol. 36, pp. 223–273, 1990.

[91] C. Lee and F. Moon, Laminated piezopolymer plates for torsion and bending sensors and actuators, *Journal of the Acoustical Society of America*, vol. 85, pp. 2432–2439, 1989.

[92] N. Hagood, W. Chung, and A. von Flotow, Modelling of piezoelectric actuator dynamics for active structural control, *Journal of Intelligent Material Systems and Structures*, vol. 1, pp. 327–354, 1990.

[93] S. Crandall, D. Karnopp, A. Kurtz, and D. Pridmore-Brown, *Dynamics of Mechanical and Electromechanical Systems*. Malabar, Florida: R. E. Krieger Pub. Co., 1982.

[94] L. Meirovitch, *Principles and Techniques of Vibration*. Upper Saddle River, NJ: Prentice Hall, 1997.

[95] J. S. Bendat and A. G. Piersol, *Random Data Analysis and Measurement Procedures*. Chichester: John Wiley & Sons, 1990.

[96] K. Shin and J. Hammond, *Fundamentals of signal processing for sound and vibration*. Chichester: John Wiley & Sons, 2008.

[97] J. Ormondroyd and J. Den Hartog, The theory of the dynamic vibration absorber, *Journal of Applied Mechanics*, vol. 50, no. 7, pp. 9–22, 1928.

[98] M. Zilletti, S. Elliott, and E. Rustighi, Optimisation of dynamic vibration absorbers to minimise kinetic energy and maximise internal power dissipation, *Journal of sound and vibration*, vol. 331, pp. 4093–4100, 2012.

[99] D. Newland, *An introduction to Random Vibrations, Spectral and Wavelet Analysis (3rd ed.).* Singapore: Longman, 1993.

[100] C. Park, Dynamics modelling of beams with shunted piezoelectric elements, *Journal of Sound and Vibration*, vol. 268, pp. 115–129, 2003.

[101] M. Kozlowski, D. Cole, and R. Clark, A comprehensive study of the rl series resonant shunted piezoelectric: a feedback controls perspective, *Journal of Vibration and Acoustics*, vol. 133, p. 011012, 2011.

[102] M. Zilletti and P. Gardonio, Experimental implementation of switching and sweeping tuneable vibration absorbers for broadband vibration control, *Journal of Sound and Vibration*, vol. 334, pp. 164–177, 2015.

[103] E. Turco, P. Gardonio, and L. D. Bo, Time-varying shunt electro-magnetic tuneable vibration absorber, in *Proceedings of RASD, Southampton, UK*, 2016.

[104] J. Hollkamp, Multimodal passive vibration suppression with piezoelectric materials and resonant shunts, *Journal of Intelligent Material Systems and Structures*, vol. 5, no. 1, pp. 49–56, 1994.

[105] S. Wu, Method for multiple mode piezoelectric shunting with single pzt transducer for vibration control, *Journal of Intelligent Material Systems and Structures*, vol. 9, pp. 991–998, 1998.

[106] D. Saravanos, Damped vibration of composite plates with passive piezoelectric-resistor elements, *Journal of Sound and Vibration*, vol. 221, pp. 867–885, 1999.

[107] J. Kim, Y.-H. Ryu, and S.-B. Choi, New shunting parameter tuning method for piezoelectric damping based on measured electrical impedance, *Smart Materials and Structures*, vol. 9, pp. 868–877, 2000.

[108] A. Fleming and S. Behrens, S. Moheimani, Optimization and implementation of multimode piezoelectric shunt damping systems, *IEEE/ASME Transactions on Mechatronics*, vol. 7, pp. 87–94, 2002.

[109] J. Kim and J.-K. Lee, Broadband transmission noise reduction of smart panels featuring piezoelectric shunt circuits and sound-absorbing material, *Journal of the Acoustical Society of America*, vol. 112, pp. 990–998, 2002.

[110] N. J. Kasdin, A runga-kutta algorithm for the numerical integration of stochastic differential equations, *Journal of Guidance, Control, and Dynamics*, vol. 18, no. 1, pp. 114–120, 1995.

[111] W. Gardner, *Statistical spectral analysis: a non-probabilistic theory.* Upper Saddle River: Prentice-Hall, 1986.

[112] P. Gardonio and M. Zilletti, Sweeping tunable vibration absorbers for low and mid frequencies broad band vibration control, *Journal of the Sound and Vibration*, vol. 354, pp. 1–12, 2015.

[113] D. Coley, *An introduction to genetic algorithms for scientists and engineers*. World Scientific Publishing Co. Pte. Ltd., 1999.

[114] MathWorks, "Genetic algorithm." http://it.mathworks.com/discovery/genetic-algorithm.html, 2016.

[115] MathWorks, "MATLABs ga function." http://it.mathworks.com/help/gads/ga.html, 2016.